Simulation of Microgrid System and Low-cost Wireless Communication Network

by

Mohammed Faizan Khan

A Thesis Submitted in Partial Fulfillment
of the Requirements for the Degree of

Master of Applied Science

in

The Faculty of Engineering and Applied Science

Electrical and Computer Engineering

University of Ontario Institute of Technology

Oshawa, Ontario, Canada

August, 2019

THESIS EXAMINATION INFORMATION

Submitted by: **Mohammed Faizan Khan**

Master of Applied Science (MASc) in **Electrical Engineering**

Thesis title: Simulation of Microgrid System and Low-cost Wireless Communication Network

An oral defense of this thesis took place on June 25, 2019 in front of the following examining committee:

Examining Committee:

Chair of Examining Committee	Dr. Walid Morsi Ibrahim
Research Supervisor	Dr. Vijay Sood
Examining Committee Member	Dr. Sheldon Williamson
External Examiner	Dr. Min Dong

The above committee determined that the thesis is acceptable in form and content and that a satisfactory knowledge of the field covered by the thesis was demonstrated by the candidate during an oral examination. A signed copy of the Certificate of Approval is available from the School of Graduate and Postdoctoral Studies.

Abstract

The MATLAB/SIMULINK model of a microgrid system is presented in this thesis. The microgrid consists of a converter-fed distributed generator photovoltaic array with maximum power point tracking, a converter-fed battery storage system and a critical load which must be fed power under all circumstances. The microgrid is capable of functioning in either grid-connected or isolated modes of operation. A passive islanding detection method is utilized to switch over from P-Q to V/F control mode, when islanding is detected. The behavior of the microgrid under various faults and other conditions is analyzed. In the second part of the thesis, the need for a wireless communication between the secondary and primary controllers of the microgrid are discussed. Proof of concept results to establish a two-way communication channel for the exchange of information between the controllers are presented.

AUTHOR'S DECLARATION

I hereby declare that I am the sole author of this thesis. This is a true copy of the thesis, including any required final revisions, as accepted by my examiners.

I understand that my thesis may be made electronically available to the public.

Mohammed Faizan Khan

Statement of Controbutions

- Microgrid system described in chapter 2, and its results from chapter 4, section 4.4 are published as:
    - F. Khan, M. Y. Ali, V. K. Sood, F. Bhuiyan, P. Insull and F. Ahmad, "Simulation of microgrid system with distributed generation," *2017 IEEE Electrical Power and Energy Conference (EPEC)*, Saskatoon, SK, 2017, pp. 1-6.

I simulated a microgrid system and switched mode of operation from grid connected to islanded using IEEE 5417 islanding detection logic. Inilitalized V-F mode of operation, when switched from P-Q mode of operation

- Wireless communication system from chapter 5, section 5.2 are published as:
    - M. Y. Ali, F. Khan and V. K. Sood, "Energy Management System of a Microgrid using Particle Swarm Optimization and Wireless Communication System," *2018 IEEE Electrical Power and Energy Conference (EPEC)*, Toronto, ON, 2018, pp. 1-7.

I established a wireless communication link between a master and local controller to transmit both digital and analog signals.

Dedication

This thesis is dedicated to my parents (Bahadur Khan and Rahmat Khatoon), without their continuous love and support, this work would have not been possible to complete.

Acknowledgements

I would like to thank and express my deep appreciation to my supervisior Dr. Vijay Sood, as the accomplishment of this work would not be possible without his consistent guidance.

Table of Contents

List of Figures

List of Tables

List of Acronyms

DG	Distributed Generation
AC	Alternating Current
DC	Direct Current
UOV	Under Over Voltage
UOF	Under Over Frequency
P	Active Power
Q	Reactive Power
V/F	Voltage/Frequency
MPPT	Maximum Power Point Tracking
PV	Photovoltaic
NDZ	Non-Detection Zone
VSC	Voltage Source Converter
IEEE	Institute of Electrical and Electronics Engineers
HV	High Voltage
LV	Low Voltage
PCC	Point of Common Coupling
MGMS	Microgrid Management System
VSCs	Voltage Source Converters
EMS	Energy Management System
VPP	Virtual Power Plant
HAN	Home Area Network

FAN	Field Area Network
WAN	Wide area networks
Qos	Quality of Service
P2P	Peer-to-peer
TX	Transmitter
RX	Receiver
LNA	Low Noise Amplifier
PA	Power Amplifier
GFSK	Gaussian Frequency Shift Keying
FIFI	First In First Out
SPI	Serial Peripheral Interface
ACK	Acknowledgement
CRC	Cycle Redundancy Check
LC	Local Controller
MC	Master Controller

Chapter 1: Introduction

The dominant structure for the generation and consumption of electricity over the past 130 years or so has been the radial power system with large generating power stations in remote areas connected via transmission lines that deliver the power to lower voltage distribution systems closer to the consumer [1]. Due to numerous factors, such as environmental pollution, global warming, gradual depletion of fossil fuel resources etc. there is considerable interest in the utilization of sustainable renewable energy systems. Coupled with this, the improved technological advances in the automation, power electronics, communications and information technologies has opened up new possibilities for cleaner power generation, with increased power quality demands, and the need for more reliable power delivery to protect against blackouts [2]. Renewable energy systems offer a sustainable solution towards generating reliable power.

Distributed Energy Resources (DER) integrate renewable energy (from sources like solar and wind) at the distribution level. DERs, along with Energy Storage (ES) systems at the distribution level, provide benefits such as peak load shaving and Uninterruptable Power Supply (UPS) capabilities.

Microgrids consist of multiple DERs and ES and are located near load centres where Distributed Generators (DG's) can supply power to the local load in parallel with the utility supply. In this manner, DG can help to reduce power demand from the national grid by delivering locally generated renewable power. In essence, a microgrid is a microcosm of the main power grid. Microgrids originated from a need to bring DG closer to the consumer rather than add distributed generators to the radial power grid further away from consumers. Microgrids are apportioned into smaller power grids and are now becoming essential delivering power to consumers [3].

Microgrids currently are operated as back-up units, to ensure reliable supply to the consumers whenever there is an outage at the utility level. They mainly facilitate in increasing the overall efficiency, reliability and stability while reducing the electricity cost. They are currently being realized mostly at the distribution level, but also have the

capability to be realized at higher voltage levels where they have the prospective to affect bigger sections of power grids.

A communication infrastructure within the microgrid enables the transfer of information from the local controllers (primary control) to the Master controller (secondary control) and vice versa to facilitate the overall management operation. A communication infrastructure can be deployed using either wired or wireless technologies. In either case, the overall communication link should be a robust network, so that the microgrids DERs, ES and loads can work effectively and securely.

1.1 Background

The traditional electric grid comprises three main stages: Generation, Transmission and Distribution. In the generation stage, the power is often generated by large power plants, such as nuclear and hydro. Usually they are located away from populated cities, so the electricity has to be transmitted over high voltage long transmission lines.

In the distribution stage, the high voltage is stepped down to a lower voltage before supplying it to the consumers. The traditional model of the distribution grid is changing due to microgrids, as they are primarily installed in the distribution grid closer to the consumers. Figure 1 depicts the structure of a traditional electric grid.

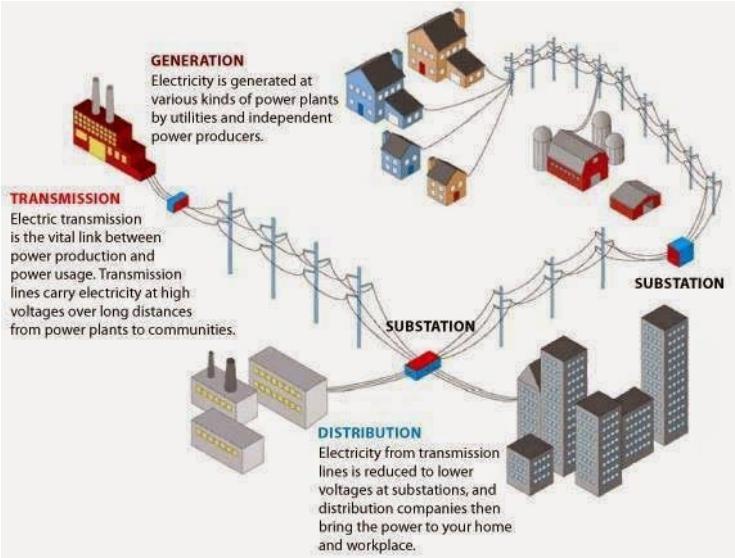

Figure 1: Traditional electric grid [49]

The traditional electric grid is a complex system and is designed in such a way that any single point failure can be avoided and a substation is usually designated to incorporate several microgrids and serve multiple neighborhoods.

1.2 Microgrid

The microgrid concept enables a reliable operation and eliminates the need of a central dispatch. Connection of microgrids to low voltage (LV) distribution level grid is economically and technically attractive. The re-design of the distribution system is not required as the use of the DG in a microgrid enables higher penetration. If a general or local blackout occurs, capabilities of local generation in the LV distribution level grid can be exploited to reduce customer interruption times by allowing microgrid islanded operation to feed local consumers until the main network becomes available and provides a fast-black start recovery in the low voltage grid [4].

A microgrid operates in either one of two modes:

1. Grid connected mode
2. Islanded mode

In grid connected mode, the transfer switch connecting to the microgrid is closed and the microgrid voltage and frequency is maintained by the grid. Within the microgrid, a DG provides the required active and reactive powers to both non-critical and critical loads.

In islanded mode, the transfer switch connecting to the microgrid is open and thereby isolating the main grid. The microgrid voltage and frequency is controlled by an internal converter connecting the DG and acting as a slack bus. DG's priority is to maintain power supply, both active and reactive power to a critical load. A basic generic microgrid architecture is shown in Figure 2.

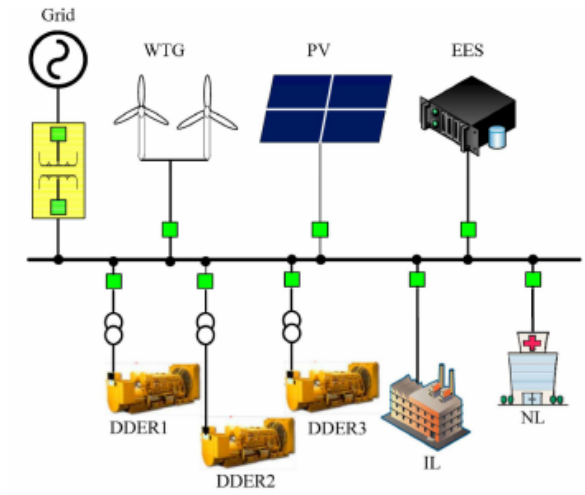

Figure 2: Microgrid architecture [7]

The microgrid is connected to the grid via a transformer at the Point of Common Coupling (PCC). DG's (wind and solar), energy storage (batteries) and both critical and non-critical loads are connected to each other at PCC. Although this is a basic microgrid architecture, PCC can expand according to the needs of the end user.

1.3 Microgrid Control Architecture

A crucial unit that controls the operation of the microgrid is the Microgrid Management System (MGMS) which operates the system autonomously, connecting it to the utility grid appropriately for the bi-directional exchange of power and providing support to the components within the microgrid. The MGMS, shown in Figure 3, is broken down into three different subsystems i.e. Primary, Secondary and Tertiary control layers that manage the entire microgrid operation [5].

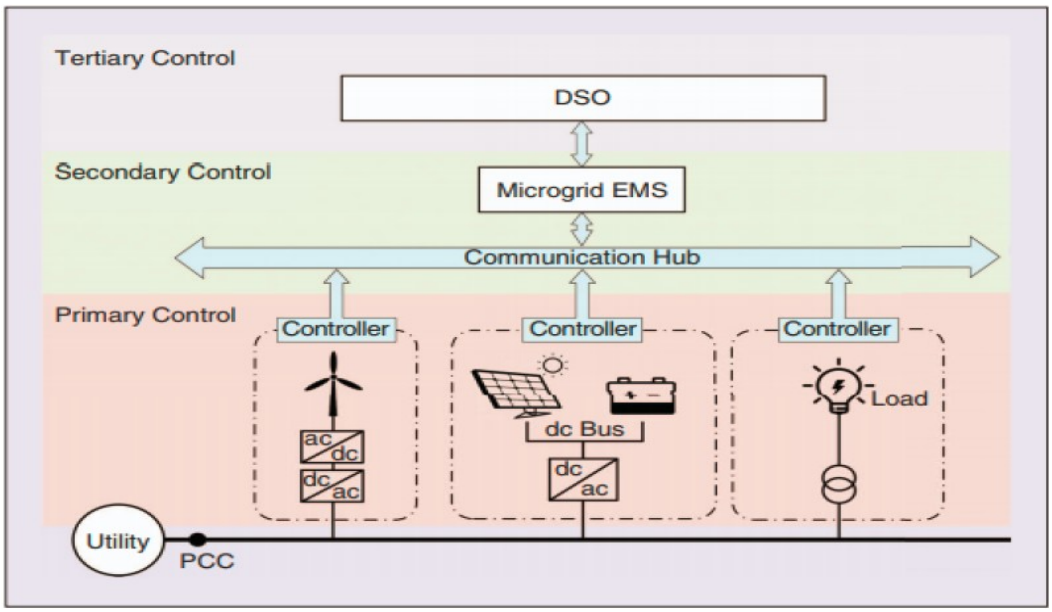

Figure 3: Microgrid Management System [5]

1.3.1 Primary Control Layer

This is the base layer that has the fastest response time (typically, in the region of milliseconds to minutes), which is responsible for the control of devices that respond to system dynamics and transients. It is also known as the local or internal controller. This control is based exclusively on local measurements and requires no communications. The function of this control includes frequency regulation, islanding detection, output control of inverter, power-sharing control and voltage regulation. Integration of voltage source converters (VSCs) due to the addition of DERs are common in the microgrid. VSC controller requires a specially designed control loop to simulate the inertia characteristic of synchronous generators and provide appropriate frequency regulation. The VSC has two stages of control: power-sharing control and inverter output control. The inverter typically comprises of an outer and inner control loop for voltage control and current regulation respectively. The power sharing control is used for the sharing of the active and reactive power in the system.

1.3.2 Secondary Control Layer

This is the central layer and its main function includes an Energy Management System (EMS) and automatic generation control. The secondary control also helps resets the

voltage and frequency deviations of the droop-controlled VSCs and generators, which then allocates new optimal long-term set points calculated from the microgrid EMS. The EMS minimizes the microgrid's operation cost and maximizes its reliability in grid-connected or islanded modes of operation. The objective of the EMS consists of finding the optimal Economical Dispatch (ED) and Unit Commitment (UC) of the accessible DER units, to achieve load and power balance in the system. The cost function is designed in terms of economic tolls such as shutdown and start-up costs, maintenance cost, emissions, power bill, battery degradation cost, fuel cost, social welfare and cost of load loss. The reliability indices are formulated as constraints such as energy storage capacity limits, generation and demand balance and power limits for all controllable generations. The EMS resolves a multi objective optimization problem with complex constraints and falls under mixed-integer linear/non-linear programing.

1.3.3 Tertiary Control Layer

This is the highest control layer and provides intelligence for the whole system. It is responsible for buying and selling of energy between consumers and Transmission system, as well provide active and reactive power support for whole distribution system. Tertiary control layer is not a part of the MGMS but is recognized as a subsystem of the utility distribution management system (DMS). But, due to the increase of microgrids in the distribution system, the tertiary control layer is evolving in a concept called Virtual Power Plant (VPP). The objective of a VPP is to coordinate the operation of multiple microgrids interacting with one another within the system and communicate needs and requirements from the main grid. The VPP can provide transmission system primary frequency support, energy market participation and reactive power support. The control layer response time is typically of the order of several minutes to hours, providing signals to secondary controls at microgrids and other sub-systems from the full grid.

The MGMS controls the DGs to maintain the balance between generation and load demand during islanded mode, grid-connected mode or the transition period between the two modes.

After understating the MGMS hierarchical control, a microgrid system simulation at the primary control layer is conducted, where the mode of operation is changed from grid-connected to islanded mode and along with that control of DG's to maintain reliable power to critical load is verified. In chapter 5, protocols to establish a two-way communication channel between the secondary control and primary control are investigated.

1.4 Literature review

Passive distribution networks are evolving into active distribution networks by integrating DGs. Large scale integration of DGs into distribution networks has attracted attention worldwide. Microgrids comprised of DGs to improve sustainability, protection, optimal power flow and decreased power cost for the consumers are discussed in [7,8,9,10]. Common barriers, experiences and ultimate success factors to implement a microgrid are discussed in [11].

Some of the negative impacts of increased DG penetration on the grid operation have been presented in [6]. These negative impacts are classified as voltage rise, reverse power flow, harmonic distortion, voltage sag/dip, voltage fluctuation/flicker, voltage unbalance, and frequency deviation etc. These negative impacts give rise to poor power quality delivered to consumers.

Reference [12] addresses key issues that microgrids face. Technical challenges faced by microgrids with respect to islanding, voltage-frequency (V-F) control and protection are reviewed.

One main function of a microgrid is to ensure stable operation after faults and various network disturbances. The main advantages of microgrids are discussed in [11,12,13] and are summarized below:

1. They can operate independently during islanded mode without connecting to the main distribution grid.
2. They can provide plug-and-play functionality for switching to a suitable mode of operation, either grid connected or in islanded mode of operation, and have the capability to resynchronize safely and re-connect to the main grid.

3. They can provide a good solution to supply locally generated power (even though in a limited fashion) in the case of an emergency (i.e. during power shortages and interruption in the main grid).

To achieve good overall performance and operation of a microgrid system requires knowledge of the mathematical modeling and control system design [14-23].

Reference [1] describes the model of a PV-Battery based DC microgrid system using PSCAD/EMTDC software. An isolated bidirectional DC-DC converter (IBDC) is implemented to charge and discharge the battery. Three different modes of operation and results are analyzed for proposed microgrid's energy management and power control.

Reference [14] has a model of a PV-Battery based microgrid system using real-time simulation with OPAL-RT OP5600 digital simulator. Behaviour of the microgrid was investigated at different levels of solar irradiance along with a storage battery to compensate for the PV output. Reference [15] describes the model of a PV-Battery based microgrid system using MATLAB/SIMULINK. Active/Reactive (P-Q) power and Voltage-Frequency (V-F) control strategies are implemented for grid connected and islanded modes of operation. Instead of conventional dq transformation, control strategies are designed in abc reference frames. Simulation results are observed to have a very fast response to the control.

In Reference [16], a flexible power electronics interface is developed for connecting the AC grid to the microgrid. Interface is comprised of a back-to-back Voltage Source Converter (VSC) to export variable active and reactive power to the microgrid. Harmonics are prevented from transferring from one side to another. A dq current decoupling control strategy are used for active power flowing bidirectionally, as well as providing reactive power compensation and keeping the microgrid voltage stable.

Reference [17] focused on the analysis of two charging modes of a battery for a stand-alone microgrid. The battery is connected to DG to charge an insufficiently charged battery bank through 2 charging modes. In mode 1, the battery performs Constant-Voltage Constant-Frequency (CVCF), which is controlled by PR voltage + P current control. In

mode 2, the DG performs CVCF control while BESS is charged by Constant-Current Constant-Voltage (CCCV), which is controlled by PI +R current control.

Reference [18] presented a strategy for synchronised control of PV with Maximum Power Point Tracking (MPPT) and battery storage control to provide coordinated voltage control or frequency support during microgrid operation. Reference [19] focused on the design and development of a PV power conditioning system for hierarchical control. Control strategies used for PV control are droop control for both active and reactive power sharing, inverter control using dq technique and PV-boost and battery bidirectional converter control. Reference [20] utilizes the droop control strategy during islanding mode. Grid-Supporting-Grid-Forming (GSGF) controls are implemented for the inverter which operates as droop control voltage source and current source. Power control in grid connected and islanding modes are shown in terms of simplified equations and recalculation of frequency reference is proposed in islanding mode. Reference [21] analysed and simulated a stationary Lithium-Ion battery system. PSCAD software is used for simulations. One-time constant model (OTC), two-time constant model (TTC) and three-time constant model (DTC) equivalent battery circuits are analysed along with its SOC, aging effects and temperature effects. Reference [22] has modelled a PV-Battery system with enhanced control for power quality. DC-DC and DC-AC converters are integrated to the DG. A dq current control based on PI controller is utilized for bidirectional flow of active and reactive powers along with a Harmonics Controller (HC) to improve power quality are implemented.

A DG system connected to the grid or loads via bidirectional inverters can cause power quality problems such as distortion in the waveform and grid instability. In order to provide high-quality power at the PCC and overcome the aforementioned problems, an appropriate controller with fast response, high tracking ability, less settling time, ability to remove steady state errors, compatible algorithm is required to reduce the Total Harmonic Distortion (THD) and achieve a purely sinusoidal output. In the literature, various controllers are proposed and designed to overcome the fore mentioned problems and achieve these qualities. Cascaded controllers, presented in literature [23-26], have an inner current loop and an outer loop. The inner current loop is vital towards the overall closed-loop controller performance of the system. Some of the control approaches, including

deadbeat [23], PI [24], H∞ [25] and μ-synthesis [26], are widely applied. In the mentioned above cases, the outer loop decreases the tracking error and improves the tracking ability.

Deadbeat method proposed in [23], is used to increase the robustness of the controller as it regulates the weighted average current to improve the grid harmonic distortions and stabilize the supply voltage. PI controller modified to fraction PI λ is presented in [24]. This makes the controller robust as the proposed PI controller has an additional degree of freedom λ along with its tuneable gains Kp and Ki. It is followed by a detailed modeling of the converter to consider the required phase margin to ensure acceptable damping. However, H∞ controllers [25] offers advantages of fast transient response and robustness over PI controllers and also to have a narrow range of stable operation and poor performance under disturbance parameter conditions. The μ-synthesis controllers are compared with H∞ controllers in [26] to solve the frequency control design problem in a microgrid. Performance and robustness of both μ-synthesis and H∞ controllers are examined and evaluated in the presence of parametric uncertainties and numerous disturbances. Results show that μ-synthesis controllers provide better performance when considering structured uncertainties with H∞ control method. Along with that, in comparison with PI controllers, μ-synthesis controllers reduce the order of PI controllers and therefore it improves the overall microgrid frequency control dramatically. Based on the aforementioned discussion, all types of controllers are able to properly track the reference values, and introduce other features and advantages such as μ-synthesis controllers.

A microgrid is designed to seamlessly transition between grid-connected and islanded modes of operation when unforeseen problems in the grid arise [12]. Reference [27] presented two modes of operation for a microgrid. In grid-connected mode, the DG's act as constant power sources and inject demanded active/reactive power (PQ mode) into the grid. In islanded mode, the DG's supply the power to the local loads only while maintaining the voltage and frequency (V/F mode) within acceptable operation limits. Seamless transition between grid-connected and islanded modes of operation is challenging, at best, and can result in power quality problems and islanding protection issues.

Detailed information about various islanding detection methods are presented in [28,29,30]. Islanding detection should be followed by control decision to maintain system stability and performance and matching the load to available generation while maintaining the power quality [28]. Islanding modes consist of two types: intentional (which are due to pre-planned events) or unintentional (which are due to accidental events).

Reference [29] reviewed three islanding detection techniques which are classified as passive, active or hybrid. Passive methods monitor the system parameters such as harmonic distortion, frequency, voltage and current on the DG site at the PCC with the utility grid. Active methods feed a small disturbance into grids and rely upon perturb and observe methods and help in deciding if the grid is in the islanding condition. Hybrid method is a combination of the passive and active methods. The active methods are applied only when islanding is detected, based on a passive technique.

Reference [30] focusses on the critical problems of islanding. For passive islanding method, its advantage is that it has no impact on power quality, but its disadvantage is the Non-Detection Zone (NDZ). The NDZ is the power difference between the load and the DG in which passive islanding scheme detects to fail. If the NDZ is relatively large then the detection time is difficult to predict resulting in the switch to fail in detect islanding. On the other hand, for an active islanding method, its advantage is that it has a very small NDZ, but the disadvantage is that the power quality will be degraded. NDZ is described in power mismatch space; it's the area where the mismatch percentage is small to reach a specific level islanding.

Wireless communication between the primary and secondary control is essential for the reliable, secure and robust operation of microgrid. Both wired and wireless technologies are employed to achieve a bidirectional communication for transmitting and exchanging data. Wired communication technologies are considered to be more reliable as they offer high data transmission bandwidth, but however they are expensive to be deployed as they have a high installation cost [31]. On the other hand, wireless communication technologies offer flexibility to add new remote terminal units (RTU) nodes to the existing communication network for future expansion, and moreover they have a low installation cost [32]. Therefore, wireless communication technologies are considered to be a better

option for microgrid applications as they can not only monitor and control sensors, meters and actuators, but also achieve the three main requirements; security to provide confidentiality of information, real-time performance guarantee by evaluating the transmission delay for various types of application within microgrid and extremely high availability to ensure non-interrupted service.

Reference [33] explains the working of wireless spectrums, networks and the economic associated with wireless communication, which lays a foundation for setting up a firm base for a low-cost wireless communication development. Reference [34] highlights the current challenges and future trends in the field of communication architectures for microgrids. It provides a guideline and a review of the transition from the current communication infrastructure to the future paradigm of communication infrastructure.

In Reference [35] impact of wireless communication system performance on the microgrid control is evaluated. Emphasis is mainly given to the communication system as it has a substantial impact towards the dynamic transitions in microgrid. Importance is given to the delay as it has to be considered for the controllers to be updated with new system status, if not the system will lose its stability. To overcome this problem, Reference [36] shows the latency and bandwidth requirements for various microgrid applications.

The most popular wireless technologies implemented for microgrid applications are: Bluetooth [31], ZigBee [37], WI-FI [38] and Radio Frequency [31]. These technologies are compared in chapter 5 based on various parameters to determine best suitable technology for microgrid wireless communication. The protocols are compared based on topology, security, bandwidth, transmission time and installation costs.

NRF24L01, a Radio Frequency transceiver offers to be an alternative solution for self-healing mesh networks. In reference [39], a comparative study in performed by analysing both NRF24L01 and ZigBee transceivers. It is analyzed that the NRF24L01 provides a better throughput, mesh routing recovery time, power consumption and low-cost solution when compared with ZigBee.

1.5 Technical challenges

1.5.1 Issues with technology

Integration of multiple generation sources and multiple components in the microgrid can be challenging when issues arise. If it cannot be individually implemented and operated successfully, overall operation of microgrid can be compromised. Issues can range from the efficiency, durability and economical operation of storage units and DG to the effective functionality of control software and communication.

Communication is considered to be one of the main challenges when DG's are connected as traditional grid was not designed to support bi-directional power flow. And the most difficult part could be maintaining a secure and reliable communication between all DG's and various components (relays, etc.) for the network management [40].

1.5.2 Dual-mode operation

Microgrid's plug and play functionality from grid-connected to islanded mode can be due to either a fault event at grid side or intentionally. Switching to island mode can be in two forms: black start or seamless transition. For a black start scenario, an outage is taken for a short period before the microgrid can be re-energized in islanded mode. And, for a second scenario, after disconnecting from the main grid within a very short time, a seamless transition to islanded mode is also complex. Both of these two forms of switching can be difficult to achieve.

Switching back to grid-connected mode also poses challenges. Re-synchronizing from islanded microgrid back to the grid after the fault is cleared requires carefully choosing the right moment to close the transfer switch to match the frequency of the grid voltage. Transitions between both modes can cause large mismatch between loads and generation that may need further voltage/frequency controls and active/reactive power controls [40].

1.5.2.1 Frequency and voltage control

Frequency and voltage are controlled by adjusting the active and reactive power of the DG. This will ensure both frequency and voltage remain within predefined limits of the set point values. During islanded mode of operation, one of the most challenging tasks it to operate

multiple DGs as it is essential to regulate the microgrid voltage by implementing a voltage vs reactive power droop controller. This can be a challenging task as the microgrid has to keep the frequency and voltage at rated values while meeting all the load demands.

1.5.2.2 P-Q control

The P-Q control is employed by the DGs when microgrid is operating in grid connected mode. In this mode, the microgrid controller no longer follows the V/F control strategy as the voltage and frequency of the microgrid is maintained by the grid. The inverter injects both active and reactive power into the grid, to meet load demands and also to operate to achieve an economic operation of microgrid.

1.5.3 Transfer Switch

Microgrid's mode of operation from grid connected to islanded mode is changed through a transfer switch. A time delay has to be considered to allow the feeder to be isolated before the DGs are allowed to deliver power to critical loads while the grid is disconnected [41]. When switching from islanded mode to grid-connected mode, synchronization conditions such as Voltage magnitude, Phase relationship and Frequency are verified by the static switch controller. If the grids synchronisation conditions are not met, then there will be a failure switching to grid-connected mode.

1.6 Scope of the thesis

This thesis focuses on the simulation of a generic microgrid consisting of a Photovoltaic (PV) and Battery Energy Storage System (BESS) and studies its operational performance using the MATLAB/SIMULINK software package.

A proof of concept bi-directional wireless communication network is to be established using a low-cost NRF24L01 transceiver. The network is to be implemented as a centralized configuration to communicate between the Primary Control (Local Controllers) and Secondary Control (Master Controller) for the exchange of information. Furthermore, LoRa, promoted as an infrastructure solution for Internet of Things, is utilized for long range and low power communication applications.

The microgrid has two modes of operation:

- In grid-connected mode, the microgrid voltage and frequency is maintained by the grid. Within the microgrid, a distributed generator provides the required active and reactive powers to both non-critical and critical loads.
- In islanded mode, the microgrid voltage and frequency is generated from an internal converter connecting the DG and acting as a slack bus. DG's priority is to maintain power supply, both active and reactive power to the critical load.

The microgrid is designed with control strategies to generate firing pulses for the converter switches. Vector control strategy is implemented during grid-connected mode, to control the active and reactive power (P-Q) independently. Voltage-Frequency (V-F) is implemented during islanded mode, to provide constant voltage and frequency reference to the microgrid.

Passive islanding detection is implemented to seamlessly switch mode of operation from P-Q to V-F mode when any disturbance is detected. Under/Over Voltage (UOV) and Under/Over Frequency (UOF) techniques are used to detect disturbance during any faults. The microgrid model is to be compliant with the IEEE 1547 standards. Tables 1 and 2 show the Voltage and Frequency limits based on IEEE 1547 standards.

Table 1 - IEEE 1547 Voltage Standard

Voltage Range V (pu)	Clearing time (s)
$V < 0.5$	0.16
$0.5 \leq V < 0.88$	2.00
$1.1 < V < 1.2$	1.00
$V \geq 1.2$	0.16

Table 2 - IEEE 1547 Frequency Standard

Frequency F (Hz)	Clearing time (s)
$F > 60.5$	0.16
$59.3 \leq F < 57$	0.16
$F < 57$	0.16

1.7 Outline of the thesis

The thesis is laid out as follows:

The introduction to the project is presented in chapter 1. The scope and the main objective of this project are also presented in chapter 1. Chapter 2 introduces the microgrid system. A proposed microgrid single line diagram is provided with detailed explanation of each element associated with the system. Chapter 3 discusses the control strategies for the microgrid. Vector-current control, Voltage-Frequency and islanding detection are discussed in detail. Chapter 4 provides the simulation results of the proposed system. Its steady-state operation is examined during grid-connected and islanded mode along with both Photovoltaic and Battery system. Chapter 5 focuses on the communication network present in the microgrid and compares existing technology's several parameters such as security, cost and bandwidth to identify the most suited protocols for wireless communication. Chapter 6 introduces NRF24L01 wireless module to resolve the concern of communication between the Master Controller and Local Controller. Chapter 7 introduces LoRa, a wireless communication technology developed specifically for long range and low power communication applications. Chapter 8 presents the conclusion and closing remarks. Recommendations for future work are also presented.

Chapter 2: Microgrid System

2.1 Introduction

In recent years, microgrid research has accelerated its focus on incorporating a greater number of renewable sources. In this chapter, the microgrid system is explained.

2.2 Microgrid System

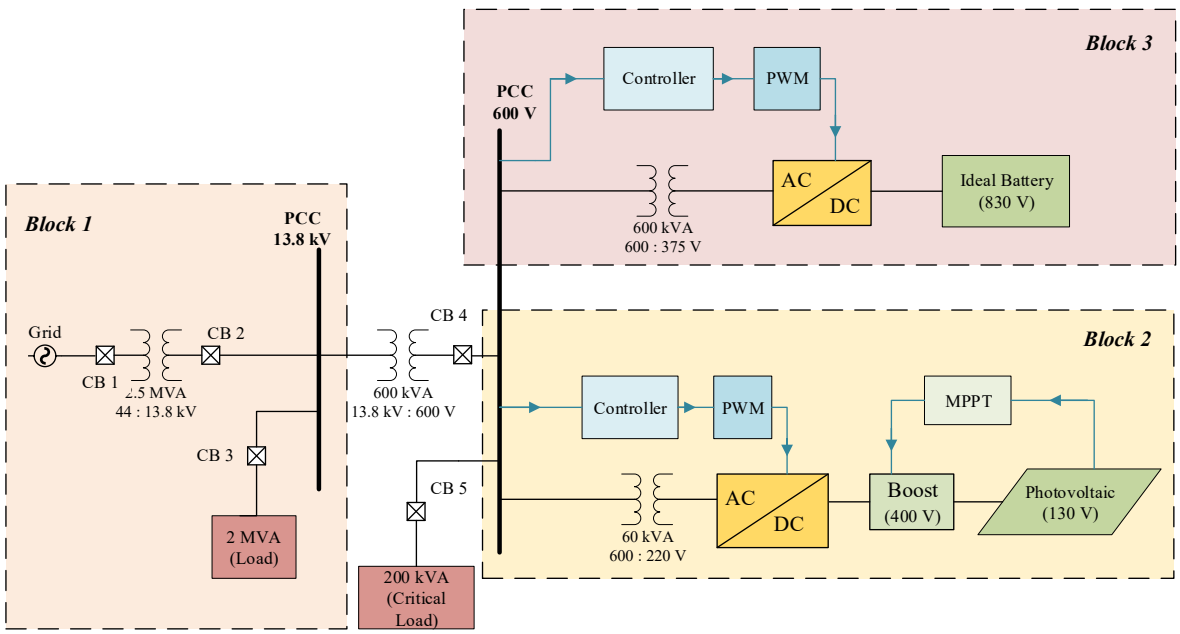

Figure 4: Microgrid System

The microgrid system modelled in MATLAB/SIMULINK consists of three major blocks (Figure 4):

1. Utility grid
2. Photovoltaic (PV) system
3. Battery Energy Storage system (BESS)

The system is interconnected at two Point of Common Coupling (PCC) buses, one at low voltage (600 V) and one at high voltage (13.8 kV). The Photovoltaic (PV) and Battery Energy Storage system (BESS) are connected in parallel to each other at the 600 V PCC along with a 200-kVA critical load. The critical load, which must be supplied under all conditions, consist of a mostly resistive load of 200 kVA. A transformer between the two

PCC buses steps up the voltage from 600 V to 13.8 kV. This transformer also electrically isolates the 600 V PCC and 13.8 kV PCC buses. The utility grid and some non-critical loads (totaling 2 MVA) are connected in parallel at the 13.8 kV PCC.

2.2.1 Utility Grid (Block 1)

Block 1 consists of an equivalent distribution grid behind a fixed impedance of 1 mH fed through a step-down transformer, rated at 2.5 MVA, 44 kV/13.8 kV, connected to the 13.8 kV PCC bus through Circuit Breaker CB 2.

2.2.2 Photovoltaic (Block 2)

Block 2 consists of a PV module, rated at 50 kW, 130 V DC. The output voltage of the PV module is stepped up by a DC-DC boost converter to 400 V DC. A Voltage Source Inverter (VSI) and 50-kVA transformer is used to step-up the voltage to 600 V to supply the PCC bus. The DC-DC boost converter is controlled with a Maximum Power Point Tracking (MPPT) algorithm that allows the PV to generate maximum power at all times. The Voltage/Current sensors measure readings at 600 V PCC bus to provide inputs into the VSI to generate the firing pulses.

2.2.3 Battery Energy Storage System (BESS) (Block 3)

Block 3 consists of an ideal battery along with a bi-directional VSI capable of working in either rectifier or inverter modes. The 600-kVA transformer in series steps up the voltage from 375 V to 600 V and feeds into the PCC. Voltage/current sensors measure readings from 600 V PCC to provide inputs to control block to generate firing pulses for the converter switches

2.2.4 Loads

There are two loads connected to the system: a critical load which requires a high degree of power quality and reliability, and a non-critical load which requires a lower quality of service. The critical load is rated at 200 kVA and is connected through circuit breaker CB 5 to the 600 PCC. The non-critical load is rated at 2 MVA and is connected through circuit breaker CB 3 to 13.8 kV PCC.

2.3 Breakdown of Microgrid System

The sub system elements of the microgrid are described below.

2.3.1 Photovoltaic system

A single-diode model of the PV system is shown in Figure 5. This is a fundamental model, which is used to represent a single PV cell and its electric characteristics. In this model, I_{PH} (current source) represents the light-induced current which is generated by the irradiance. A diode in parallel to I_{PH} represents the p-n junction of the PV cell. A shunt resistance R_{SH} accounts for the leakage currents caused by the impurities of the p-n junction. A series Rs resistance represents the distributed ohmic resistance of the PV model.

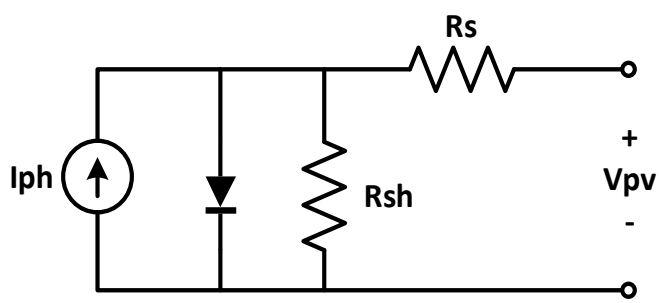

Figure 5: Ideal PV model [29]

The PV array is based on the Panasonic SCI250P BBB model within the Simulink library. Manufacturer of the solar module gives parameters needed to model the PV. The parameters of the SCI50P BBB essential to model the PV array are given in Table 3.

Table 3 - Parameters of SCI50P BBB

Open circuit voltage (V_{oc})	37.71 V
Short-circuit current (I_{sc})	8.74 A
Power at maximum power point (P_{mpp})	250.2502 W
Voltage at maximum power point (V_{mpp})	30.26 V
Current at maximum power point (I_{mpp})	8.27 A

A single solar cell was modelled first; later, it is extended to model a PV module and finally extended to model the PV array. The following equations describe the cell output voltage and current [33].

$$I = N_p(I_{ph} - I_d * \left[e^{\left(\frac{q\left(\frac{V}{N_S}\right)}{A.K.T_c} \right)} - 1 \right] \tag{2.1}$$

$$I_{ph} = N_p[I_{sc} * \emptyset_n + K_I(T_e - T_r) \tag{2.2}$$

$$I_d = I_{or}(\frac{T_c}{T_r})^3 * e^{\frac{q*E_g(\frac{1}{T_r} - \frac{1}{T_C})}{A*K}} \tag{2.3}$$

$$\emptyset_n = \frac{s}{1000} \tag{2.4}$$

Variables from equations (2.1-2.4) are defined in Table 4.

Table 4 - Variable defined from equations (2.1 - 2.4)

$\emptyset_n$	Normalized Irradiance
A	Diode quality factor
E_g	Band gap of the semiconductor
I_{ph}	Photo generated current
I_{or}	Cell's reverse saturation current
I_{sc}	Short circuit current at standard conditions
K	Boltzmann's constant
K_I	Cell's short circuit current temperature coefficient
N_p	Number of parallel connected cells
N_s	Number of series connected cells
Q	Electron electrical charge
R_s	PV cell series resistance
R_p	PV cell shunt resistance
S	Solar irradiance
T_c	Cell temperature in degrees Kelvin
T_r	Reference temperature in degrees Kelvin
V_{oc}	Open circuit voltage

Various characteristics have been derived from the SIMULINK model to illustrate and verify the I-V and P-V characteristics of the PV array. This curve is non-linear and primarily relies on the temperature and on the solar irradiation. Figure 6 shows the I-V and P-V characteristics of the PV at fixed a temperature but with different irradiance values. It can be observed that when the irradiance increases, the current is increased more than the voltage and the maximum power point increases as well.

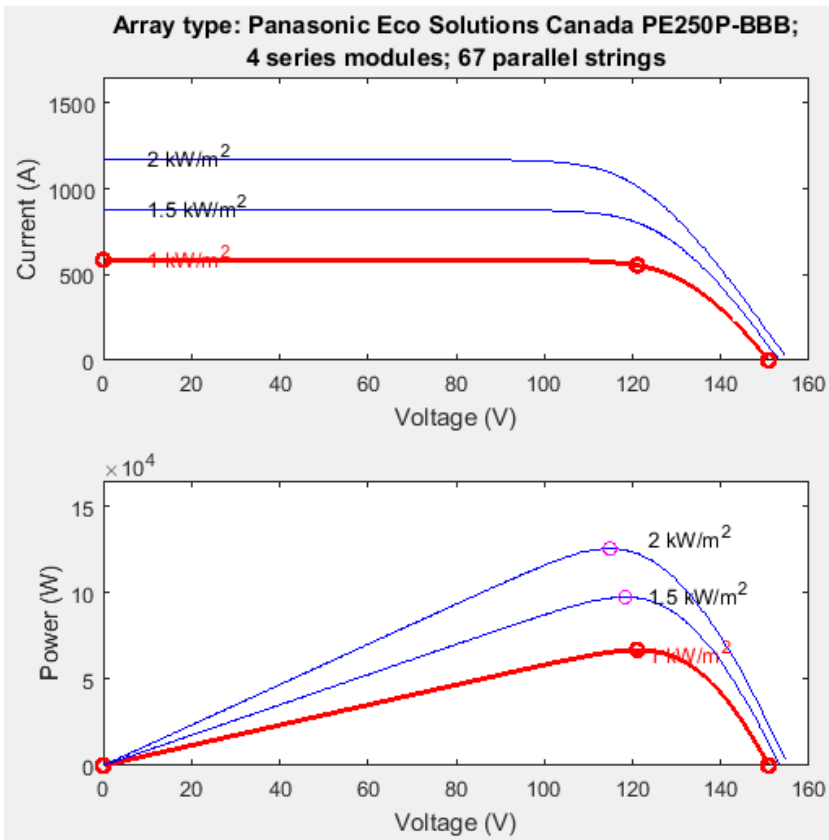

Figure 6: I-V and P-V characteristics

Figure 7 shows the I-V and P-V characteristics of the PV at fixed irradiance but at different temperatures. It can be observed that when the temperature increases, the current is changed less than the voltage and the maximum power point decreases as well.

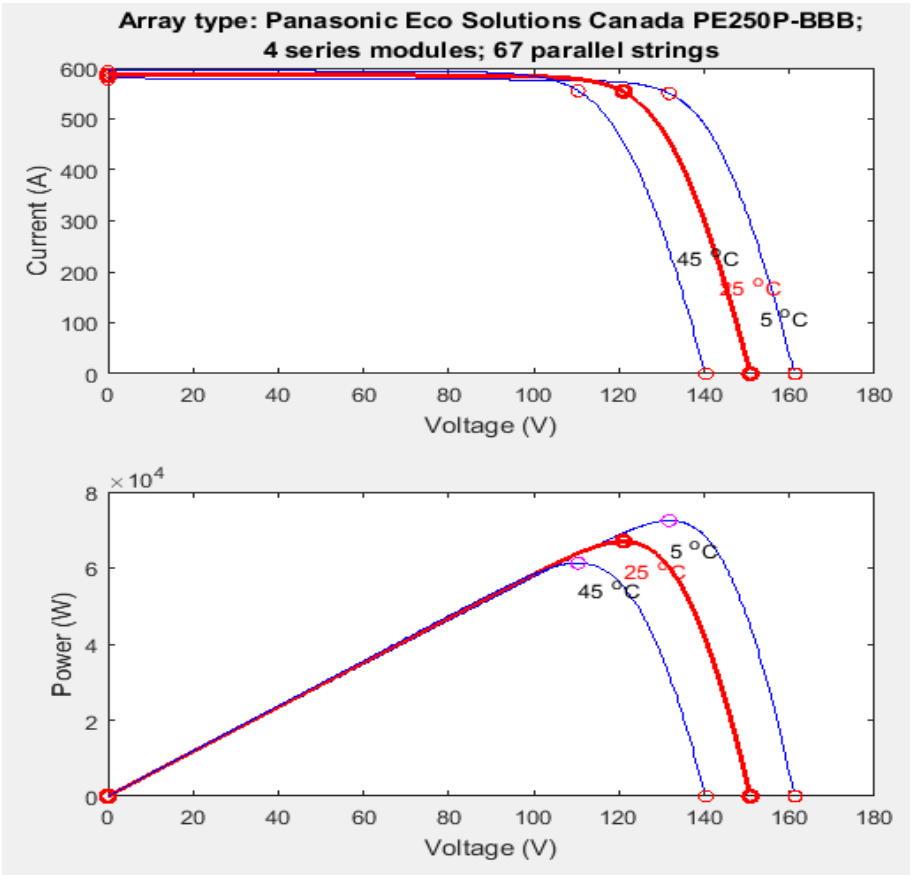

Figure 7: I-V and P-V characteristics

2.3.2 Boost converter

The main purpose of the DC/DC boost converter is to convert the low DC input voltage from the PV into a higher DC voltage necessary for the inverter in the following stage. A Maximum Power Point Track (MPPT) algorithm is used to control the DC/DC boost converter power at the maximum power point.

In Figure 8, a boost converter consists of a DC voltage source, inductor, switch, diode, capacitor and load. The switch is periodically is turned on and off, so that the energy stored in the inductor is transferred to the capacitor and the load. This transferred energy will result in boosing up the output voltage.

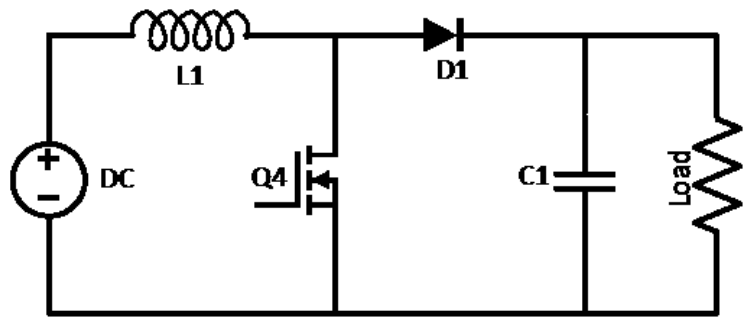

Figure 8: Boost converter [30]

The duty cycle from the MPPT controller is to control the switch of the boost converter. The Pulse Width Modulation (PWM) controls the opening and closing of the switch hence controlling the duty cycle D. Formula for duty cycle is given as:

$$\frac{V_0}{V_{in}} = \frac{T_s}{t_{off}} = \frac{1}{1-D} \tag{2.5}$$

Variables from equations (2.5) are defined in table 5

Table 5 - Variables defined from equation (2.5)

D	Duty cycle
T_s	Switching period
T_{off}	Switching off, of the IGBT
V_o	Average output voltage

The basic operation of boost converter is as follows: when the switch is on, the source charges the inductor and the diode is reversed biased. When the switch is off, the energy stored within the inductor is transferred to the capacitor resulting in a boost for the output voltage. The boost converter also has 2 modes of operation; continuous conduction mode (CCM) and discontinuous conduction mode (DCM).

The following equations are used to calculate the estimated values for the components of boost converter [34]. Variables from equations (2.6-2.8) are defined in table 6

$$L \geq \frac{V_o * D * (1-D)}{f_s |\Delta I_L|} \tag{2.6}$$

$$C \geq \frac{I_o * D}{f_s \Delta V_o} \tag{2.7}$$

Table 6 - Variables defined from equations (2.6-2.7)

D	Duty cycle
f_s	Switching period
V_o	Maximum of the dc component of the output voltage
ΔI_L	Ripple current of the inductor
I_o	Output current at maximum output power
ΔV_o	Output ripple voltage

2.3.3 Maximum Power Point Tracking

Maximum Power Point Tracking (MPPT) algorithm is used for extracting maximum available power from the PV module based on amount of solar irradiation and ambient temperature. In the incremental conductance (IC) method, the algorithm predicts the effect of a voltage change by measuring incremental changes in PV current and voltage. Several algorithms have been introduced in literature. This PV model utilizes the IC algorithm as it can track the changing conditions more rapidly than the perturb and observe (P&O) method.

Figure 9 shows the Incremental Conductance (IC) method flow chart. dI is the increment of the current, while dV is the increment of the voltage. I/V is considered to be the array conductance and dI/dV is the incremental conductance.

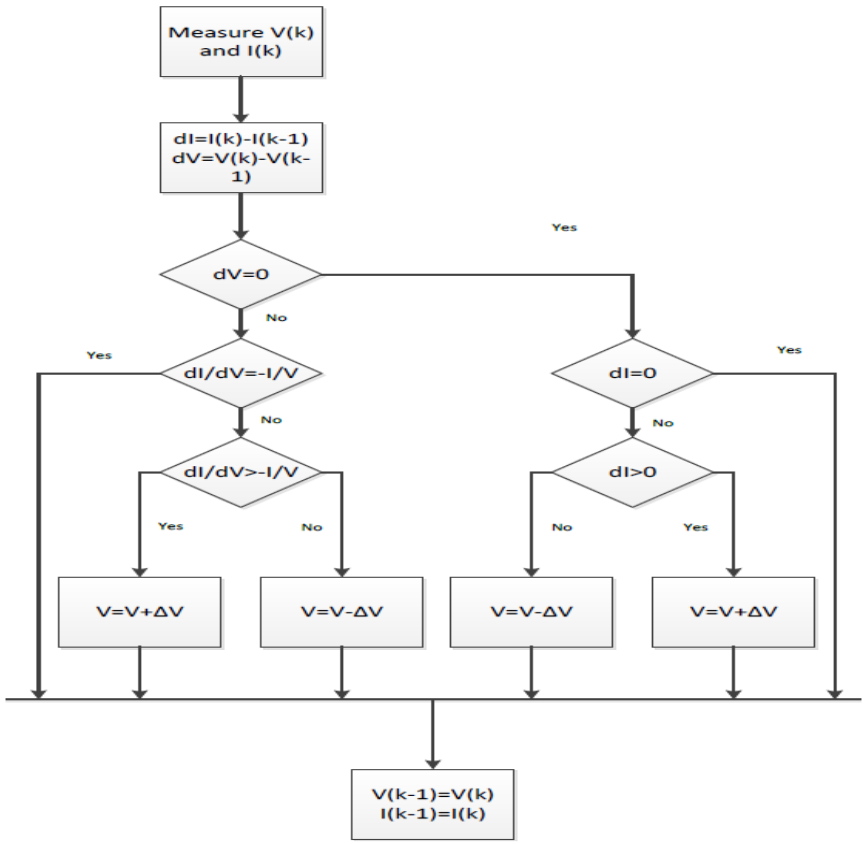

Figure 9: Incremental conductance (IC) flow chart [31]

The IC algorithm senses the output voltage and current of the PV module. The maximum power point is tracked by comparing the incremental conductance (dI/dV) to the array conductance (I/V). When the IC is zero (dV = 0 and dI = 0) then the condition is not changed and the MPPT is still operating at the MPP until the change in irradiance is encountered. This change will then be encountered by the MPPT to increase or decrease the PV array operating voltage to track the MPP. This process is repeated until a new maximum power point is reached [44].

2.3.4 Battery System

In the literature, there are three types of battery models; electrochemical, experimental and electric circuit based. Elimination of State of Charge (SoC) in electrochemical and experimental models make them a non-ideal choice to represent the cell dynamics. However, the electric circuit-based models make an ideal choice to represent the SoC and electrical characteristic of batteries. A battery model consisting of a voltage source in series with a resistance is shown in Figure 10. It is a generic dynamic model parameterized to represent some of the most common used battery technologies such as Lead-Acid, Nickel and Lithium-Ion.

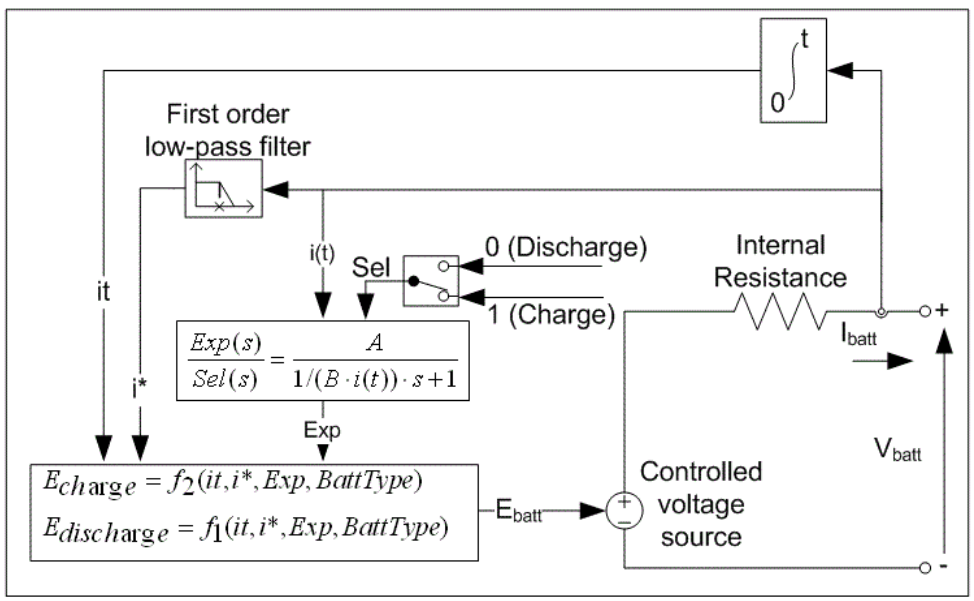

Figure 10: Battery equivalent circuit [50]

Lead-Acid [50]:

Lead-Acid consist of three main elements; lead oxide, lead and sulfuric acid. Some of its advantages include mature technology and low cost. Some of its disadvantages include heavy weight, self discharge, low energy and power due to heave lead collectors. The Lead-Acid model uses the following equations for the discharging and charging modelling.

Discharge Model ($i^* > 0$)

$$f_1(it, i*, i, Exp) = E_0 - K \cdot \frac{Q}{Q-it} \cdot i* - K \cdot \frac{Q}{Q-it} \cdot it + Laplace^{-1}\left(\frac{Exp(s)}{Sel(s)} \cdot 0\right) \quad (2.8)$$

Charge Model ($i^* < 0$)

$$f_2(it, i*, i, Exp) = E_0 - K \cdot \frac{Q}{it+0.1 \cdot Q} \cdot i* - K \cdot \frac{Q}{Q-it} \cdot it + Laplace^{-1}\left(\frac{Exp(s)}{Sel(s)} \cdot \frac{1}{s}\right) \quad (2.9)$$

Nickel [50]:

Nickel Cadmium (NiCad) and Nickel Metal Hydride (NiMH) are most used battery technologies. NiCad performance is not affected by the over discharged and over charged over time, which make this the most stable performance technology. However, as cadmium is considered poisonous; it is banned in most countries for industry applications. Whereas, NiMH batteries power density and its safe use has its advantages over NiCad, but due to its low energy density make it a poor technology when compared with Lithium-Ion. The Nickel model uses the following equations for the discharging and charging modelling.

Discharge Model ($i^* > 0$)

$$f_1(it, i*, i, Exp) = E_0 - K \cdot \frac{Q}{Q-it} \cdot i* - K \cdot \frac{Q}{Q-it} \cdot it + Laplace^{-1}\left(\frac{Exp(s)}{Sel(s)} \cdot 0\right) \quad (2.10)$$

Charge Model ($i^* < 0$)

$$f_2(it, i*, i, Exp) = E_0 - K \cdot \frac{Q}{|it|+0.1 \cdot Q} \cdot i* - K \cdot \frac{Q}{Q-it} \cdot it + Laplace^{-1}\left(\frac{Exp(s)}{Sel(s)} \cdot \frac{1}{s}\right) \quad (2.11)$$

Lithium-Ion [50]:

Materials used in Lithium-Ion (Li-Ion) batteries are: Iron Phosphate, Cobalt Oxide, Nickel Cobalt Aluminum Oxide, Manganese Oxide and Nickel Manganese Cobalt Oxide. Li-ion based batteries offer higher energy than Nickel and Lead-Acid as it has long life cycle, high specific energy (100 Wh/kg) and recyclability. The Lithium-Ion model uses the following equations for the discharging and charging modelling.

Discharge Model ($i^* > 0$)

$$f_1(it, i*, i) = E_0 - K \cdot \frac{Q}{Q-it} \cdot i* - K \cdot \frac{Q}{Q-it} \cdot it + A \cdot \exp(-B \cdot it) \quad (2.12)$$

Charge Model ($i^* < 0$)

$$f_2(it, i*, i) = E_0 - K \cdot \frac{Q}{it+0.1 \cdot Q} \cdot i* - K \cdot \frac{Q}{Q-it} \cdot it + A \cdot \exp(-B \cdot it) \quad (2.13)$$

Variables for equations (2.8-2.13) are:

E_{Batt}	Nonlinear voltage, in V
E_0	Constant voltage, in V
$Exp(s)$	Exponential zone dynamics, in V
$Sel(s)$	Represents the battery mode. $Sel\ (s) = 0$ during battery discharge, $Sel\ (s) = 1$ during battery charging
K	Polarization constant, in V/Ah, or polarization resistance, in Ohms
i^*	Low frequency current dynamics, in A
i	Battery current, in A
it	Extracted capacity, in Ah
Q	Maximum battery capacity, in Ah
A	Exponential voltage, in V
B	Exponential capacity in Ah^{-1}

2.3.5 DC/AC Inverter

The main purpose of the DC/AC inverter is to convert DC input voltage from boost converter into AC voltage. DC/AC converters play an essential role when delivering power to the load or connecting to three-phase grid power. Various control techniques can be implemented in the DC/AC converter to achieve optimum results.

Figure 11 shows the equivalent circuit of three-phase inverter. It is represented with six switches and six parallel diodes. The switches are controlled by Pulse Width Modulation (PWM) that turn on and off to obtain a sinusoidal output.

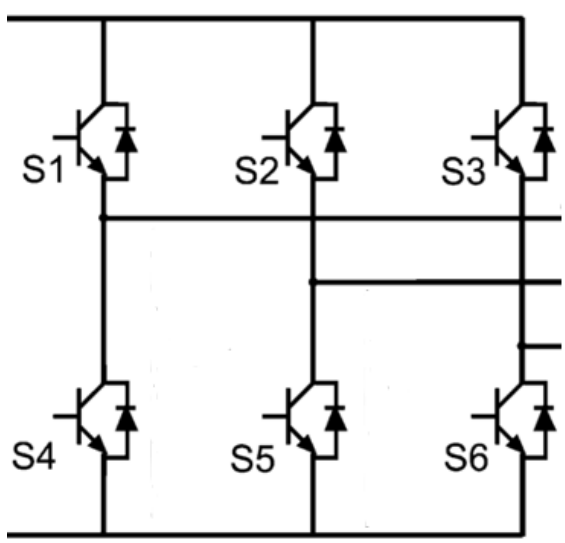

Figure 11: Three-phase inverter [32]

To obtain the PWM pulses, a three-phase sine wave - called the reference voltage - is compared with a triangle (carrier) waveform to generate three-phase pulses for the inverter. The converter switches are controlled by pulses having a $0^o, 120^o, 240^o$ phase shift for S1, S2, S3 whereas for S4, S5 and S6 the phase shift is $180^o, 300^o, 60^o$ respectively.

2.3.6 Filters

The main purpose of three-phase harmonic filters is to decrease the voltage/current distortion. Nonlinear converters such as Voltage Source Converters (VSI) generate harmonic voltages or harmonic currents which are injected into the power system. Harmonic filters reduce this distortion by diverting harmonic currents into low impedance paths.

Three-phase line reactors are used to limit line currents and are connected in series with the VSI. These reactors reduce any spikes of current and limit any peak fault currents.

A second order filter, shown in Figure 12, is also implemented which has two passive LC elements. Inductor represents the line reactor and capacitor is to further attenuate switching frequency components. Capacitor is calculated from the following equation. Variables from equations (2.8) are defined in Table 7.

$$f_c = \frac{1}{2\pi\sqrt{LC}} \tag{2.14}$$

Table 7 - Variables defined from equation (2.8)

L	Inductor
C	Capacitor
f_c	Cut-off frequency

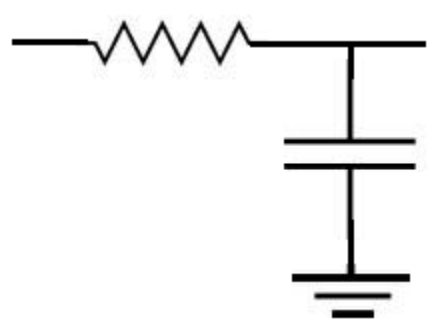

Figure 12: LC filter

Chapter 3: Control Strategies for VSC

3.1 Introduction

Microgrid has two modes of operation; grid connected mode and islanded mode shown in Figure 13. These operations are as follows:

- Vector-current control to regulate instantaneous active and reactive powers independently for VSC
- Voltage-Frequency (V-F) control mode to maintain power supply along with both active and reactive power to the critical load.
- UOV/UOF passive islanding detection to detect islanding using IEEE 1547 standards. Mode of operation is switched from grid connected to islanded mode.

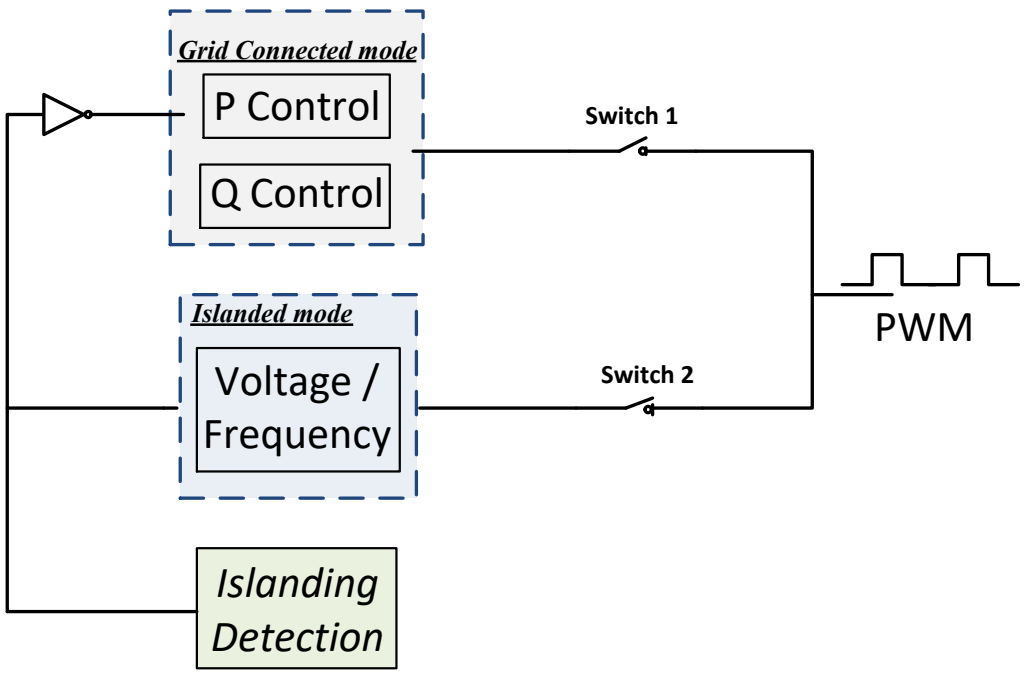

Figure 13: Overview of control scheme

3.2 Vector-current control

The main purpose of vector control is to regulate instantaneous active and reactive powers independently for the VSC. The control technique is accomplished by having outer and inner loop controllers. Using a dq decomposition technique, outer loop uses the d-

component to control active power (P control), and the q-component to control reactive power (Q control).

The following equations have been derived referring to Figure 14, to analyze the control strategy equations in detail.

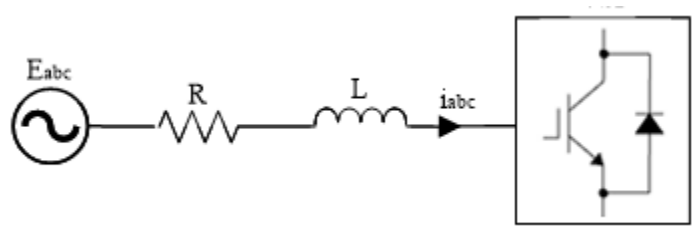

Figure 14: Schematic representation of VSC [32]

By using grid voltages E_{abc} as phase references, it can be described as:

$$E_{abc} = L\frac{d}{dt}i_{abc} + v_{abc} + Ri_{abc} \tag{3.1}$$

Where v_{abc} are converter input voltages, while i_{abc} are grid currents, R and L are resistance and inductance respectively between the converter and the grid [46].

Three-phase currents and voltages are transformed into dq reference frame by means of abc to dq transformation, where ω is the system frequency in rad/s.

$$\begin{bmatrix} E_d \\ E_q \end{bmatrix} = L\frac{d}{dt}\begin{bmatrix} i_d \\ i_q \end{bmatrix} + \omega L\begin{bmatrix} 0 & -1 \\ -1 & 0 \end{bmatrix}\begin{bmatrix} i_d \\ i_q \end{bmatrix} + R\begin{bmatrix} i_d \\ i_q \end{bmatrix} + \begin{bmatrix} v_{sd} \\ v_{sq} \end{bmatrix} \tag{3.2}$$

After the transformation in dq reference frame, the voltage equations are:

$$E_d = L\frac{d}{dt}i_d - \omega L i_q + v_d + Ri_d \tag{3.3}$$

$$E_q = L\frac{d}{dt}i_q + \omega L i_d + v_q + Ri_q \tag{3.4}$$

From equations 3.3 and 3.4, it is observed that the $d\ and\ q$ axes are decoupled from each other but are only related to each other by means of $\omega L i_q$ and $\omega L i_d$.

The power exchange in dq reference frame is given by:

$$P = v_d i_d + v_q i_q \tag{3.5}$$

3.2.1 Initial inputs to Controller

Figure 15 shows the overall view of the controller. All measured signals entering the VSC controller are first converted to pu values and then filtered by an anti-aliasing low-pass filter with a cut-off frequency of 2000 Hz. The VSC controller block will be described in section 3.2.2. Output of the controller is a three-phase voltage reference waveform, which is then compared with a triangular wave to generate PWM firing pulses for the VSC switches.

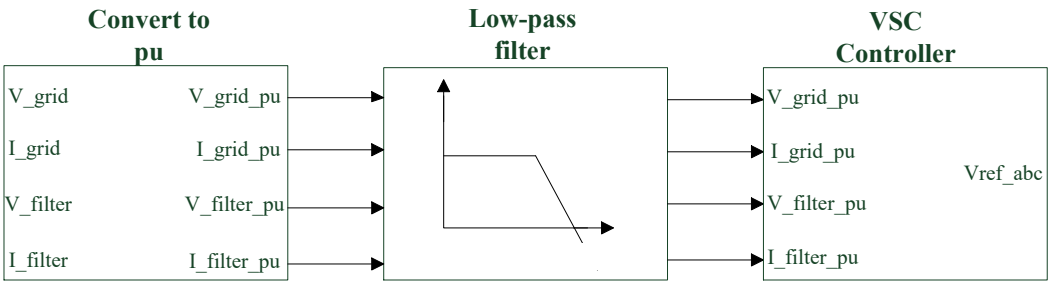

Figure 15: Overall block diagram of controller

3.2.2 VSC Controller

Figure 16 shows the block schematic of VSC controller. The Clarke transformation, dq transformation and signal calculations blocks are required to compute the variables needed for the outer and inner controllers. Active and reactive powers along with AC voltage are calculated in the signal calculations block.

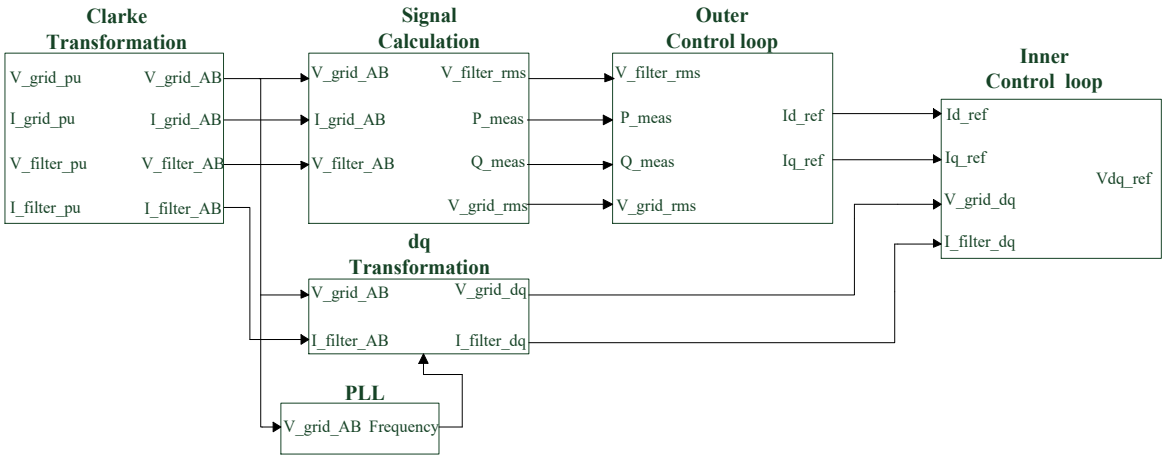

Figure 16: Block schematic of VSC controller

3.2.2.1 Clarke Transformation

The Clarke transformation block transforms the three-phase voltage and currents to stationary frame by using the following equation

$$\begin{bmatrix} x_\alpha(t) \\ x_\beta(t) \end{bmatrix} = \begin{bmatrix} \sqrt{\frac{2}{3}} & -\frac{1}{\sqrt{6}} & -\frac{1}{\sqrt{6}} \\ 0 & \frac{1}{\sqrt{2}} & -\frac{1}{\sqrt{2}} \end{bmatrix} \begin{bmatrix} x_a(t) \\ x_b(t) \\ x_c(t) \end{bmatrix} \tag{3.6}$$

Where x_a, x_b and x_c represent the three-phase stationary reference frame components and the components projected onto the two stationary orthogonal axes are x_α and x_β. Figure 17 shows the Clarke transformation vector

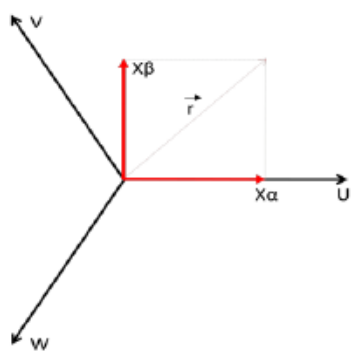

Figure 17: Clarke transformation vector [32]

3.2.2.2 Park Transformation

The Park (dq) transformation block is then used to transform x_α and x_β from the stationary reference frame to the synchronous rotating frame. This synchronous rotating frame is rotated with ω(t) ($\omega = \frac{d\theta}{dt}$), representing the angular frequency of the grid voltage in rad/s. The phase angle theta (θ) is found by the PLL allowing the synchronization of grid voltage with DG voltage. The following equation 3.7 is used to form dq transformation, and Figure 18 shows the dq transformation vector

$$\begin{bmatrix} X_d \\ X_q \end{bmatrix} = \begin{bmatrix} \cos\omega t & \sin\omega t \\ -\sin\omega t & \cos\omega t \end{bmatrix} \begin{bmatrix} X_\alpha \\ X_\beta \end{bmatrix} \tag{3.7}$$

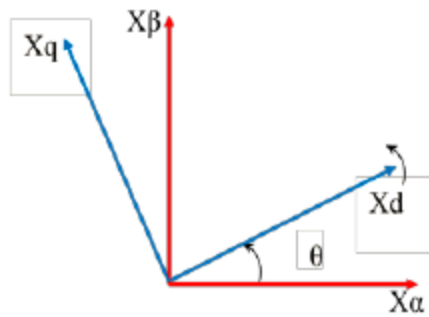

Figure 18: dq transformation vector [32]

3.2.2.3 Phase Lock Loop

The main function of the PLL is to synchronize with the phase angle and frequency of the AC grid voltage. Inputs of the PLL are the Park transformation voltages measured on the grid side and the output is the tracked phase angle. The synchronization is of a dq reference frame vectors is done in such a way that the grid voltage vector is chosen to align with the d-axis reference ($V_d = V_{grid}$) and the q-axis voltage to zero ($V_q = 0$).

3.2.2.4 Outer Control Loop and Inner Control Loop

The outer control loop shown in Figure 19 consists of an active power controller and reactive power controller. Depending on which functionality is desired, the control of both active and reactive power can be controlled in either inverter or rectifier modes. The outer control loop creates dq-current component reference values for inner current controllers.

As the grid voltage vector is aligned with the d axis, the q component of the grid voltage is equal to zero and d component equal to the voltage magnitude. The equations for both active and reactive power referring to equation (number) becomes:

$$P = v_d i_d \tag{3.8}$$

$$Q = -v_d i_q \tag{3.9}$$

An accurate active and reactive power control is achieved by using a PI controller. The outer controller takes the error between the measured and reference of both active (P_{ref}) and reactive (Q_{ref}) powers. This error is carried through the PI regulators and I_{dq} reference is obtained from equations (3.8) and (3.9)

In Figure 19, the outer controller loop's active and reactive control equations are represented as:

$$i_{d_{ref}} = \frac{1}{v_d}\left(k_p + \frac{k_i}{s}\right)\left(P_{ref} - P\right) \tag{3.10}$$

$$i_{d_{ref}} = -\frac{1}{v_d}\left(\frac{k_i}{s}\right)\left(P_{ref} - P\right) \tag{3.11}$$

As explained earlier, inner current control loop is used to decouple the current into d and q components. The inner controller, as shown in Figure 19, initially has the same functionality as the outer controller, except the decoupling terms from (3.3) and (3.4) are compensated by feed-forward. As a result, desired converter voltage in dq reference frame is obtained.

The output of the inner control loop is again converted to abc transformation along with the PLL for synchronization of the inverter and grid. Pulses are generated to fire the IGBT switches in the converter to enable the charge and discharge performance of the battery.

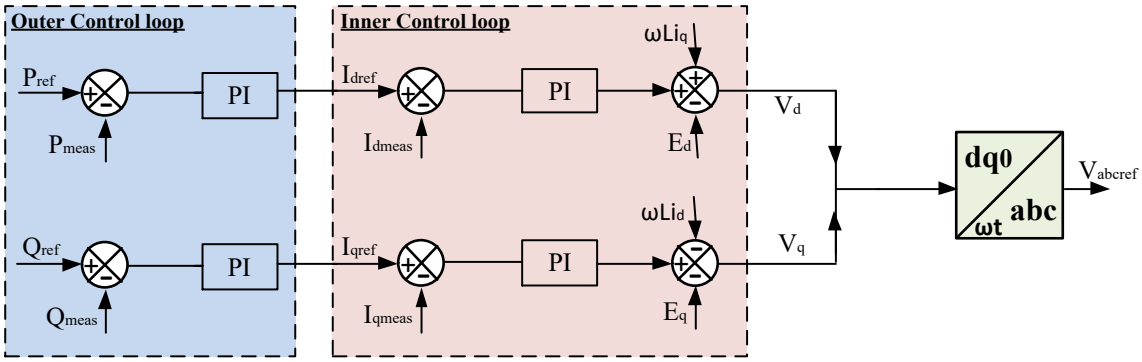

Figure 19: Grid connected mode of operation

3.3 Voltage-Frequency control

Any change in voltage or frequency caused by a disturbance in the network is sensed by the islanding detection logic (UOV/UOF) resulting in load shedding and isolation from the main grid. A trip signal is sent to the circuit breakers connected to the main grid and non-critical load to disconnect, resulting in a microgrid formation.

Mode of operation, explained in section 1.2, is switched from active and reactive (P-Q) control to voltage/frequency (V/F) control. V/F is initialized so that the voltage and frequency reference is provided to the PV and critical load.

Figure 20 shows the block diagram of V/F control. The reference voltage V_{ref} is compared with droop voltage. Following this, it is then compared with measured voltage V_{meas} and the error is given to the PI controller. The output of the PI controller is forced to 1 pu with the addition of V_{error}. The frequency is added to the voltage ref (V_{d_ref}) through the addition of Id. As grid voltage vector is aligned with the d axis, the following equation can be derived:

$$V_{d\_ref} = \left(V_o + \Delta V_{grid}\right) + H_{HP}(s) i_d \tag{3.12}$$

$$V_{q\_ref} = 0 \tag{3.13}$$

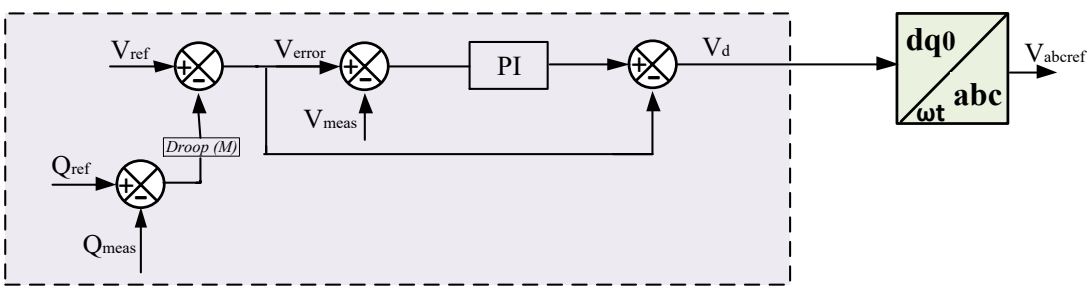

Figure 20: Islanded mode of operation

3.4 Islanding Detection

Passive islanding using Under/Over Voltage (UOV) and Under/Over Frequency (UOF) has been applied to detect any fluctuations during any disturbances. As per IEEE 1547 standards, discussed in section 1.5, the UOV and UOF logic has been implemented. This method uses two main system parameters, voltage and frequency at the PCC to detect islanding by having threshold values to monitor the variations. Figures 21 and 22 show the algorithms UOV and UOF respectively that were used to implement the passive detection method [47].

Figure 21 shows the control logic used to detect the Under/Over Voltage (UOV) for the system. The two minimum and two maximum voltage limits are set for normal operation. Whenever the voltage at PCC exceeds these limits, the UOV command will be triggered after certain time delays as shown. This triggered signal will be initiating a disconnection logic sequence resulting in the microgrid disconnection from the utility grid and non-critical load.

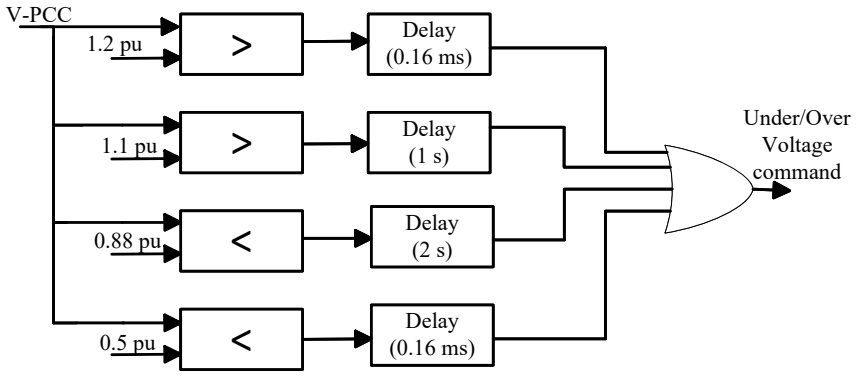

Figure 21: UOV Logic circuit

Figure 22 shows the logic used to detect the Under/Over Frequency (UOF) for the system. The UOF command is implemented in a similar manner where the frequency at PCC is compared with the two minimum and one maximum limits. Whenever these limits are exceeded, they will trigger the UOF signal after pre-set time delays as shown. This triggered signal will be initiating a disconnection logic sequence resulting in the microgrid disconnection from the utility grid and non-critical load.

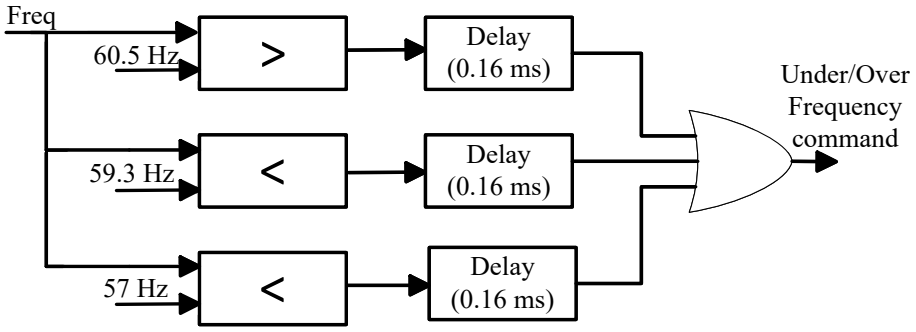

Figure 22: UOF Logic circuit

Chapter 4: Simulation results and analysis

4.1 Introduction

This chapter focuses on the overall system performance assessment during grid connected and islanded modes. For Photovoltaic system, its DC-AC side simulation results with vector-current control technique are provided and comparison study is conducted of controlling the active and reactive powers independently. Islanding detection logic, along with its controls, are observed to follow the microgrid behaviour at different loads. Harmonic analysis is performed to examine the THD at PV, battery, 600 V PCC and 13.8 kV PCC buses.

4.2 Photovoltaic system

For the Photovoltaic system, its steady-state operational performance is investigated. The Photovoltaic system comprises of an incremental conductance (IC) based MPPT algorithm.

4.2.1 Photovoltaic output

Simulation results show the operation of Photovoltaic system at the output of PV. In this case, the input variables to the PV cells are Irradiance and Temperature. Step changes are applied to these inputs to study the dynamic behaviour of the units.

In Figure 23a, Temperature is initialy at $25^{o}\ C$ and is step increased to $40^{o}\ C$ at 1.8 s. Temperature remains at $40^{o}\ C$ for 400 ms, and at 2.2 s it is suddenly stepped down to its normal value of $25^{o}\ C$. In Figure 23b, Irradiance is initialy at 1000 W/m^2 and is suddenly stepped down to 800 W/m^2 at 1 s. Irradiance remains at 800 W/m^2 for 300 ms, and is then gradually increased (ramped up) at 1.3 s back to its initial value.

In Figure 23c and 23d, PV-Voltage and PV-Current are roughly around 135 V and 400 A respectively. The impact of variations in Temperature and Irradiance on the PV-Voltage and PV-Current can be observed. Multiplication of both voltage and current is Power, and is shown in Figure 23e. The fluctuations in Power are tracked with respect to the input changes.

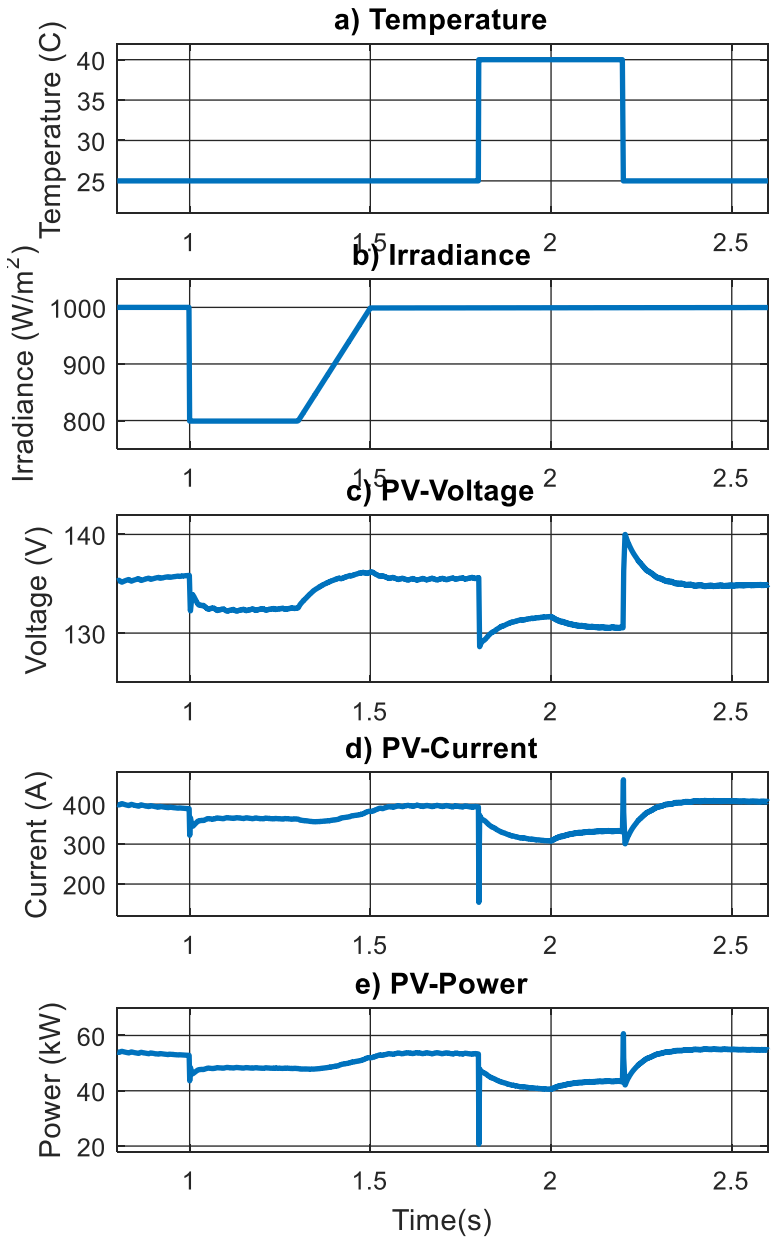

Figure 23: PV Output simulation results

4.2.2 Boost converter

Simulation results represent the operation of the boost converter. Figures 24a, 24b and 24c are respecitively the output voltage, current and power of the boost converter. The boost converter boost the input voltage from 135 V to 400 V and reduces the output curent of the boost converter to 145 A. The output power is reduced from 50 kW to 45 kW because of the converter action. In Figure 24d, Duty Cycle is maintained at 70%

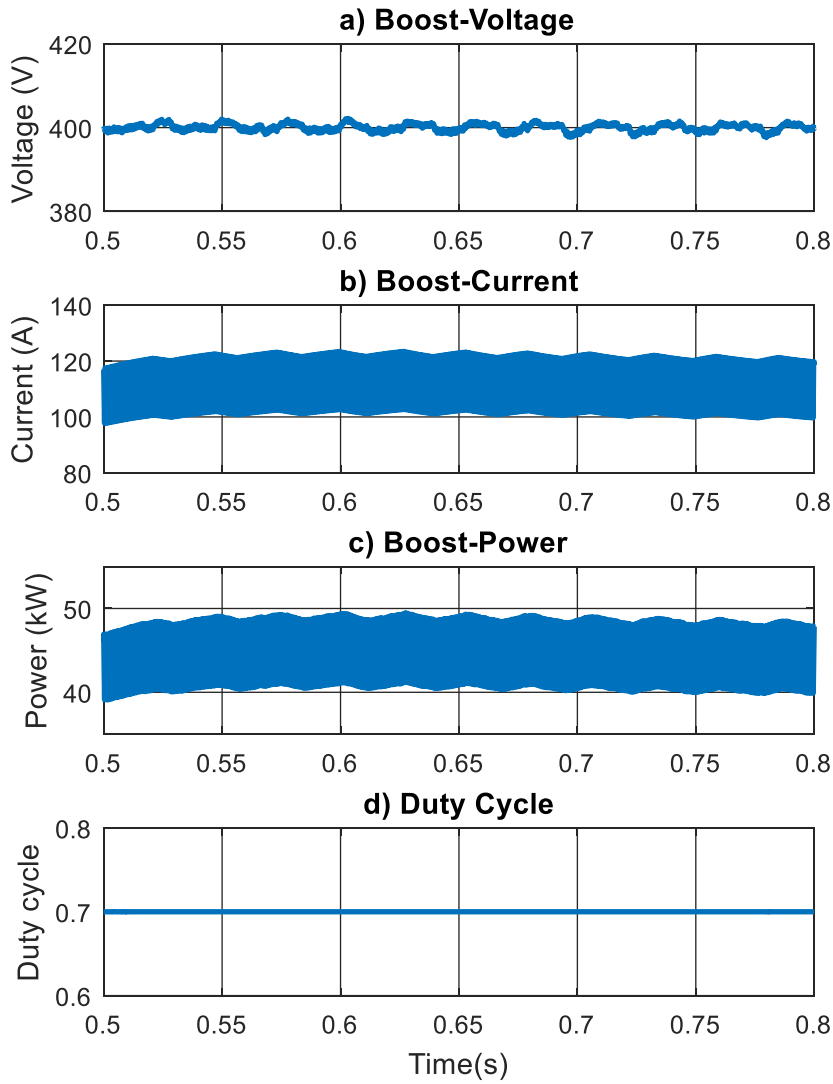

Figure 24: Boost converter simulation results

4.2.3 Three-phase Voltage output waveforms

In this simulation, the DC output voltage from the boost converter is converted to three-phase AC voltage. Figures 25a, 25b and 25c are respectively the output voltage at the converter side, filter and at 600 V PCC. It can be observed in Figures 25a and 25b, that the three-phase, 3-level pulses are transformed to three-phase sine wavefroms by using AC filters. In Figure 25c, the PV voltage is stepped from 320 V to 600 V. THD of these voltage waveforms are shown in section 4.5.2.

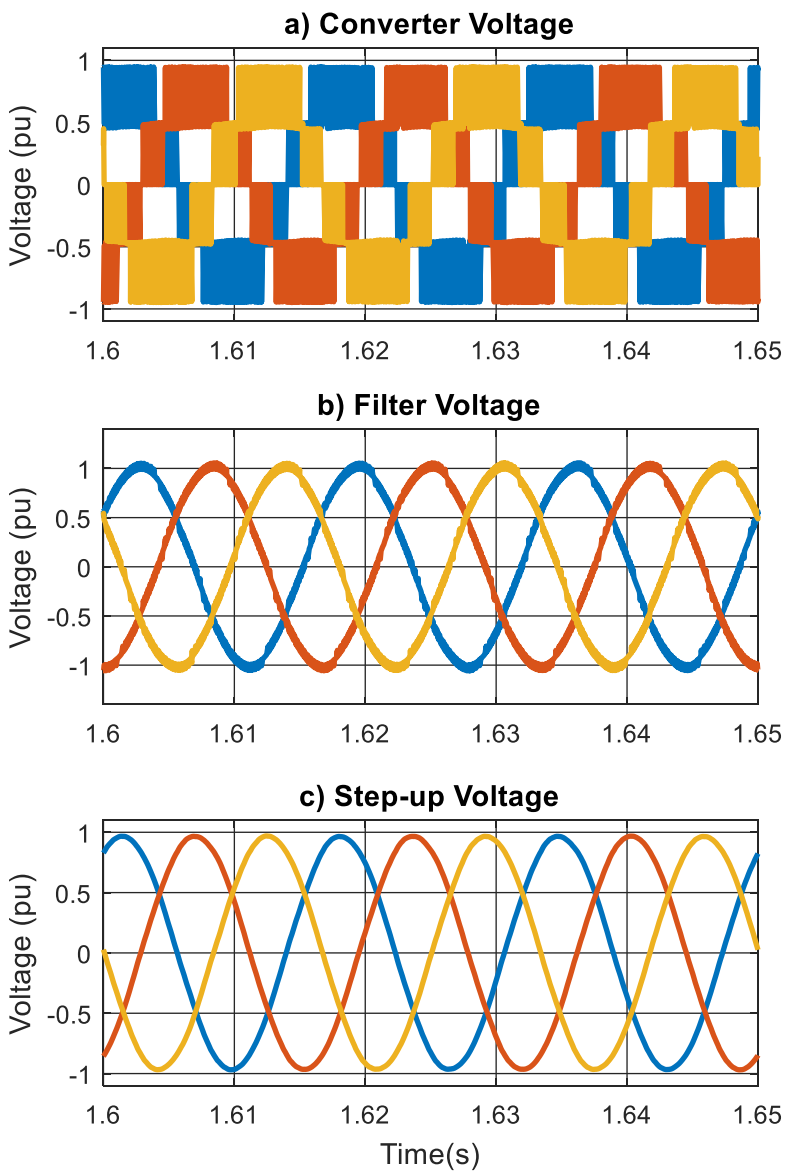

Figure 25: AC Voltage waveforms for PV

4.2.4 Three-phase Current waveforms

In this simulation, the DC output current from the boost converter is converted to three-phase AC current. Figures 26a, 26b and 26c are respectively the output current at the converter side, filter and at 600 V PCC.

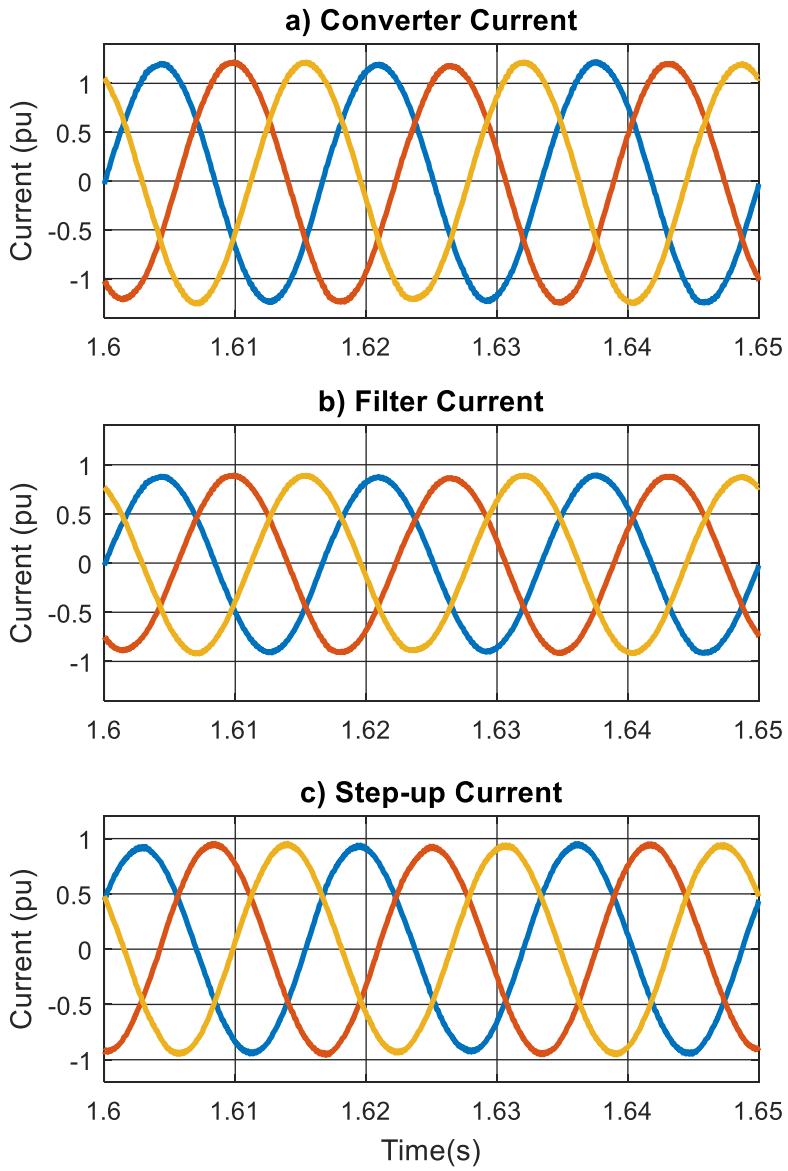

Figure 26: AC Current waveforms for PV

4.3 Battery Simulation Results

For the Battery system, its steady-state operational performance is investigated here. The Battery system comprises of vector-current control. Actisve and reactive powers can flow in both directions, depending on the reference values as the system modeled here is acting as a bi-directional converter.

4.3.1 Three-phase Voltage waveforms

In this simulation, the DC output voltage from battery is converted to three-phase AC voltage. Figures 27a, 27b and 27c are respectively the output voltage at the converter side, filter and at 600 V PCC. It can be observed in Figures 27a and 27b, that the three-phase, 3-level pulses are transformed to three-phase sine wavefrom by using AC filters. In Figure 27c, battery voltage is stepped up from 375 to 600 V. THD of the following voltage wavefroms are shown in section 4.5.1.

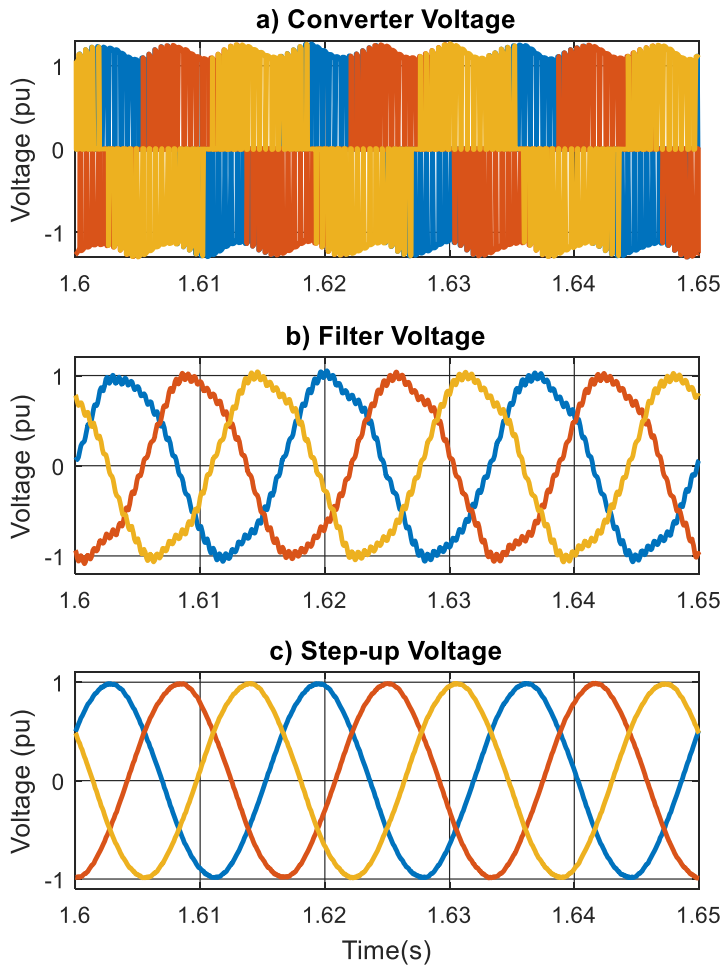

Figure 27: AC Voltage waveforms for Battery

4.3.2 Three-phase Current waveforms

In this simulation, the DC output current from the battery is converted to three-phase AC current. Figures 28a, 28b and 28c are respectively the output current at the converter side, filter and at 600 V PCC. It can be observed in Figure 28a, that the harmonic content in the

converter-side current wavefrom is reduced using AC filters and shown in Figure 28b. In Figure 28c is shown the measured current at 600 V PCC.

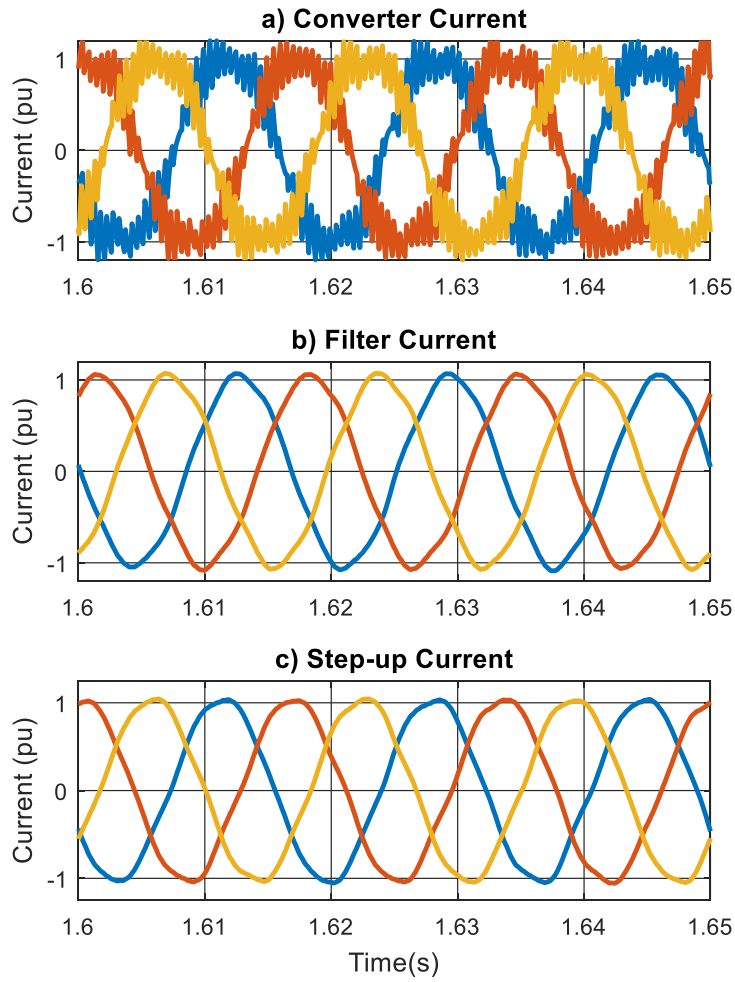

Figure 28: AC Current waveforms for Battery

4.3.3 Active Power Control (Inverter mode operation)

In this case study, the bi-directional converter is operating in inverter mode. The reference values of the Active power controller are changed to control the amount of power to be delivered by the battery to the load. It can be observed in Figures 29a, 29b and 29c that the system responds in controlling the power with respect to the reference values of -1 pu, -0.5 pu and -0.1 pu. In Figure 29a, there is an undershoot of -0.25 pu and it takes 0.7 s for the power to reach its steady state. Similarly, in Figures 29b and 29c, there is an undershoot of -0.22 pu and -0.19 pu respectively. It can also be observed that the controller reaches its

steady state quickly when the reference value is reduced. It takes around 0.5 s and 0.3 s respectively for the power to reach its steady state in Figures 29b and 29c.

It is also observed that at 1.5 s, the steady state power is changed due to a small step of -0.1 pu to observe the dynamic behaviour of the system. This step is not observed in Figure 29a.

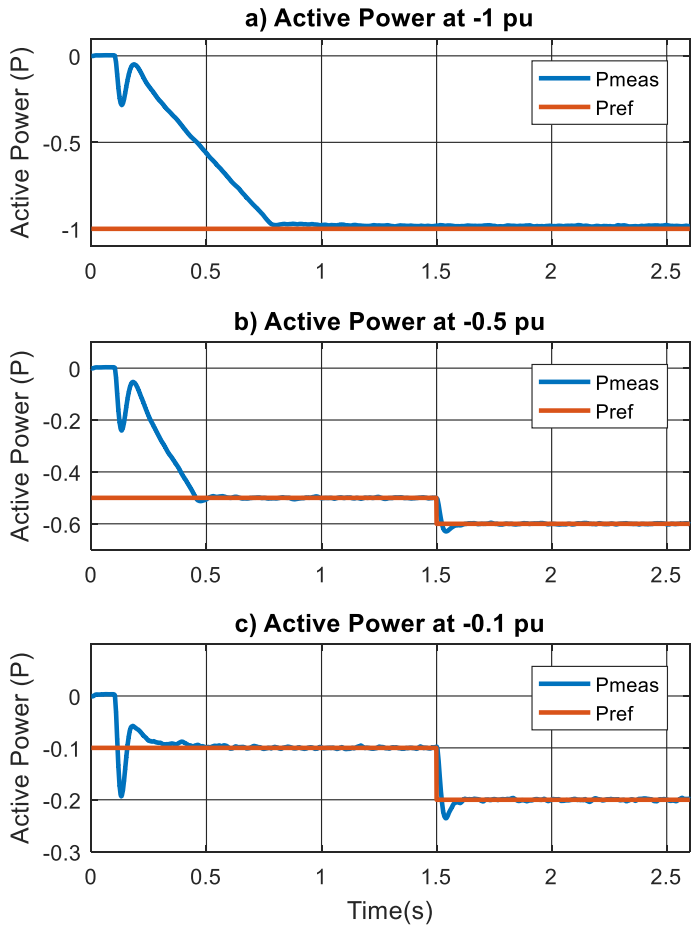

Figure 29: Active Power control (Inverter mode)

4.3.4 Reactive Power Control (Inverter mode operation)

In this case study, the bi-directional converter is operating in the inverter mode. The reference value of Reactive power controller is similarly changed as mentioned previously. It can be observed in Figures 30a, 30b and 30c that the system responds in controlling the reactive power with respect to the reference values of -0.5 pu, -0.3 pu and -0.1 pu. In Figure 30a, there is an undershoot of -1 pu, whereas for Figures 30b and 30c there is an undershoot of -0.8 pu and -0.57 pu respectively. It can also be observed that the settling time for all

three controllers are the same for it to reach its steady state values. At 1.5 s, a small transient is observed due to a step in the active power, whereas for Figure 30a, the step is not observed due to the controller limits of -0.5 pu. The small dynamic interaction is observed as there is not 100% decoupling between the power and reactive power controllers, as anticipated.

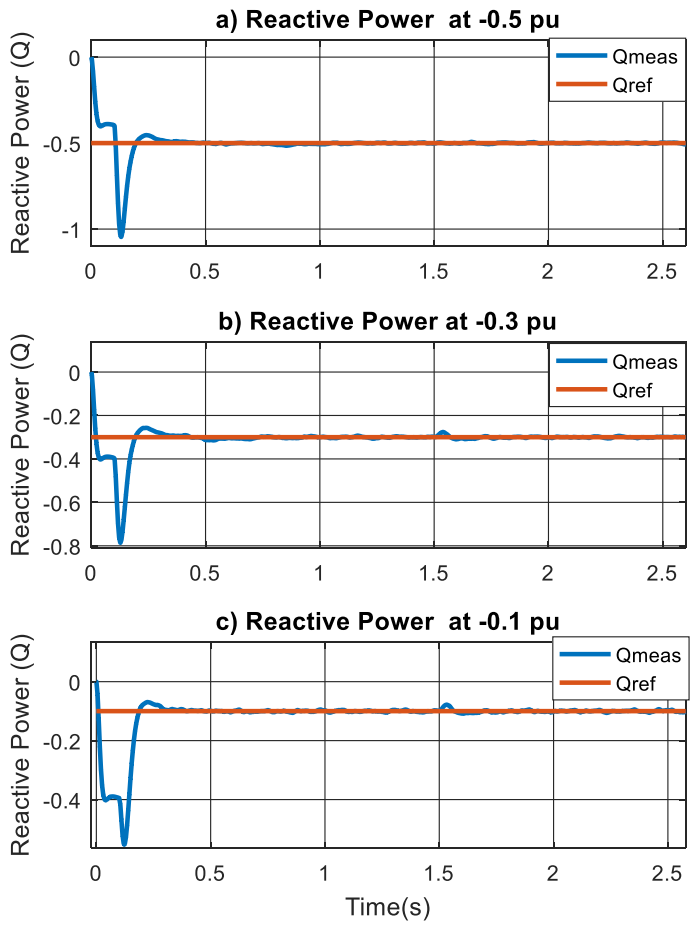

Figure 30: Reactive Power control (Inverter mode)

4.3.5 Active Power Control (Rectifier mode)

In this case study, the bi-directional converter is operating in rectifier mode. The reference values of Active power controller are changed to control the amount to power to be delivered to the battery for charging. It can be observed in Figures 31a, 31b and 31c that the system responds in controlling the power with respect to the reference values of 1 pu, 0.5 pu and 0.1 pu. In Figures 31a and 31b, a very small undershoot of -0.02 pu and -0.03 pu respectively is observed, whereas for Figure 30c there is an undershoot of -0.1 pu. It

can also be observed that the controller reaches its steady state value quickly as the reference value is reduced. It takes around 0.7 s for Figure 31a, whereas 0.5 s and 0.3 s for Figures 31b and 31c.

It is also observed that at 1.5 s, the steady state power is step changed. As explained in previous cases, this is due to a small step of -0.1 pu which is implemented to observe the dynamic behaviour of the system.

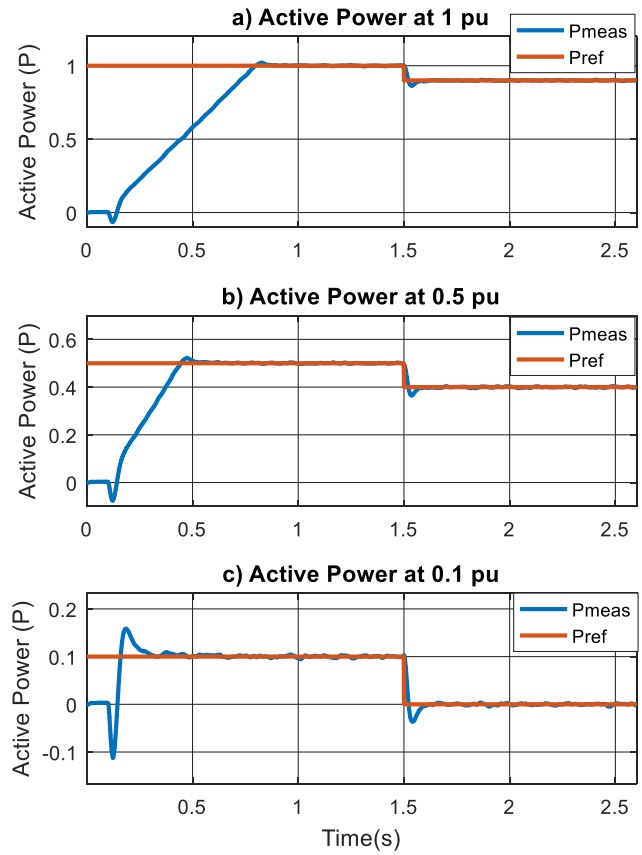

Figure 31: Active Power control (Rectifier mode)

4.3.6 Reactive Power Control (Rectifier mode operation)

In this case study, the bi-directional converter is operating in the rectifier mode. The reference value of Reactive power controller is similarly changed as mentioned previously. It can be observed in Figures 32a, 32b and 32c that the system responds in controlling the reactive power with respect to the reference values of 0.5 pu, 0.3 pu and 0.1 pu. It can be observed that the settling time for all three controllers are the same for it to reach its steady state values. At 1.5 s, a small transient is observed due to a step in the active power.

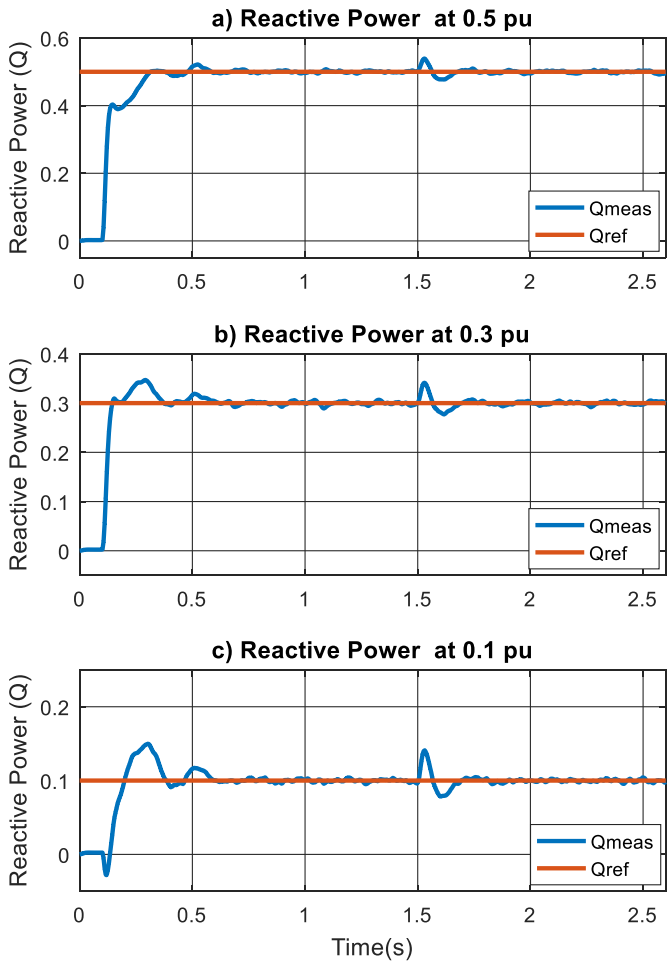

Figure 32: Reactive Power control (Rectifier mode)

4.3.7 Active Power Control at different PI parameters

It is also observed that at 1 s, a small step has been introduced to the system to check the robustness of the controllers with different Kp and Ki values. It is clear that, the ones used in the simulation in the thesis have a good enough (maybe not the best) performance when it comes to transients and tracking the reference value (Figure 33a). By contrast, with less optimal parameters, the response of the controller becomes less ideal especially in transient behavior (Figures 33b and 33c). This shows that the controller parameters implemented in this thesis are adequate to provide a smooth transition in the output voltage and power, without interfering with the study of the effect of the microgrid on the PCC and the introduced islanded technique.

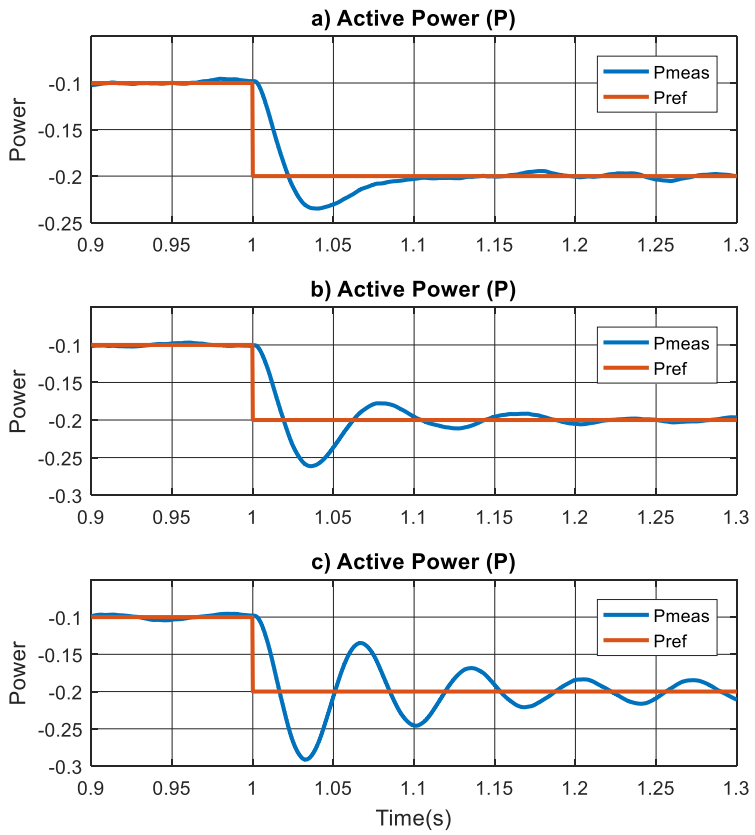

Figure 33: Active Power control at different PI parameters

4.4 Islanding detection and control

In this case study, the microgrid system and its steady-state operational performance is investigated. The microgrid system is operating in stand-alone mode, i.e. the grid is disconnected. To determine when the microgrid's mode of operation is to be changed is the responsibility of the UOV/UOF passive islanding detection scheme. Once the detection logic is triggered, control mode is then switched from P-Q control mode to Voltage-Frequency (V-F) control mode.

4.4.1 Islanding

To initiate the islanded mode operation, first a 3-phase fault is applied on the 600 V PCC. The passive islanding scheme [13] then acts on the UOV and UOF logic signals and triggers the circuit breakers to disconnect the utility grid and the 2 MVA load. Control mode of operation is then changed from P-Q to V/F control mode.

Figure 34 depicts the case of the microgrid system being islanded following a close 6-cycle, 3-phase fault on the PCC at 1.0 s. Figure 34a, shows the rms voltage measured at the 600 V PCC bus and the under/over voltage (UOV) logic signal in blue. Initially, the voltage measured at 600 V PCC is 1 pu. It can be seen that the resultant transient changes in voltage causes switching over of the microgrid operation to islanded mode. Transient changes in voltage are then sensed by the under/over voltage logic, causing the breaker signal shown in Figure 34c to trip. The trip of the breaker signal happens at 1.17 s which disconnects the utility grid and a microgrid is formed. It then changes the control mode of operation from P-Q to V/F mode. This V/F mode is initialized at 1.37 s. The measured voltage is at 1.3 pu until 2 s, but it is stabilized to 1 pu at 2.5 s. Figure 34b depicts the frequency and the UOF logic signals. It can be observed that frequency is at 60 Hz before the 3-phase fault is applied. After 100 ms fault, it can be seen that there is a transient overshoot in frequency to 61 Hz, as the utility grid is isolated. When V/F mode is initialized at 1.37 s, it can be seen that the frequency comes back to steady state at 1.6 s

Figure 34c shows the CB2 and CB3 Breakers (Figure #4) and V/F logic signals, which indicates the passive islanding detection. The CB2 is opened at 1.17 s whereas Breaker CB3 is opened at 1.32 s. Mode of operation to V/F is initialized at 1.37 s. (Note that the corresponding signal for re-connection of the islanded grid is not shown here.)

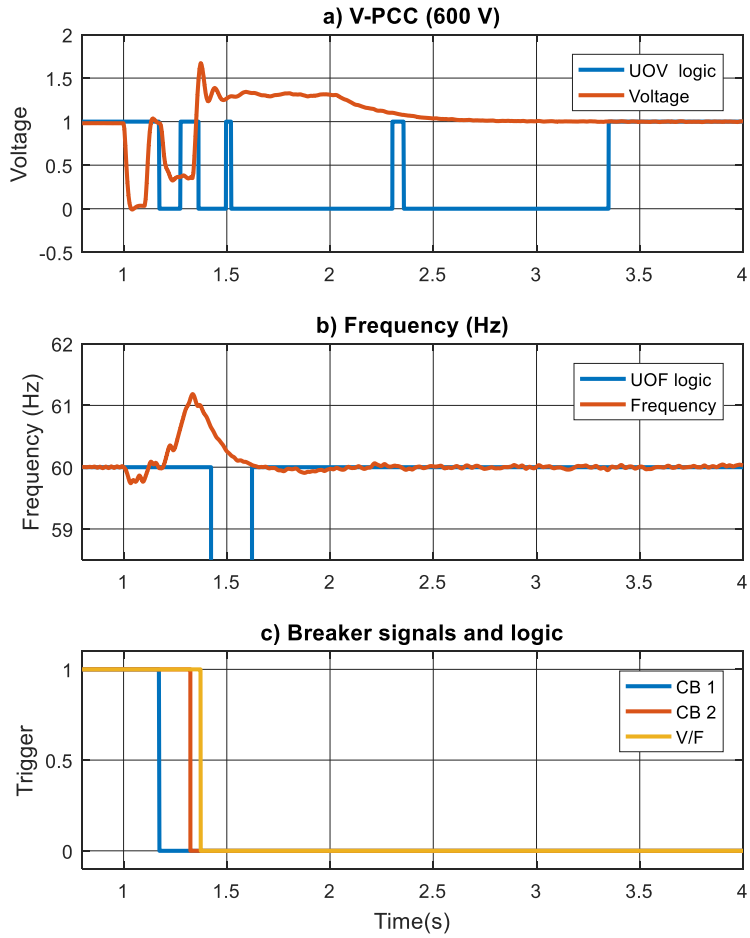

Figure 34: Islanding mode simulation results

4.4.2 Islanding with different loads

In this parametric study, the magnitude of the critical load is varied from 50, 200, 350 to 500 kVA to investigate the impact of the size of the load on the PCC 600 V voltage (Figure 35a) and frequency (Figure 35b). Table 8 summarizes the comparative results on the voltage as the critical load is varied. Table 9 shows the comparative results on the frequency as the critical load is varied. The damping effect of the variable loads is clearly visible on the undershoot, overshoot and settling times.

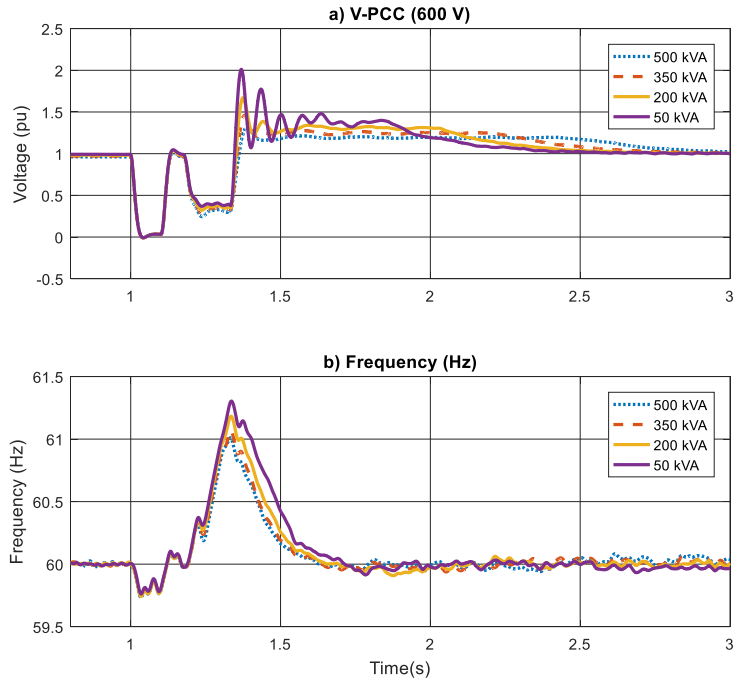

Figure 35: Islanding with different loads

Table 8 - Different load test (Voltage)

Load (kVA)	Undershoot (pu)	Overshoot (pu)	Settling time (s)
50	0.37	2.00	1.30
200	0.31	0.68	1.40
350	0.29	0.45	1.50
500	0.24	0.31	1.80

Table 9 - Different load test (Frequency)

Load (kVA)	Undershoot (Hz)	Overshoot (Hz)	Settling time (s)
50	59.76	61.30	0.39
200	59.75	61.18	0.37
350	59.74	61.06	0.32
500	59.73	61.01	0.30

4.4.3 System behaviour without islanding

In this case, a high impedance 3-phase fault is applied on the 600 V PCC bus. The magnitude of the fault impedance is such that the measured voltage and frequency do not exceed the limits of either UOV or UOF logic circuits; hence the circuit breaker is not tripped for islanding. Control mode of operation is also not switched from PQ to V/F mode.

Figures 36a and 36b show the system voltage and frequency respectively (with lower and upper limits indicated in dotted lines) following a remote fault (fault impedance is 20% or greater, than the base impedance) on this system; in this case again, the remote fault magnitude is such that it does not cause islanding mode of operation as the UOV and UOF logic signals are not impacted enough, and the system is able to ride through the fault.

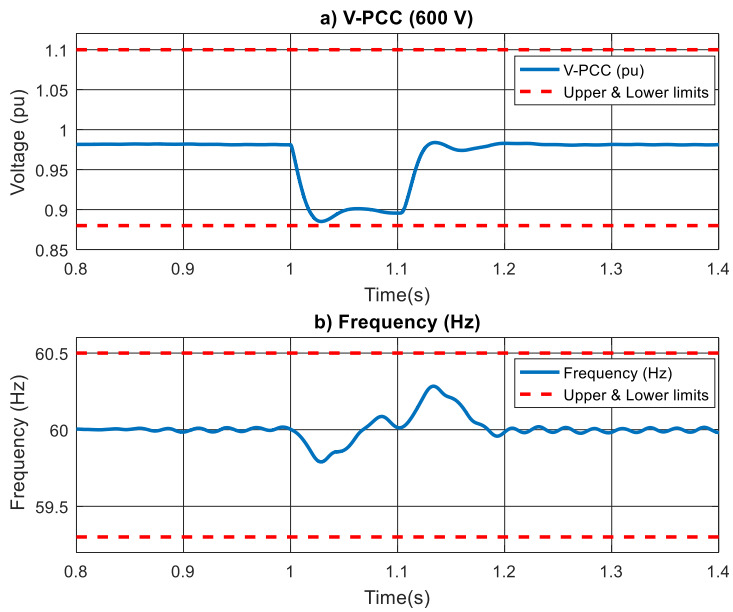

Figure 36: 20% base impedance fault

4.4.4 Islanding detection logic

Figure 37 shows the outputs of the UOV islanding detection logic in more detail for the corresponding case shown in Figure 37. Figure 37e shows the output of the rms voltage less than 0.5 pu after a time delay of 0.16 s. Figure 37d shows the output of the rms voltage less than 0.88 pu after a time delay of 2 s. Figure 37c shows the output of the rms voltage less than 1.1 pu after a time delay of 1 s. Figure 37b shows the output of the rms voltage less than 1.2 pu after a time delay of 1 s. Figure 37a shows the output of the UOV logic detection circuit. These time delays are as recommended in IEEE Standard 1547, but need to be coordinated for the particular microgrid system in use.

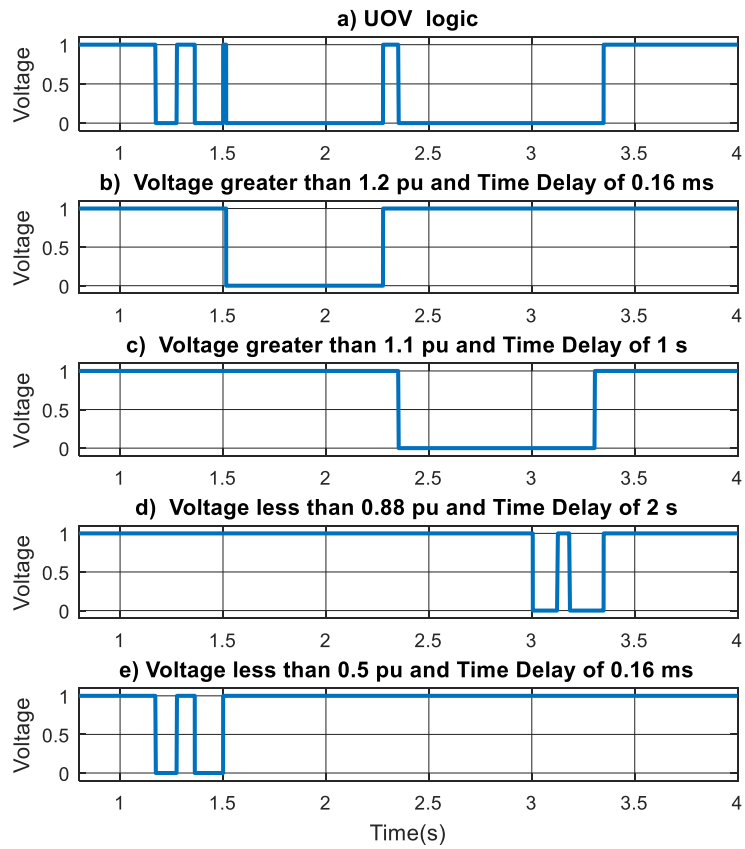

Figure 37: UOV logic sequence

4.5 Harmonic Analysis

Harmonic Analysis tool is used to analysis Total Harmonic Distortion (THD) as poor power quality will significantly degrade overall efficiency of the power system. In the proposed model discussed in section 2.2, the microgrid comprised of Photovoltaic and Battery storage is connected to utility grid via a power electronics interface. These power electronics devices are potential harmonic sources. Harmonics in the voltage and/or current waveforms are reduced by having filters to improve power factor and efficiency.

THD is defined as the ratio of number of harmonics at fundamental frequency, which is mathematically defined as:

$$THD = \frac{\sqrt{\sum_{n=2}^{\infty} H_n^2}}{H_1} \tag{4.1}$$

where H_n is the magnitude of harmonic components, n is an integer and H_1 is the magnitude of the fundamental component.

4.5.1 Harmonic analysis at Battery

Figure 38 shows the harmonic content at the filter, whereas Figure 39 shows the harmonic content after the converter side. It can be observed that the THD content is significantly reduced as the filters are designed accordingly. It can also be observed at the converter side that the 3rd and 5th harmonics are 4.19% and 1.57% of fundamental frequency respectively, whereas the 3rd and 5th harmonics are 6.26% and 2.11% of fundamental frequency respectively after the filter.

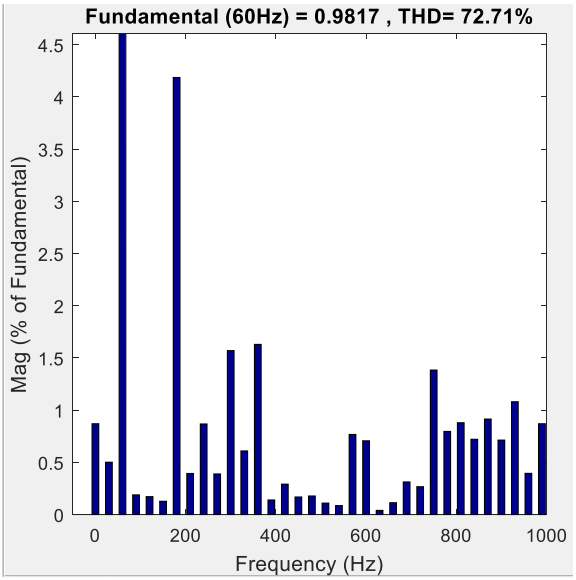

Figure 38: Harmonics at converter side for Battery

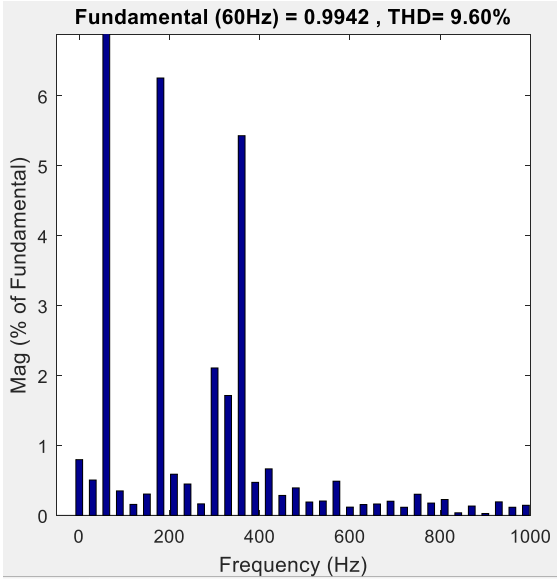

Figure 39: Harmonics at filter side for Battery

4.5.2 Harmonic analysis at PV

Figure 40 shows the harmonic content at converter side, whereas Figure 41 shows the harmonic content after the filter. It can be observed that THD content is slightly reduced as the filters are not fully optimised to decrease harmonic content. It can also be observed at converter side that the 3rd and 5th harmonics are 0.21% and 0.15 % of fundamental frequency respectively, whereas the 3rd and 5th harmonics are 0.04% and 0.02% of fundamental frequency respectively after the filter.

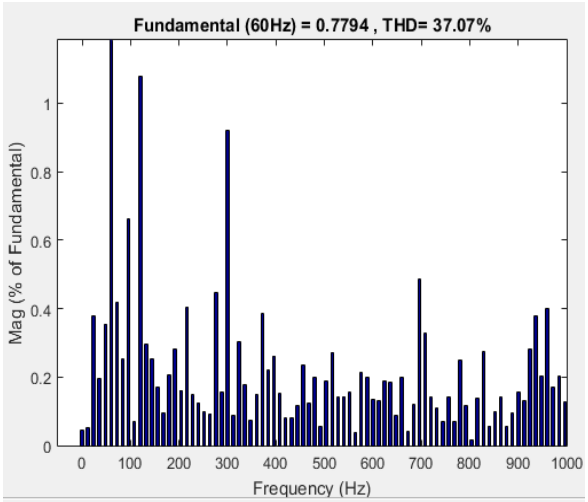

Figure 40: Harmonics at converter side for PV

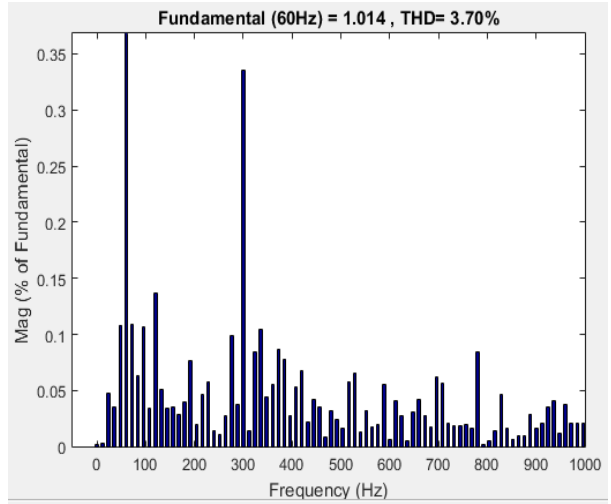

Figure 41: Harmonics at filter side for PV

4.5.3 Harmonic analysis at HV and LV PCC

Figure 42 shows the harmonic content at 600 V PCC, whereas Figure 43 shows the harmonic content at 13.8 kV PCC bus. It can be observed that THD content is significantly reduced at 13.8 kV PCC compared to the 600 V PCC bus. It can also be observed at grid side that the 3rd and 5th harmonics are 0.04% and 0.66% of fundamental frequency respectively, whereas the 3rd and 5th harmonics are 0.01% and 0.13% of fundamental frequency respectively at the microgrid.

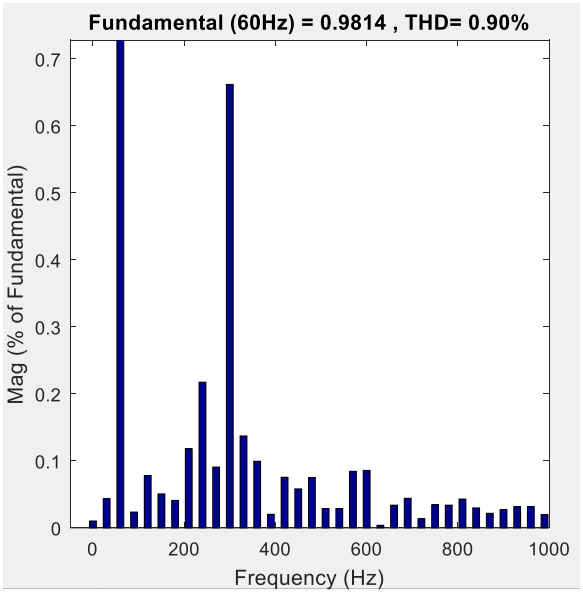

Figure 42: Harmonics at 600 V PCC

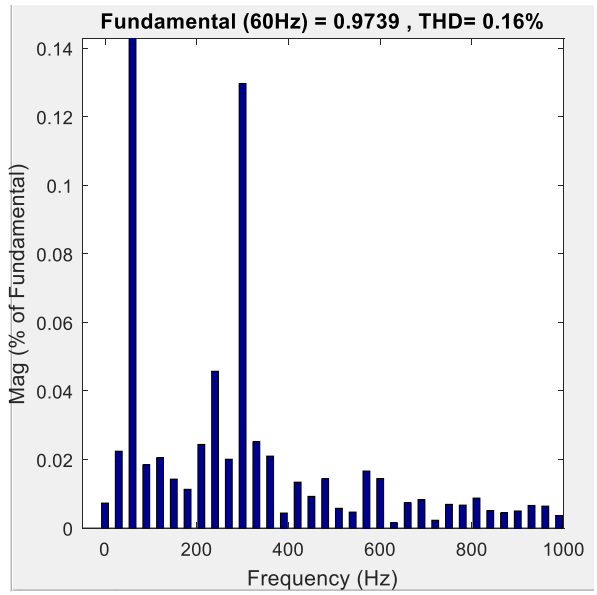

Figure 43: Harmonics at 13.8 kV PCC

Chapter 5: Communication for microgrid

Traditional power grids are now evolving to smart grids. Smart grid uses two-way communication networks to support intelligent mechanisms for predicting failures and monitoring the condition of the network. Therefore, communication plays a vital role to transform the smart grids into microgrids. An important concern in microgrids is the security, load sharing and the variability of DG's. which affects power flow management and voltage control. Therefore, effective communication infrastructure - combined with advanced control techniques – is needed to maintain the stability and safe operation during islanding of the microgrid [48].

This chapter focuses on the basic communication network present in a microgrid. As shown in Figure 44, within a microgrid there are local controllers and a master controller. The task of the local controller is to ensure the DG's are operating accordingly to a set value defined by the master controller. Along with it, a local controller monitors the DG ratings and sends in back to the master controller. The master controller is an Energy Management System (EMS), which optimizes overall performance and operation of the microgrid.

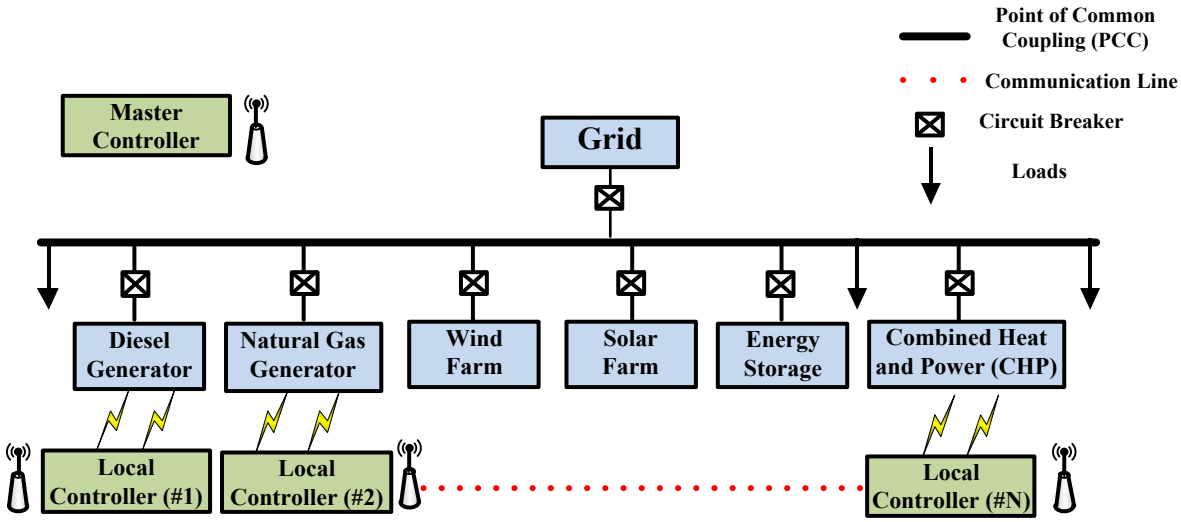

Figure 44: Communication network for microgrid

The communication network can be seen as the spinal cord of a MG. They connect the power generating sources, transmission, distribution and consumption systems to the management block in order to evaluate the real-time data that reflects the stability of the entire grid [49]. Information is exchanged bi-directionally among operators, energy

generating sources and consumers. Micro-grid communication networks can be divided into the following categories [48]:

1. Home Area Networks (HANs): Provides low bandwidth, two-way communication between the home appliances and equipment such as smart meters to collect the real-time data
2. Field Area Networks (FANs): Provides low bandwidth, two-way communication between the microgrid control station and customer premises
3. Wide Area Networks (WANs): Provides high bandwidth, two-way communication between the microgrid and utility grid.

To establish a reliable, secure and effective two-way communication for the information exchange, a communication subsystem in a microgrid must at least consist of the following basic requirements:

- Should support the Quality of Service (QoS) of data. This is because the critical data must be delivered promptly
- Must be highly reliable since large number of devices will be connected and will be communicating with different devices
- Must have a high coverage, so it can respond to any event in the microgrid
- Must guarantee security and privacy

Communication networks can be implemented wired or wirelessly. Wireless networks offer significant benefits over wired networks such as rapid deployment, low installation cost, mobility, etc. This thesis focuses on wireless communication; therefore, it will be comparing existing technology's several parameters such as security, cost and bandwidth to identify the most suited protocols for wireless communication.

5.1 Microgrid Communication

As mentioned previously, microgrids are part of FAN and WAN networks as microgrids are usually installed close to consumers. Therefore, a comparison of different protocols is shown in Table 10. It is observed that most suitable wireless technology for microgrid communication is either ZIGBEE, Wi-Fi, NRF24L01, Bluetooth and LoRa. There are other

wireless technologies such as Z-wave, GPRS and Wi-MAX but considering the cost and range, NRF24L01 and LoRa appear to be the most promising technologies [50].

Table 10 - Comparison of different protocols

Protocol	**Data rate**	**Coverage**
Bluetooth	721 kbps	10 – 30 m
Wi-Fi	1 – 54 Mbps	100 m
ZIGBEE	250 kbps	100 m
NRF24L01	250 kbps, 1 Mbps and 2 Mbps	Up to 1 km
LoRa	50 kbps	Up to 15 km

5.1.1 Microgrid communication network design

The following section compares the mentioned protocols based on various parameters to determine best suitable technology for microgrid communication. The protocols will be compared based on topology, security, bandwidth available, transmission time and installation costs.

5.1.1.1 Topology

Placement of nodes in a microgrid is random and unique to each microgrid. One cannot predict where and how many loads and generators are going to be present in a particular microgrid. A wireless network can either be implemented in a centralized or decentralized topology to provide flexible flow of information to achieve two-way communication for an efficient, secure and reliable power delivery and use.

A centralized configuration (Figure 45), requires a two-way communication channel between the Primary Control (Local controllers) and Secondary Control (Master controller) for the exchange of information. This configuration is called a Star-connection topology and a master/slave technique is established. The communication channels can be either wired or wireless depending on its requirements.

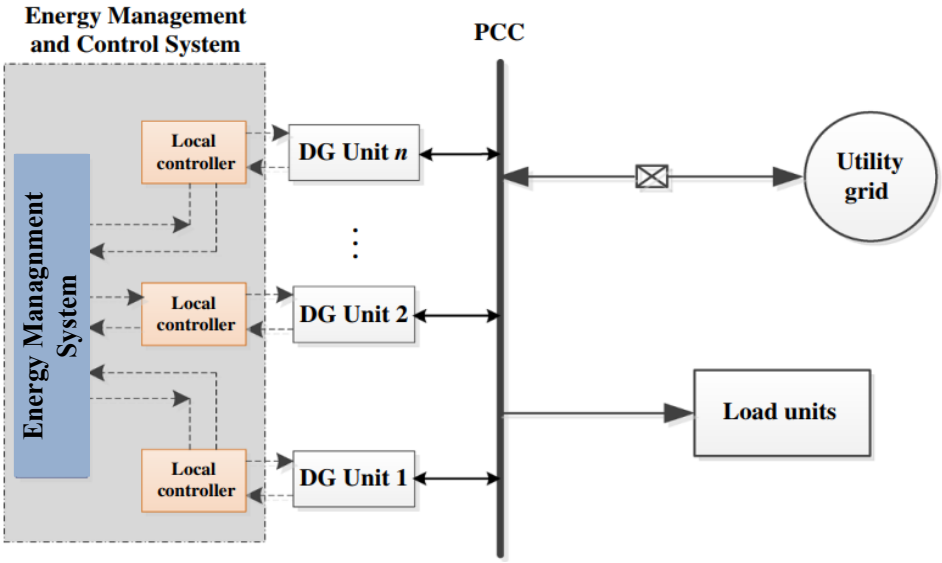

Figure 45: Centralized configuration [5]

A decentralized configuration (Figure 46), illustrates a two-way communication channel between the local controllers for the exchange of information. This configuration is called a peer-to-peer (P2P) communication topology and is established within the Primary Control layer. The EMS is implemented locally in each of its Local controllers connected to either DGs or the loads within the microgrid to allow the interaction of each unit to enable a decision-making process to optimally solve the energy management problem while providing flexibility within the microgrid to provide autonomy for all DG's and loads.

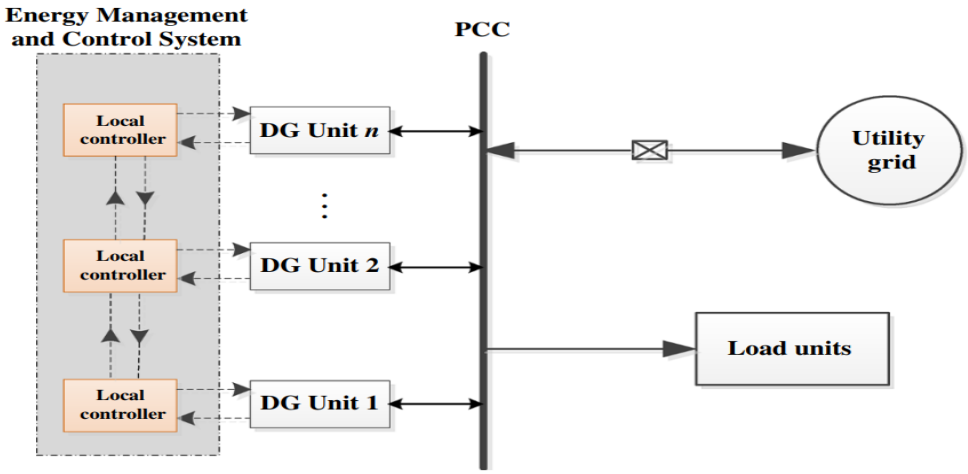

Figure 46: Decentralized configuration [5]

5.1.1.2 Bandwidth

Communication within the microgrid is not bandwidth intensive. The messages exchanged between the master controller and local controllers are mostly small message signals, which do not require a very high-speed link. According to a survey on smart grid communication requirements [51], a bandwidth of 1Mb should be enough for communication in a microgrid. Table 11 enlist the required bandwidth for various microgrid applications, which needs to be exchanged between the local controllers and master controller.

5.1.1.3 Security

Security is a major concern for the safe operation of microgrid, as the sensitive information exchanged needs be communicated through a secured communication link. Therefore, the technology used should have encryption to ensure confidentiality and integrity of the data.

5.1.1.4 Transmission delay

Extensive research has been done on the messages that need to be exchanged between Master controller and Local controller. A survey on smart grid communication requirements have looked into the latencies that are acceptable for various types of applications within the microgrid [51]. Table 11 enlist the required latency for various microgrid applications, which needs to be exchanged between the local controllers and master controller.

Table 11 - Requirements of microgrid applications

Smart Grid Application	**Bandwidth**	**Latency**
Substation Automation	9.6 – 56 kbps	15 – 200 ms
WASA	600 – 1500 kbps	15 – 200 ms
Outage Management	56 kbps	2000 ms
Distribution Automation	9.6 – 100 kbps	100 ms – 2 sec
Distributed Energy Resources	9.6 – 56 kbps	100 ms – 2 sec
Smart Meter Reading	10- 100 kbps/ meter	2000 ms
Demand Response	10 – 100 kbps	500 ms – min
Demand Side Management	10 – 100 kbps	500 ms – min
Assets Management	56 kbps	2000 ms

5.3.1.5 Cost

Regardless of various technical requirements for microgrid, it is necessary and useful to have a low cost for the operation of microgrid.

5.1.2 Wireless technologies for microgrid communication [36]

5.1.2.1 Bluetooth (IEEE 802.15.1)

Bluetooth is a radio based wireless technology which is low cost, small range and is mainly applied in HAN and FAN. This technology supports data rate up to 721 kbps, and maximum possible range of 10-30 m. Bluetooth network can either be implemented either in piconet and scatternet (centralized and decentralized topology). Bluetooth router has an inbuilt 16-bit CRC encryption and it usually cost around $80-$100.

5.1.2.2 ZIGBEE (IEEE 802.15.4)

ZIGBEE is radio based wireless technology which is low cost, medium range and is mainly applied in HAN and FAN. This technology supports data rate up to 250 kbps, and maximum possible range of 100 m. ZIGBEE network provides self-organized, multi-hop communication. This network topology is also similar to Bluetooth, where either centralized or decentralized communication can be implemented. ZIGBEE has an inbuilt 128-bit AES encryption and it usually cost around $50-$100 per device and $250 for a router.

5.1.2.3 Wi-Fi (IEEE 802.11)

Wi-Fi is a widely used network protocol. It is a low cost, medium range technology which is applied in HAN and FAN. It supports data rate up to 54 Mbps, and maximum possible range of 100 m. It is a full meshed network which can easily be modified into a desired star topology. A main disadvantage of deploying this protocol is potential inter-channel interference from other devices using same protocol and channels. Wi-Fi has an inbuilt 32-bit CRC encryption and the router usually cost around $150.

5.1.2.4 Radio Frequency (RF)

A NRF24L01 RF transceiver can be an ideal option when comparing its parameters with other wireless technologies. It cost around $10 which a low-cost transceiver and operates on 2.4 GHz. A common tree topology can be implemented with 6 independent channels. It has data rate of 250 kb/s, 1 and 2 Mb/s. Due to an increase in various technologies such as ZIGBEE and Bluetooth in busy domestic environments, NRF24L01 becomes a robust

wireless link which is immune to interference from other 2.4 GHz technologies. This transceiver can be an idea choice for microgrid applications, but due to its lack of security feature makes it a debatable choice for a user. Although, if a high-level encryption is implemented, it would enhance the device capabilities and be an optimal low-cost wireless technology for microgrid applications. A Norway based energy metering specialist, Landis_Gyr Enermet, has already implemented it for smart utility meters applications [52].

Table 12 summarizes the various technologies mentioned above in terms of different parameters such as range, bandwidth, security and frequency band. This information is useful while simulating the protocols for microgrid.

Table 12 - Microgrid communication protocols

Parameter	**Bluetooth**	**ZIGBEE**	**Wi-Fi**	**NRF24L01**
Frequency Band	2.4 GHz	2.4 GHz	2.4 GHz	2.4 GHz
Range	100 m	10 – 100 m	100 m	600 m
Channels	79	16	14	6
Topology	Tree	Tree	Mesh	Tree
Data Protection	16-bit CRC	16-bit CRC	32-bit CRC	N/A
Data Rate	1 Mb/s	250 kb/s	54 Mb/s	250 kb/s, 1 and 2 Mb/s

This chapter has investigated possible protocols that are suitable for wireless communication within a microgrid by comparing existing technology's several parameters such as security, cost and bandwidth. Next chapter will further investigate the details and operation of NRF24L01 transceiver as it has shown to be a better option when compared with other low-cost devices. A proof of concept case study will later be implemented to analysis various scenarios so that the microgrid would be able to work effectively and communicate its status to the EMS (master controller).

5.2 Wireless Communication NRF24L01 Transceiver

A 2.4 GHz wireless RF transceiver is an integrated radio frequency module which enables a two-way communication. It is a combination of electronic components like filters, self-contained circuits and amplifiers which supports the module to either perform as a Transmitter (TX) or a Receiver (RX). NRF24L01 (Figure 47) is a low-cost module which can transmit data at 250 kbps, 1 and 2 Mbps, allowing an efficient and reliable communication [53].

Figure 47: NRF24L01 transceiver [53]

The ISM radio band of 2.4 GHz employed by the NRF24L01 wireless module resolves the concern of communication between the Master Controller and Local Controller. The module is a single chip transceiver consisting of a transmitter and receiver which simultaneously transmits and receives data, making this a small fashioned, remarkable and effective component for a point-to-point communication. Moreover, the Low Noise Amplifier (LNA) & Power Amplifier (PA) circuit in the module enables an efficient wireless communication to transmit data in a reliable manner.

5.2.1 Functional Block Diagram of NRF24L01

A communication between the Master Controller and Local Controller plays an important role in making the hierarchical control of the Microgrid. Therefore, it is important to know the functionality of NRF24L01 module. It comprises of 14 different functional blocks which is shown below in Figure 48.

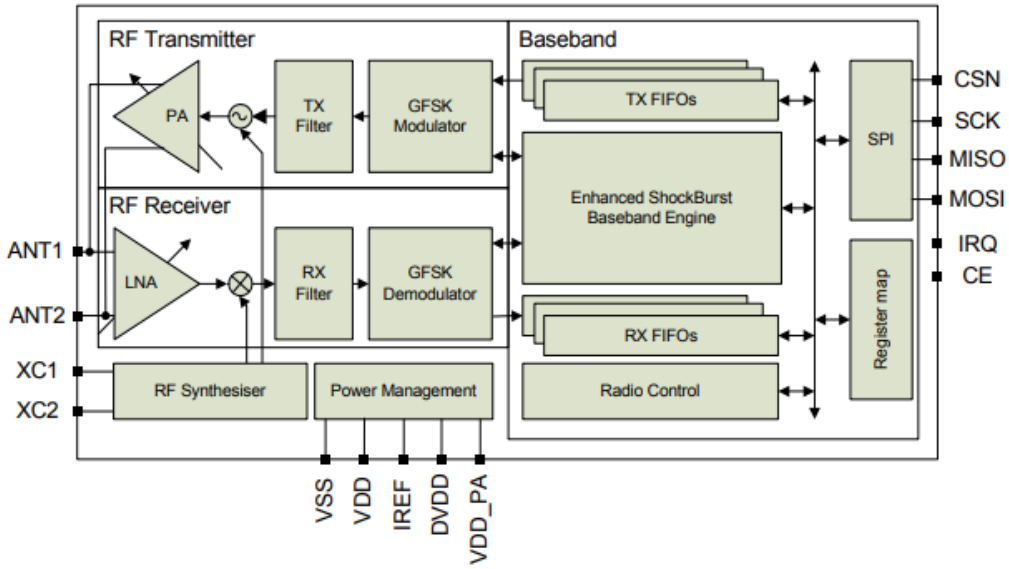

Figure 48: NRF24L01 block diagram [53]

NRF24L01 is divided into 3 parts as observed in the block diagram and shown in Table 13. The functionalities of the 14 sub-blocks, including other electronic components are categorized as:

Table 13 - Expansion of NRF24L01 major three components

RF Transmitter	• PA (Power Amplifier) • GFSK Modulator • TX filter
Baseband	• TX FIFO • Enhanced ShockBurst Baseband Engine • RX FIFO • Radio Control
RF Receiver	• LNA (Low Noise Amplifier) • RX Filter • GFSK Demodulator

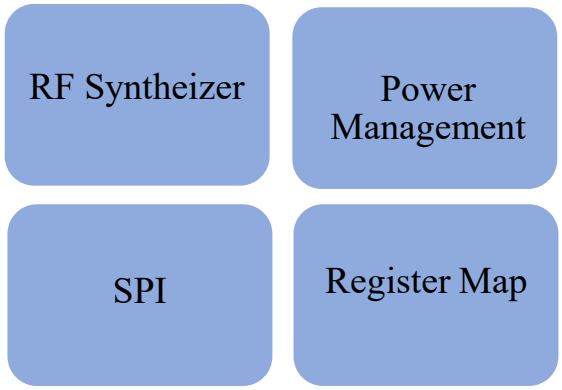

Figure 49: NRF24L01 other four components

5.2.1.1 PA (Power Amplifier)

An RF Power Amplifier converts a frequency signal of a low power to a larger signal with more power. It is a categorized as a type of electronic amplifier which is usually optimized to have good return loss on the output, input, high efficiency, optimum heat dissipation and high output power. Data sheet is provided in the Appendix.

The use of PA in NRF24L01 is to amplify the payload data by the transmitter to transmit through air.

5.2.1.2 Filter

Electronic filters are commonly used to filter out unwanted frequency components from the signal by performing signal processing. NRF24L01 is equipped with digital filters to perform appropriate signal processing.

5.2.1.3 Gaussian Frequency Shift Keying (GFSK) Modulator

GFSK modulator consists of two steps, where the signal goes through Gaussian filter and later gets modulated using FSK. In GFSK, the signal is passed through a Pulse-Shaping Gaussian Low Pass Filter before modulation in order to shape the pulses to give them half-sinusoidal shape so that the phase trajectory of the FSK signal becomes smooth and the instantaneous frequency variations over time are stabilized [54].

And, in FSK the frequency of sinusoidal carrier wave is varied (switched) depending on the digital input signal. The 1's and 0's are transmitted using two different frequencies f_1 and f_2 depending on the data sequence of the binary value.

5.2.1.4 First In, First out (FIFO)

First In, First out (FIFO) is a method for manipulating and organizing data stack or data buffer, where the bottom of the stack (oldest entry) is processed first.

5.2.1.5 LNA (Low Noise Amplifier)

Low Noise Amplifier, an electronic amplifier is used to amplify a weak signal. It is usually located at the receiver to detect low signals, and amplify it and reduce the losses in the feedline [55].

5.2.1.6 RF Synthesiser

A frequency synthesizer is an electronic system which generates frequency of any range from a single fixed time base or oscillator. It can combine frequency mixing, frequency division and frequency multiplication.

RF synthesizers are used to generate frequencies. It is an electronic system that utilizes an oscillator or a single fixed time base for generating frequencies of any range. It can combine frequency mixing, frequency division and frequency multiplication.

5.2.1.7 Serial Peripheral Interface (SPI)

The NRF24L01 module uses Serial Peripheral Interface (SPI) to communicate with the microcontroller. The SPI-bus is a serial communications interface with four wires used by many microprocessors [56]. These wires are:

- SCK – Serial Clock: a 50% duty cycle clock generated by the master
- MOSI – Master Out Slave In: The line for writing data from the master to the slave
- MISO – Master In Slave Out: The line for writing data from the slave to the master
- CSn – Chip Select not: an optional control line, signalling the channel is active. Sometimes called Salve Select (CS)

As shown in Figure 50, the master and slave start communicating when CS is low. Both master and slave operate on same clock, where the slave uses the clock generated by the master to transmit or reveice the data. During the communication, the transmiting device changes the bit on the MISO or MOSI using one edge of the clock, whereas the receiver reads the bit using the other edge of the clock.

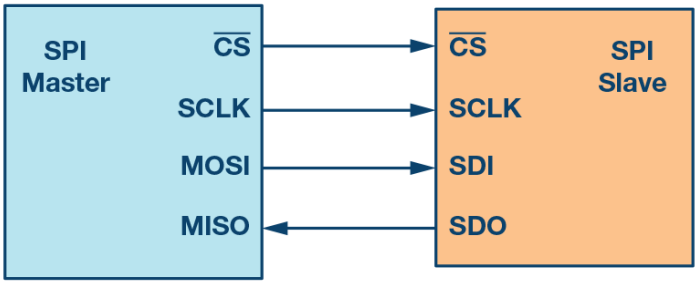

Figure 50: SPI communication between master and slave [56]

5.2.2 Operational Modes of NRF24L01

There are 4 main modes of operation, and the transceiver can be configured in TX, RX, Power Down or Standby mode. All 4 modes are described as [57]:

5.2.2.1 Transmission mode (TX)

When the transceiver is used as a transmitter, the TX mode is active. To enter this mode, the transceiver should have the PRIM_RX bit set low, PWR_UP and CE pin set high. The transceiver stays in this mode until the data to be send is finished transmitting. If CE = 1, the TX FIFO determines next action, and when CE = 0, the transceiver returns to standby-I mode. If TX FIFO is empty the transceiver switches to standby-II mode and when TX FIFO not empty, the transceiver remains in TX mode and keeps transmitting the data.

5.2.2.2 Receiving mode (RX)

When the transceiver is used as a receiver, the RX mode is active. To enter this mode, the transceiver should have the CE pin, PRIM_RX bit and PWR_UP bit set high. In this mode, the signal received from the RF channel is demodulated and constantly sending the received data to the Enhanced Shockburst engine. This Enhanced Shockburst constantly searches if a valid packet is received. Whenever it is received, the data of the packet is sent to the RX FIFOs. If the FIFO is already full, the received packet will be discarded.

5.2.2.3 Power Down Mode

In this mode of operation, the transceiver is deactivated by allowing minimal current consumption. The SPI is set to active and all the values of register available are maintained, allowing the configuration to change and the downloading/uploading of data registers.

5.2.2.4 Standby Mode

5.2.2.4.1 Standby-I mode:

The transceiver enters in standby-I mode when the PWR_UP bit in the CONFIG register to 1. This mode allows to maintain short start up times by minimizing the average current consumption. Only a part of the crystal oscillator is active. Whenever the CE is set to either high, it changes to active mode and when CE is low, the transceiver switches to standby-I mode from both RX and TX modes.

5.2.2.4.2 Standby-II mode:

The transceiver enters in standby-II mode, when the CE is set to high and with an empty TX FIFO. Current consumption is more when compared to standby-I mode, and extra clock buffers are active. The SPI is activated in both standby I and standby-II modes, and all the values of register available are maintained.

5.2.3 Details of NRF24L01 Wireless Module

NRF24L01 is designed to be operated at world-wide 2.400 – 2.4835 GHz ISM frequency band. It is embedded with Enhanced ShockBurst (baseband protocol engine) which makes it an ideal choice for low power applications. The transceiver is configurable through Serial Peripheral Interface (SPI) to communicate with the microcontroller to transmit data. All modes of operation are controlled by the register map, which contains all the registers to be configured, which is accessible through the SPI [57].

Communication by the transceiver is established by the Enhanced ShockBurst feature, which communicates by sending packets and supports numerous modes of operation from advance to manual protocol operation. A smooth flow of data is responsible by the FIFO between the microcontroller and transceiver. The transceiver uses GFSK modulation technique and its paraments like air data rate, output power and frequency channel can be

configured by the user. It can transmit data at the speed of 2Mbps, 1 Mbps and 250 kbps. The addition of digital filtering internally has enhanced the device to meet the regulatory standards for RF. And lastly, wide power supply range and high-Power Supply Rejection Radio (PSRR) is achieved by the internal voltage regulators [57]. Consideration of all these reasons to enable a reliable communication system between the master and local controller has made an ideal choice to use this sophisticated wireless module.

5.3.3.1 Air data rate

The transmitter uses the modulated signaling rate (air data rate) when either receiving or transmitting data. It can be 2 Mbps, 1 Mbps, or 250 kbps. Probability of on-air collision is reduced and average current consumption is lowered when the transceiver uses high air data rate. And the sensitivity of the receiver is increased when operating at lower air data rate compared to higher air data rate. RF_DR bit in the RF_SETUP sets the air data rate. Both the receiver and transmitter should be configured with same air data rate to communicate with each other.

5.3.3.2 RF Channel Frequency

The center of the channel used by the transceiver is determined by the RF channel frequency. At 2 Mbps, the channel occupies a bandwidth of 2 MHz and at 250 kbps and 1 Mbps a bandwidth of 1 MHz. The programming resolution setting for RF channel frequency is 1 MHz.

At 2 Mbps, the channel spacing should be of 2 MHz or more, to ensure non-overlapping channels. At 250 kbps and 1 Mbps, the channel bandwidth lower than the resolution of the RF frequency or same.

The RF channel frequency is set by the RF_CH register according to the following formula:

$$F0 = 2400 + RF\_CH \ [MHz]$$

5.3.3.3 Enhanced ShockBurst

The transceiver embedded with Enhanced ShockBurst (baseband protocol engine) has made it a unique module for communication. It is a packet-based data link layer, which features automatic acknowledgement and retransmission of packets, automatic packet

assembly and timing. This feature enables the transceiver to enhance its power efficiency for both uni-directional and bi-directional systems, without increasing its complexity and lastly it also enables the implementation of high performance and ultra low power with low cost host microcontrollers.

5.3.3.3.1 Enhanced ShockBurst overview

Enhanced ShockBurst's automatic timing and packet handling is done by ShockBurst and controls all the timing and handling of high-speed bits. When in TX mode, ShockBurst assembles the packet and clocks the bits in the data packet for transmission. And during RX mode, the valid address in the demodulated signal is constantly searched by ShockBurst. When a valid address is found by ShockBurst, the packet is processed and is validated by CRC and if packet is valid, the payload is sent to the RX FIFO's vacant slot.

Enhanced ShockBurst features a reliable bi-directional data link, by automatically handling the packet transaction which is the exchange of packets between two transceivers (Primary Transmitter (PTX) and Primary Receiver (PRX)). PTX always initiates the packet transmission and waits for the acknowledgement packet (ACK packet) from the PRX to complete the packet transaction. The PRX can attach user data to the ACK packet enabling a bi-directional data link.

The NRF24L01 has the capability to form a star network configuration, which can receive data through six different data pipes, Figure 51. Each of the six data pipes will have a unique address but share the same channel frequency. This means that up to six different NRF24L01 configured as PTX can communicate with one NRF24L01 configured as PRX, and configured PRX will be able to distinguish between them. All of the six data pipes can perform full Enhanced ShockBurst functionality.

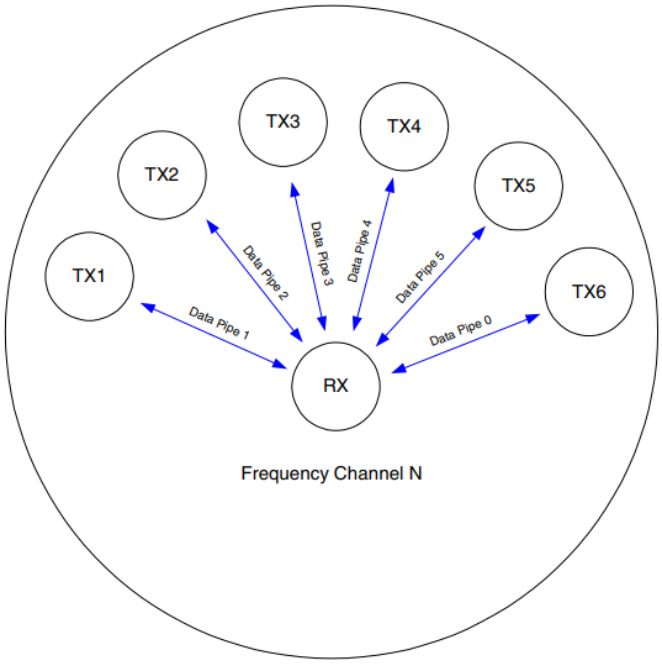

Figure 51: NRF24L01 star network configuration [57]

5.2.4 Interfacing the NRF24L01 through SPI

As shown in Figure 52, the transceiver breakout board has eight pins. Two pins, GND and VCC are for powering the modules. MISO, MOSI, SCK and CSN are used to communicate the NRF24L01 with the microcontroller through the SPI interface. CE is also used for communication with the microcontroller. The IRQ (Interrupt ReQuest pin) is used to signal the microcontroller if a packet is receiver, transmitted correctly or cannot be transmitted correctly.

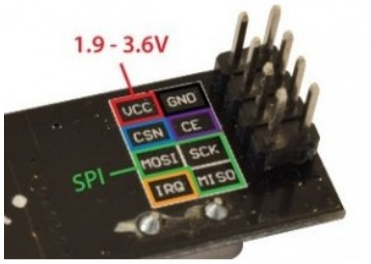

Figure 52: NRF24L01 pin breakout [57]

In Table 14, the transceivers breakout board functions are shown. A brief overview of the pins function during transmission and receiving modes is shown.

Table 14 - NRF24L01 transceiver breakout board

Pin	**Function**	**Function during Tx**	**Function during Rx**
GND	Ground		
VCC	Connect with 3.3 V		
CE	Control data in Tx and Rx mode	High to low transition	CE = 1, High signal
CSn	CSN = 0, it communicates with master and when CSN = 1, it ignores master		
SCK	Generated by master	Transceiver being as slave reads the state of MOSI pin	Arduino being as master reads the state of MISO pin
MOSI	Master Out Slave In	Master transmit, slave receive. In Tx mode, Arduino is master and transceiver is slave. Master sends data bit where slave reads the data. And thus, the transceiver receives commands from Arduino	
MISO	Master in Slave Out		Slave transmit, master receive. In Rx mode, Arduino is master and will only receive from transceiver. The data which will be received by the transceiver will be sent serially trough MISO line and Arduino will read from the same line.

5.2.5 Controlling the NRF24L01 modules with an Arduino

The transmitter requires an SPI interface to read and transmit the data. However, the computer will write the data to a USB port. Therefore, we need to build a bridge between the computer and transmitter that converts the USB output to an SPI output. There are many types of microcontrollers on the market, but a programmable one with a high-level programming language is preferred as it creates the possibility to write simple test programs. Arduino microcontroller is an ideal choice as it could test the NRF24L01 modules and the data coming from the USB.

5.2.5.1 Arduino Mega 2560

Arduino Mega 2560 (Figure 53) is based on ATmega2560, an 8-bit Atmel microcontroller with 256K byte system programmable flash. It has 16 Analog I/O, 54 digital I/O, 4 UARTs, and a reset button.

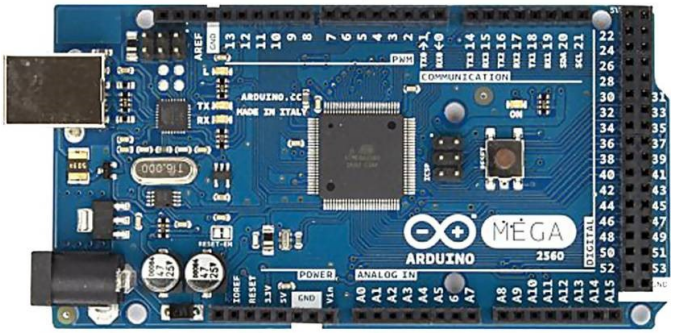

Figure 53: Arduino Mega 2560 board

5.2.5.1.2 Features

- Microcontroller: Atmega 2560
- Input voltage: 7-12 V
- Operating voltage: 5 V
- Analog I/O: 16
- Digital I/O: 54
- PWM pins: 15
- Clock speed: 16 MHz
- EEPROM: 4 KB
- RAM: 8 KB

5.2.6 Encryption

5.2.6.1 Introduction

Cryptography is defined as the science and art of creating undisclosed messages. Encryption is the process where an original message is coded into the cipher text and decryption is the process where the encrypted message is restored back to the original message.

Cryptography has 4 essential objectives and are described as follows [58]:

- Authentication: Process of proving one's identity
- Integrity: Assuring if the received signal has been altered or not from the original message
- Privacy/confidentiality: Ensuring only the intended recipient can read the message
- Non-repudiation: A mechanism to prove that the correct party has send the message

A cryptanalyst should be familiar with different techniques to be used for encryption as his main task is to decipher the received text to recover plaintext. Therefore, it is necessary for a cryptanalyst to be familiar with the encryption technique used, as each algorithm has its own features. The use of Caesar and Vigenere ciphers are implemented in this thesis, making it a 2-level encryption.

5.2.6.1.1 Caesar cipher

Caesar cipher is one of the firstly introduced technique which was originally developed by Julius Ceasar. In this technique the letters of the message are replaced by either a symbol, number or letters. A following example is shown below, where a message is encrypted using Caesar cipher.

Message: Welcome to UOIT

Ciphertext: 7ovmywo 4y 5ys4

A shift of 10 is applied to the message which results in the following Ciphertext shown above. Each letter in the message is replaced. For instance, letter E is represented as letter

O. The following algorithm can be represented as a function of h(x), where x is the message to be encrypted and K is the shift applied to each letter

Encrypted message: $h(x) = (x+k) \bmod 26$ (4.1)

Decrypted message: $h(x) = (x-k) \bmod 26$ (4.2)

5.2.6.1.2 Vigenere Cipher

Vigenere cipher referred as a polyalphabetic substitution was developed by Blaise de Vigenere in the 16th century. In this method, a 26 x 26 matrix table is used to generate an encrypted message [59].

	A	B	C	D	E	F	G	H	I	J	K	L	M	N	O	P	Q	R	S	T	U	V	W	X	Y	Z
A	A	B	C	D	E	F	G	H	I	J	K	L	M	N	O	P	Q	R	S	T	U	V	W	X	Y	Z
B	B	C	D	E	F	G	H	I	J	K	L	M	N	O	P	Q	R	S	T	U	V	W	X	Y	Z	A
C	C	D	E	F	G	H	I	J	K	L	M	N	O	P	Q	R	S	T	U	V	W	X	Y	Z	A	B
D	D	E	F	G	H	I	J	K	L	M	N	O	P	Q	R	S	T	U	V	W	X	Y	Z	A	B	C
E	E	F	G	H	I	J	K	L	M	N	O	P	Q	R	S	T	U	V	W	X	Y	Z	A	B	C	D
F	F	G	H	I	J	K	L	M	N	O	P	Q	R	S	T	U	V	W	X	Y	Z	A	B	C	D	E
G	G	H	I	J	K	L	M	N	O	P	Q	R	S	T	U	V	W	X	Y	Z	A	B	C	D	E	F
H	H	I	J	K	L	M	N	O	P	Q	R	S	T	U	V	W	X	Y	Z	A	B	C	D	E	F	G
I	I	J	K	L	M	N	O	P	Q	R	S	T	U	V	W	X	Y	Z	A	B	C	D	E	F	G	H
J	J	K	L	M	N	O	P	Q	R	S	T	U	V	W	X	Y	Z	A	B	C	D	E	F	G	H	I
K	K	L	M	N	O	P	Q	R	S	T	U	V	W	X	Y	Z	A	B	C	D	E	F	G	H	I	J
L	L	M	N	O	P	Q	R	S	T	U	V	W	X	Y	Z	A	B	C	D	E	F	G	H	I	J	K
M	M	N	O	P	Q	R	S	T	U	V	W	X	Y	Z	A	B	C	D	E	F	G	H	I	J	K	L
N	N	O	P	Q	R	S	T	U	V	W	X	Y	Z	A	B	C	D	E	F	G	H	I	J	K	L	M
O	O	P	Q	R	S	T	U	V	W	X	Y	Z	A	B	C	D	E	F	G	H	I	J	K	L	M	N
P	P	Q	R	S	T	U	V	W	X	Y	Z	A	B	C	D	E	F	G	H	I	J	K	L	M	N	O
Q	Q	R	S	T	U	V	W	X	Y	Z	A	B	C	D	E	F	G	H	I	J	K	L	M	N	O	P
R	R	S	T	U	V	W	X	Y	Z	A	B	C	D	E	F	G	H	I	J	K	L	M	N	O	P	Q
S	S	T	U	V	W	X	Y	Z	A	B	C	D	E	F	G	H	I	J	K	L	M	N	O	P	Q	R
T	T	U	V	W	X	Y	Z	A	B	C	D	E	F	G	H	I	J	K	L	M	N	O	P	Q	R	S
U	U	V	W	X	Y	Z	A	B	C	D	E	F	G	H	I	J	K	L	M	N	O	P	Q	R	S	T
V	V	W	X	Y	Z	A	B	C	D	E	F	G	H	I	J	K	L	M	N	O	P	Q	R	S	T	U
W	W	X	Y	Z	A	B	C	D	E	F	G	H	I	J	K	L	M	N	O	P	Q	R	S	T	U	V
X	X	Y	Z	A	B	C	D	E	F	G	H	I	J	K	L	M	N	O	P	Q	R	S	T	U	V	W
Y	Y	Z	A	B	C	D	E	F	G	H	I	J	K	L	M	N	O	P	Q	R	S	T	U	V	W	X
Z	Z	A	B	C	D	E	F	G	H	I	J	K	L	M	N	O	P	Q	R	S	T	U	V	W	X	Y

Figure 54: Vigenere table [59]

Vigenere table (Figure 54), consist of 26 alphabets written in 26 rows and 26 columns and in each row, one shift is made towards the right in a cyclic manner. The process of encryption is implemented in the following steps:

1. Message to be encrypted: BUY A CAR
2. Any random key generated by the user: HI
3. Repeat the letters of key so that the letters of message are equal, for ex:

MESSAGE: BUY A CAR

KEY: HIH I HIH

4. Now for encryption: take each alphabet of message and key, and find the intersection of row and column in the Vigenere table

ICF I JIY

For decryption of the cipher message, each letter can be traced back to the table to find its key and message as it is the completely opposite of encryption. Based on the Equations (4.3) and (4.4) the encryption and decryption can be written as:

$$C=Ek(Pi) = (Pi+Ki) \bmod 26 \tag{4.3}$$

where,

Pi= p0p1…..pn , C= c0c1…..cn and K = k0….km.

Similarly, decryption is given by:

$$Pi =Dk(Ci)= (Ci-Ki) \bmod 26 \tag{4.4}$$

5.2.7 NRF24L01 Results

5.2.7.1 Introduction

In order to demonstrate the communication needs between the microgrid and Control Centre, a proof-of-concept case study was conducted. In a MG, various measurements from the microgrid sensors (such as voltages, currents, power, frequency and speed of machines) are to be transmitted wirelessly to the Control Centre, where the EMS will check if the measured values are matching to the predicted values. In case of any mismatches, an error signal will be generated and sent back wirelessly to the local controllers at the microgrid

A centralized configuration is implemented, where a two-way communication channel between the local controller and master controller is exchanging information. Furthermore, a star connection topology and a master/slave is established by having two local controllers communicating with a master controller in real-time.

5.2.7.1 Demonstration Setup

Two case studies are conducted, where initially a single point wireless communication channel is tested by sending various signals from the local controllers to a master controller to establish a safe and secure channel. And secondly, a bi-directional wireless communication network is built composed of multiple NRF24L01 transceivers modules. The demonstration setup for both single point communication and network communication are shown below:

As shown in Figure 55, the demonstration used two wireless NRF24L01 transceivers along with two micro-controllers: an Arduino Uno as the Local Controller at the microgrid, and an Arduino MEGA 2560 as the Master Controller at the Control Centre.

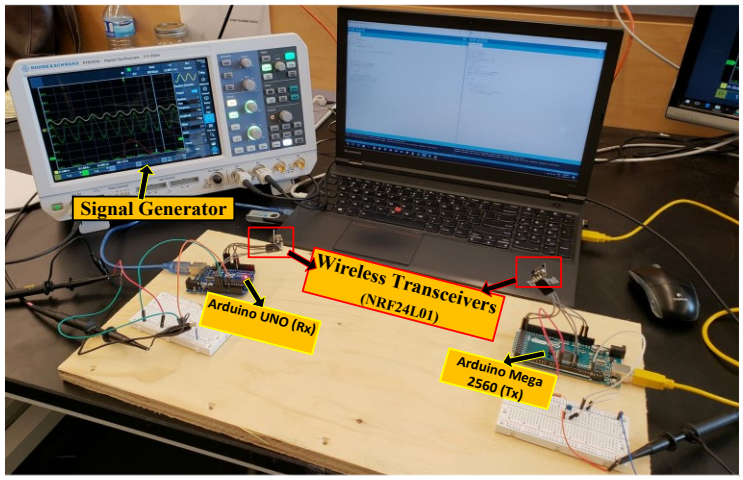

Figure 55: NRF24L01 demonstration setup

For the demonstration setup, showed in Figure 55, two case studies were conducted where digital and analog signals are transmitted wirelessly and the delay between the transmitted and received signal is observed. And a 2-level encryption is added for the save and reliable communication.

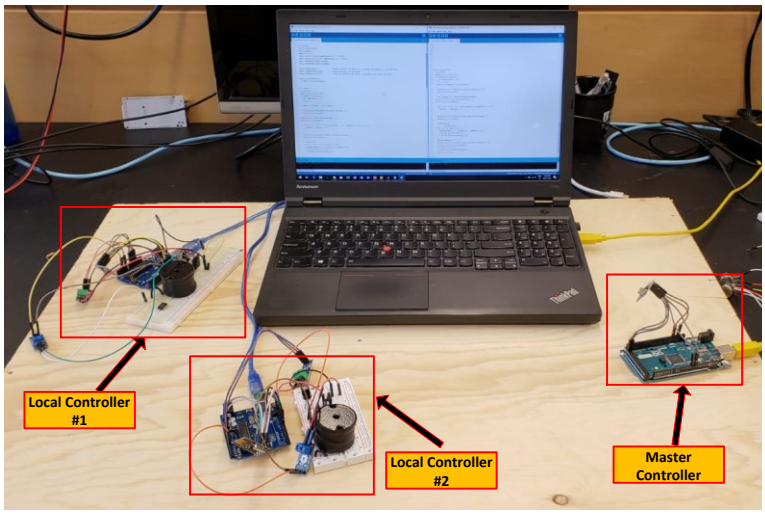

Figure 56: NRF24L01 network demonstration setup

As shown in Figure 56, the demonstration used three wireless NRF24L01 transceivers along with three micro-controllers: two Arduino Uno as the Local Controllers at the microgrid, and one Arduino MEGA 2560 as the Master controller at the Control Centre.

5.2.7.1.1 Case study 1: Digital Signal

In this case study, a 1 Hz pulse signal is transmitted to open/close breakers to shed/connect loads to match generation and load demands

Figure 57 and Figure 58 depicts a 1 Hz pulse signal wirelessly transmitted by using the NRF24L01 from Arduino MEGA 2560 to Arduino UNO. It can be observed that the pulse is transmitted with a delay of 1.6 ms at a sampling rate of 2 Mbps. The sampling can be reduced by increasing the frequency of the transmitted signal.

Figure 57: 1 Hz pulse signal wirelessly transmitted using NRF24L01

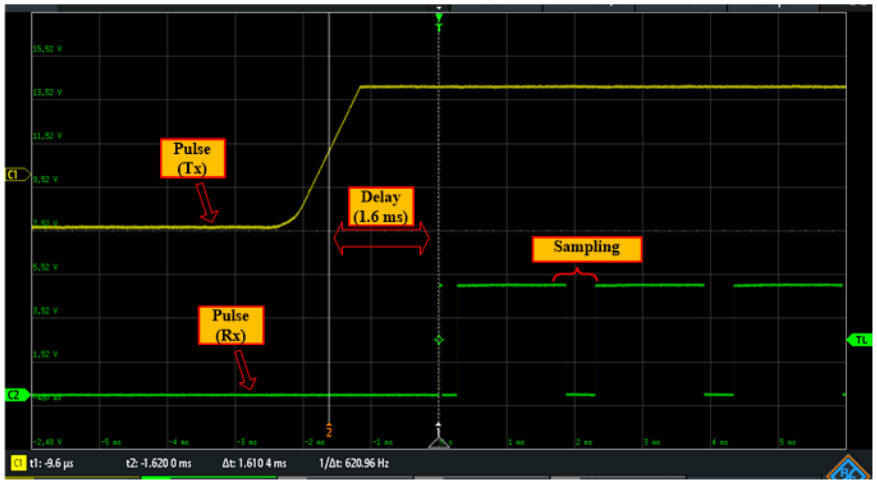

Figure 58: 1 Hz pulse signal wirelessly transmitted using NRF24L01 (zoom view)

5.2.7.1.2 Case study 2: Analog Signal

5.2.7.1.2.1 Sinusoidal Signal Test

In this case study, a 1 Hz sinusoidal signal is transmitted to simulate small signal control signals sent to the local controller at the microgrid level from the master controller at the control center

Figure 59 depicts a 1 Hz sinusoidal signal that is wirelessly transmitted by using the NRF24L01 from Arduino MEGA 2560 to Arduino UNO. It can be observed that the pulse is transmitted with a phase shift of 9.13° (25 ms) at a sampling rate of 2 Mbps. Compared to the previous test, the delay in the sinusoidal signal is higher because the Arduino does not have a Digital-to-Analog Converter (DAC). Therefore, it required an off-line RC low-pass filter acting as a DAC.

Figure 59: 1 Hz sinusoidal signal wirelessly transmitted using NRF24L01

5.2.7.1.2.2 Saw-tooth Signal Test

In this case study, a 1 Hz saw-tooth signal is transmitted to simulate ramp-up or ramp-down power orders to the local controller at the microgrid level from the master controller at the control center

Figure 60 and Figure 61 depict a 1 Hz saw-tooth signal that is wirelessly transmitted by using the NRF24L01 from Arduino MEGA 2560 to Arduino UNO. It can be observed that the pulse is transmitted with a delay of 3.3 ms at a sampling rate of 2 Mbps. The delay time in the saw-tooth signal can be reduced if the Arduino has a built in Digital-to-Analog Converter (DAC). Therefore, due to the lack of DAC in Arduino, an off-line RC low-pass filter is required acting as a DAC.

Figure 60: 1 Hz saw-tooth signal wirelessly transmitted using NRF24L01

Figure 61: 1 Hz saw-tooth signal wirelessly transmitted using NRF24L01 (zoom view)

5.2.7.1.3 Case study 3: Two-level Encryption

In this case study, a two-level encryption is added so that when transmitting any information, it is kept secure from any third party to get access to the desired information. This will enable the user to transmit any vital data or messages to either local controllers or master controller, without having to worry about the information to be leaked by a third-party hacker.

Figure 62 depicts a string of encrypted information from master controller and local controller transmitted wirelessly. It can be observed from COM6 serial monitor (Master controller), that a message (Circuit Breaker #1 ON) is initially being encrypted using the Vignere Cipher and followed by the Ceasar Cipher. The encrypted information after the Ceasar Cipher is being transmitted to COM8 (local controller) and an auto acknowledgement is received back to the COM6 to make sure the information is securely transmitted. It is observed that time from message transmitted and to receive back an acknowledgement takes about roughly 59 ms.

Furthermore, it can also be observed from COM8 serial monitor (Local controller), that a message (Circuit Breaker #5 ON) is also being encrypted using the Vignere Cipher and followed by the Ceasar Cipher. The encrypted information after the Ceasar Cipher is being transmitted to COM6 (master controller) and an auto acknowledgement is received back to the COM8 to make sure the information is securely transmitted. It is observed that the time from message transmitted and to receive back an acknowledgment takes about roughly 63 ms.

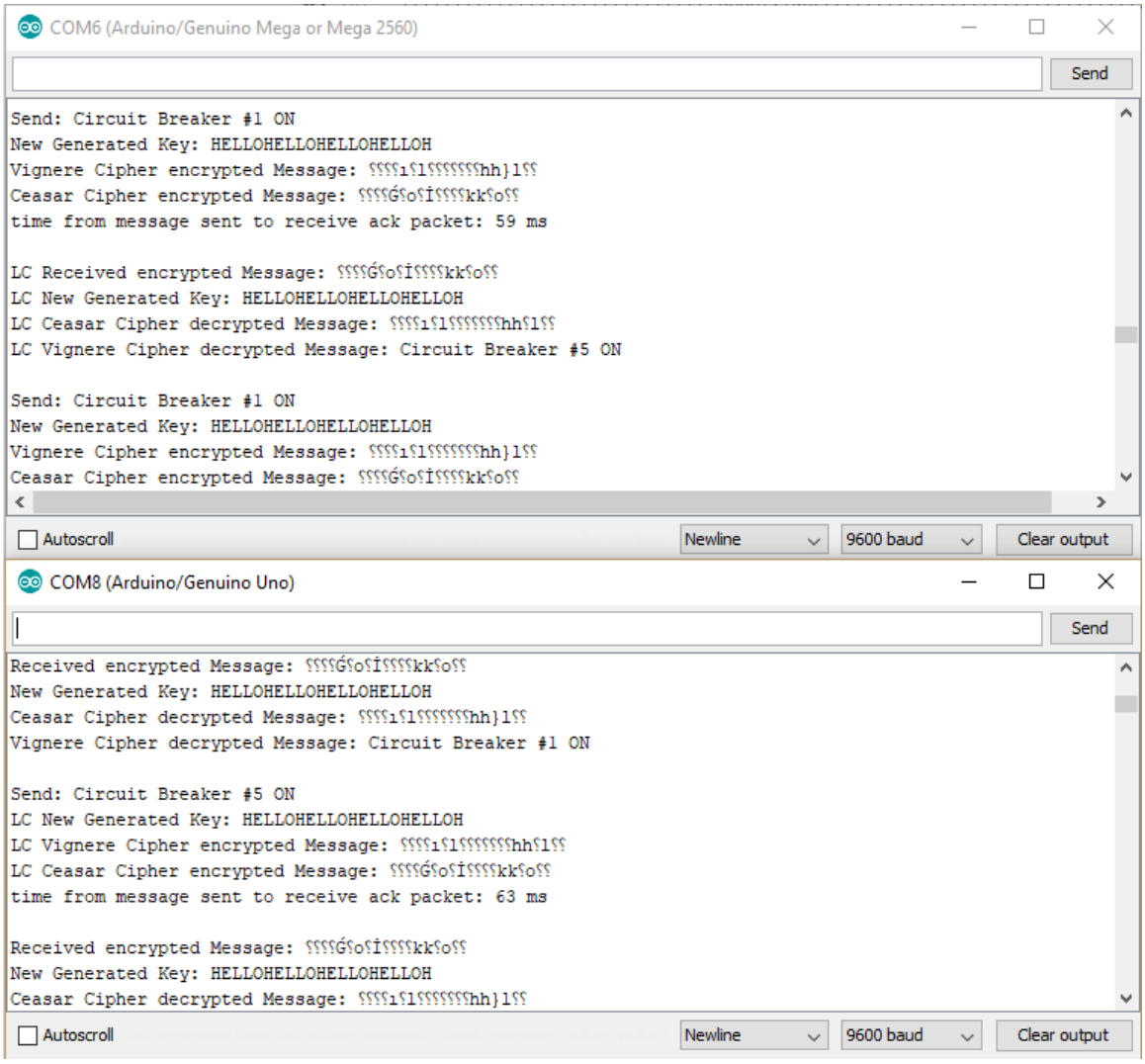

Figure 62: Encrypted information from master controller and local controller transmitted wirelessly

5.2.7.1.4 Case study 4: Range test

A range test was demonstrated in Figure 63 to observe the maximum range of NRF24L01 transceiver. The master controller transceiver is kept stationary at ERC building (2000 Founders Drive) and the local controller transceiver was moved to test the maximum range. It can be observed that a reliable communication link between the local controller and master controller can be up to 300 m range.

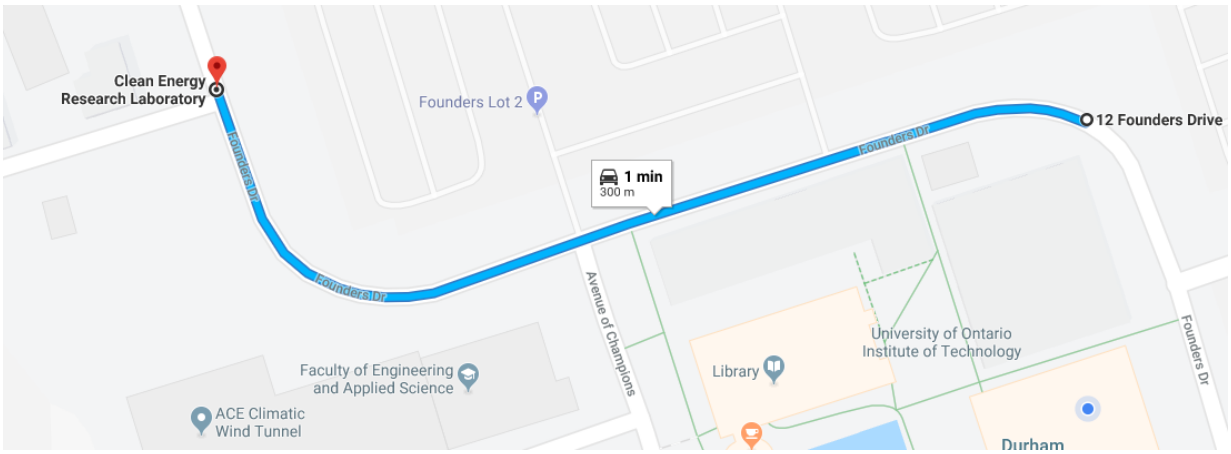

Figure 63: Range test for NRF24L01

5.2.7.1.5 Case study 5: Wireless Network

In this case study, a two-way communication channel between the Master controller and local controller is established and the demonstration setup is shown in Figure 56. As mentioned earlier, this configuration is a star connection topology and used for centralized EMS.

Two boost converters (local controllers #1 and #2) are controlled by a master controller, where a duty cycle is transmitted for the converters to operate. Both voltage and current sensors read the real-time values to frequently observe the controller and transmits the power rating to the master controller to sample the critical generation/demand information from each converter.

In Figure 64, the boost converter (local controller #1) is designed to operate at 0.5 W power. A 5 V input voltage is boosted to 8 V output voltage, when operated at a 50% duty cycle and 31 kHz frequency. The loss of roughly 2 V is due to the noise and the selection of inductor and capacitor components.

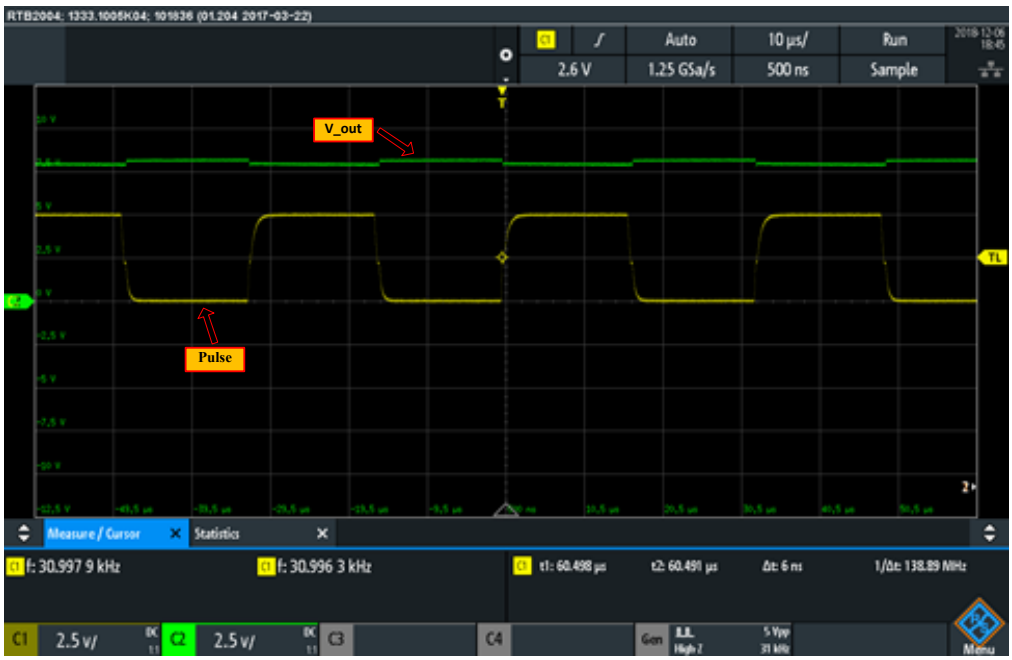

Figure 64: Boost converter (local controller #1)

Figure 65 depicts boost converter (local controller #1) output power transmitted wirelessly from the local controller to master controller. It can be observed from COM8 serial monitor (local controller #1), that voltage and current sensors display the real-time values at output when a duty cycle of 50% is applied. Power (0.5 W) is then calculated and is transmitted to the master controller. It can be observed from COM6 serial monitor (master controller) the information is received without any interruption.

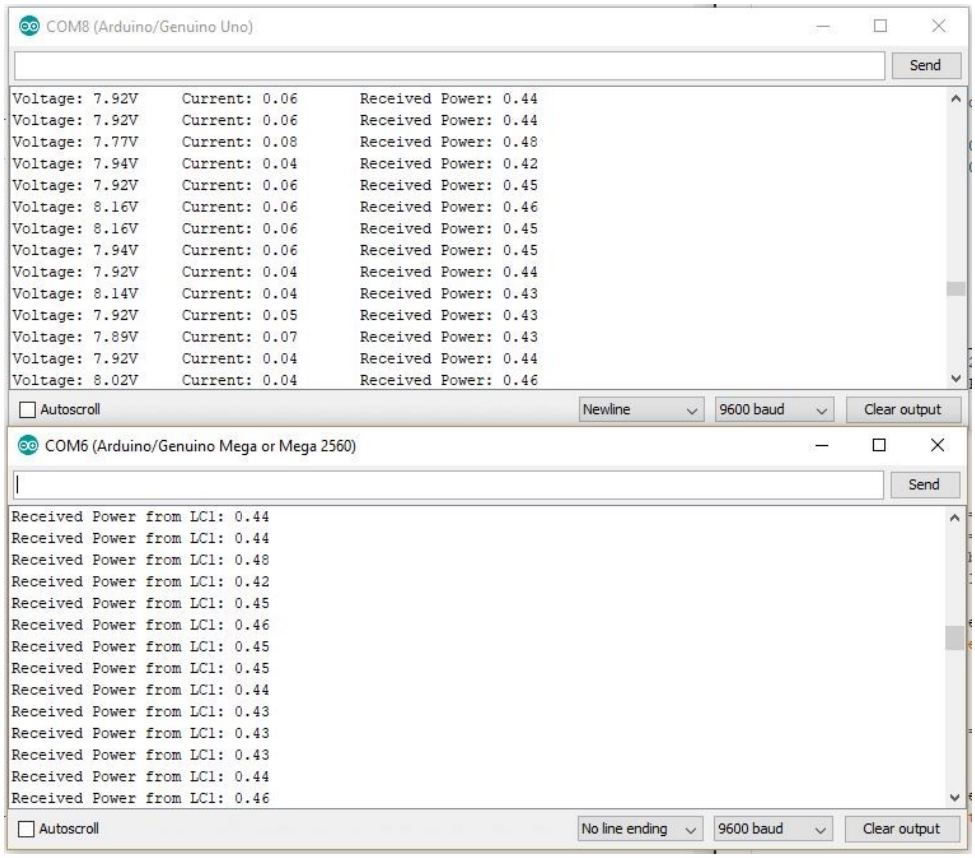

Figure 65: Boost converter (local controller #1) output power transmitted wirelessly to master controller

In Figure 66, the boost converter (local controller #2) is designed to operate at 3 W power. A 10 V input voltage is boosted to 18 V output voltage, when operated at a 50% duty cycle and 31 kHz frequency. The lose of roughly 2 V is due to the noise and the selection of inductor and capacitor components.

Figure 66: Boost controller (local controller #2)

Figure 67 depicts boost converter (Local controller #2) output power transmitted wirelessly to master controller. It can be observed from COM8 serial monitor (local controller #2), that voltage and current sensors display the real-time values at output when a duty cycle of 50% is applied. Power (3 W) is then calculated and is transmitted to the master controller. It can be observed from COM6 serial monitor (master controller) the information is received without any interruption.

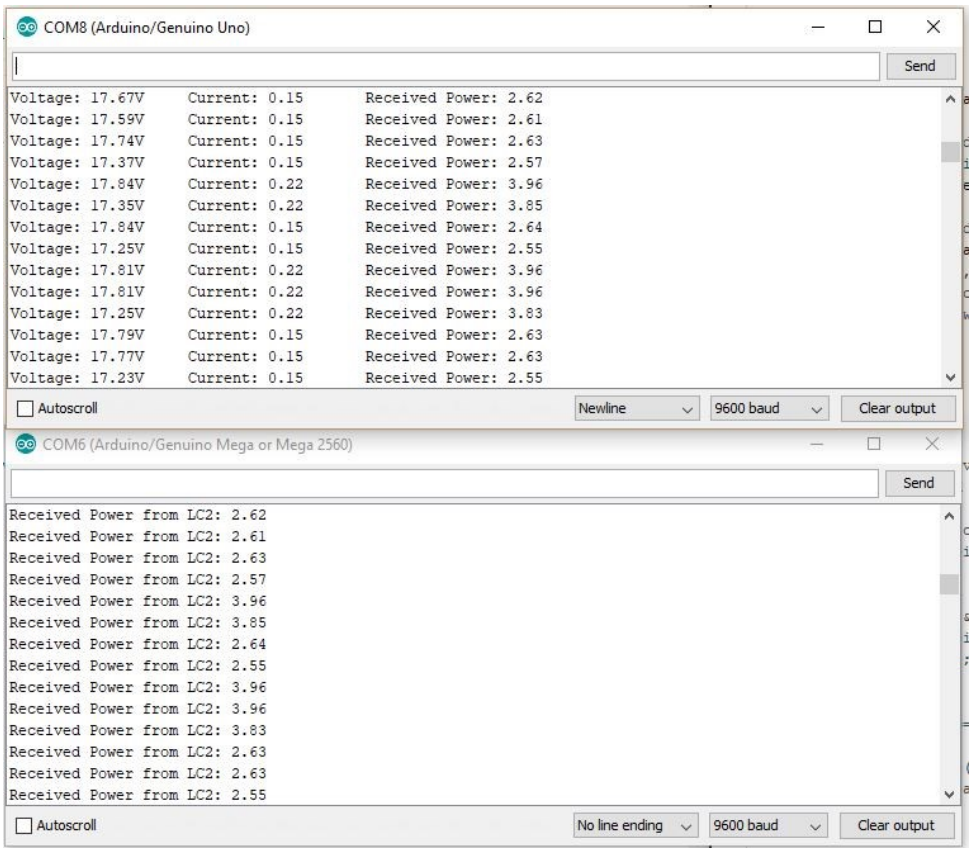

Figure 67: Boost converter (local controller #2) output power transmitted wirelessly to master controller

5.3 LoRa Transceiver

5.3.1 Introduction

The Internet of Things (IoT) is a rapidly growing area of development for the scientific community. It is a concept where all the devices are connected to the internet. In order to support IoT communications, several technologies have been developed such as Wireless Personal Area Network (WPAN), Wireless Local Area Network (WLAN) and Low Power Wide Area Network (LPWAN). LPWAN provide long range communication (several km) and low power consumption. Due to these capabilities, LPWAN technology is investigated.

LoRa is a wireless communication technology developed specifically for long range and low power communication applications. It provides long range capability of up to 5 km range in urban environment and up to 15 km range in suburban. It used spread spectrum technique and chirp modulation to transmit data over a wide range of frequencies from 137 MHz to 1020 MHz therefore, quite a few license-free ISM bands can be used for LoRa communication (169 MHz, 433 MHz, 868 MHz and 915 MHz) [60]. LoRa sacrifices data rate for range hence it is only suitable for applications that need to transmit small amounts of data periodically. This makes LoRa extremely useful for microgrid applications.

5.3.2 LoRa network Architecture

LoRa is promoted as an infrastructure solution for Internet of Things by Samtech and its network architecture is shown in Figure 68. It consists of four components [61]

1. End-device: Collects the data from various sensors and transmits to the gateway
2. Gateway: A gateway acts like a router, which can transmit data from end-device to the cloud and vice versa
3. Network Server: Manages several gateways and assures there is no duplicates send to the server and avoids collisions
4. Application server: Processes and stores the data. It can send data back to the end nodes through the network server and gateway.

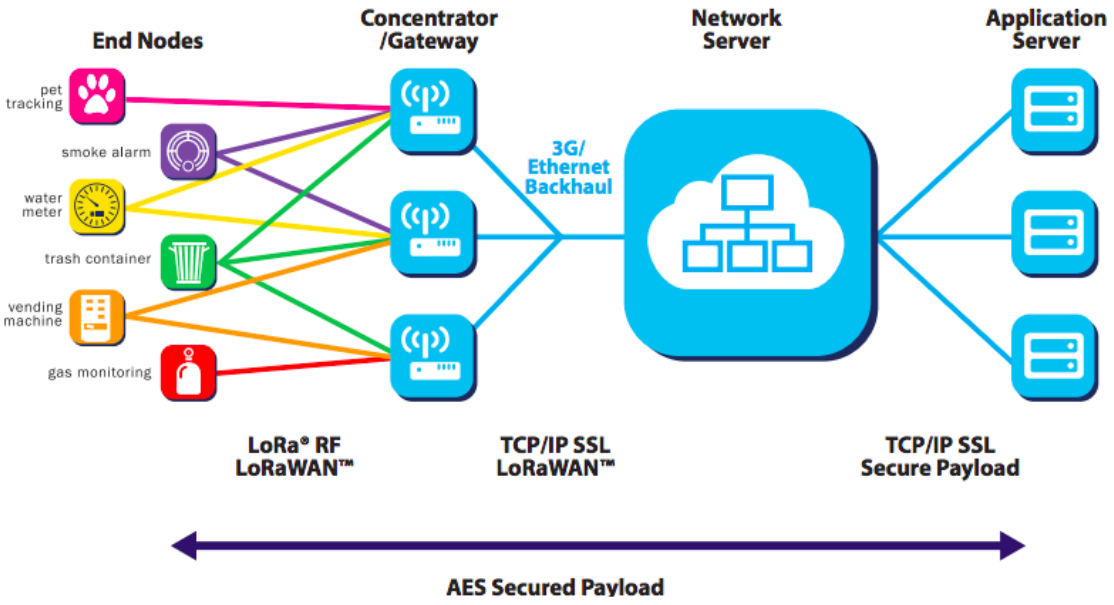

Figure 68: LoRa network architecture [61]

5.3.3 LoRa Modulation Scheme

LoRa utilizes chirp spread-spectrum modulation [62] scheme for achieving long-range with low power. The actual scheme used by Samtech in LoRa PHY is closed source but it is a derivative of chirp spread-spectrum modulation. LoRa uses orthogonal spreading factors to implement a variable data rate for range and power for various application-specific needs. Different combinations of spreading factor, coding rate and bandwidth results in various modes which can be utilized to achieve the required range and data rate.

5.3.3.1 Chirp Spread-Spectrum (CSS)

Chirp Spread-Spectrum is a spread spectrum technique that uses wideband linear frequency modulated chirp pluses to encode information and spread spectrum techniques are methods by which a signal is deliberately spread in the frequency domain [62].

A chirp is a sinusoidal signal of increasing or decreasing frequency. It relies on the linear nature of chirp signals for spreading the bandwidth spectrum of a transmitted signal. A chirp of increasing frequency is called an up-chirp as shown in Figure 69.

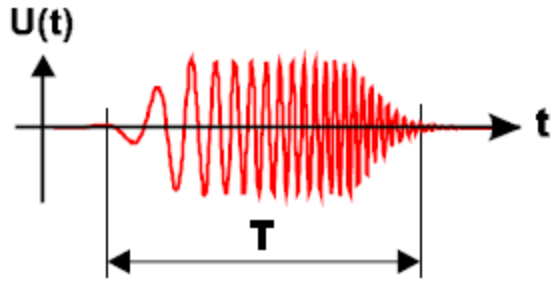

Figure 69: Up-chirp frequency signal [62]

A chirp of decreasing frequency is called down-chirp as shown in Figure 70.

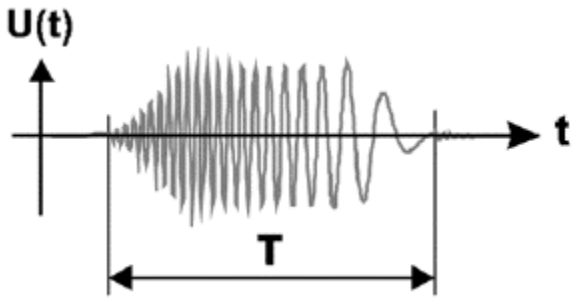

Figure 70: Down-chirp frequency signal [62]

Up-chirp has positive chirp value whereas down-chirp has negative chirp value. The change in frequency can either be linear or exponential.

5.3.4 LoRa Limitations

LoRa is designed specifically for applications that require transmission of small amounts of data periodically using a minimal amount of power. The three key requirements that LoRa tries to address are battery life, simplicity, and range. It is not suitable for applications that require low latency and high data rate.

5.3.5 LoRa Results

In order to demonstrate the communication needs between the microgrid and Control Centre, a proof-of-concept case study was conducted with LoRa transceiver. The test setup is similar to the LoRa network architecture shown in Figure 68, where the information from the end devices is transmitted to application server.

Figure 71 depicts the IoT network server. It can be observed that the status of the LED and the temperature reading sensed by the sensor is transmitted to the loRa IoT network. The status of the LED can represent the status of a breaker, where red represents a CLOSED breaker and green represents an OPEN breaker. The information is transmitted with a delay of 1 s at a sampling rate of 50 kbps and a BW of 125 kHz. This information can later be transmitted to the application server.

downlink | activation | ack | error

counter	port	
11	1	payload: 01 32 35 2E 36 rgbLed: "red" temperature: "25.6"
10	1	payload: 01 32 35 2E 34 rgbLed: "red" temperature: "25.4"
9	1	payload: 01 32 35 2E 37 rgbLed: "red" temperature: "25.7"
8	1	payload: 01 32 35 2E 36 rgbLed: "red" temperature: "25.6"
7	1	payload: 02 32 35 2E 34 rgbLed: "green" temperature: "25.4"
6	1	payload: 02 32 35 2E 35 rgbLed: "green" temperature: "25.5"
5	1	payload: 02 32 35 2E 35 rgbLed: "green" temperature: "25.5"
4	1	payload: 02 32 35 2E 35 rgbLed: "green" temperature: "25.5"

Figure 71: LoRa IoT network server

A range test was demonstrated in Figure 72 to observe the maximum range of LoRa transceiver. The IoT gateway is kept stationary at ERC building (2000 Founders Drive) and the transceiver was moved to test the maximum range. It can be observed that a reliable communication link between the local controller and master controller can be up to 800 m range.

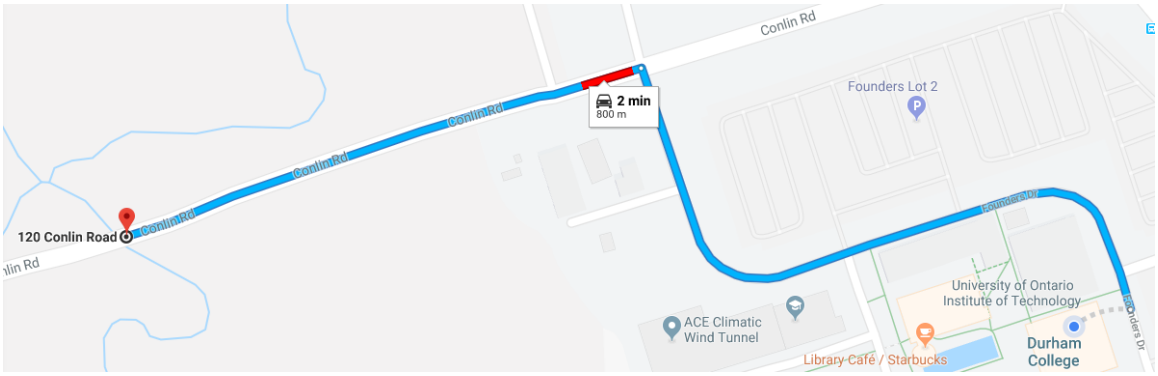

Figure 72: Range test for LoRa

Chapter 6: Conclusion and Future work

6.1 Conclusions

The model of a microgrid system with distributed generation has been developed in MATLAB/SIMULINK. This model contains a photovoltaic distributed generation system with its converter and MPPT algorithm, a battery electric storage system (BESS), a critical load that must be fed at all times and various other non-critical loads.

In order to fully utilize the Battery Energy Storage System (BESS), vector-current control was implemented for the converters to control the active and reactive powers independently for the VSC. The algorithm was investigated and the performance was tested under different operational conditions. Results for this control technique show that the active and reactive power can be controlled precisely.

The transition between grid-connected and islanded modes of operation must be done "seamlessly". A passive detection system, as suggested by IEEE Standard 1547, has been incorporated to detect islanding so that the control mode may be switched seamlessly from P-Q to V/F control mode.

Simulation results for microgrid model show the satisfactory operation during steady-state conditions. The case of a close 3-phase fault has been investigated and verified to result in successful islanding. Various critical load scenarios are observed to investigate the behaviour of voltage and frequency to determine its settling time. However, remote 3-phase faults have been noted not to result in islanding and permitting the system to ride through when a 20% or more base impedance fault is applied.

Harmonics at the 13.8 kV PCC and 600 V PCC have shown satisfactory results as the overall systems THD is less than 1%. As per IEEE Standard 519 limits for harmonic voltage distortion at the point of common coupling (PCC) for 13.8 kV should be less than 5%. Whereas for 600 V PCC, THD should be less than 1.5%.

A bi-directional wireless communication network has been established using a low-cost NRF24L01 transceiver. The network uses a centralized configuration where a two-way communication channel between the local controller and master controller is exchanging

information. Furthermore, a star connection topology and a master/slave is established by having two local controllers communicating with a master controller in real-time.

Two case studies are conducted, where initially a single point wireless communication channel is tested by sending various signals from the local controllers to a master controller to establish a safe and secure channel. And secondly, a bi-directional wireless communication network is built composed of multiple NRF24L01 transceivers modules.

Furthermore, LoRa which is a wireless communication technology developed specifically for long range and low power communication applications is utilized to transmit the the status of the LED and the temperature reading sensed by the sensor is to the loRa IoT network.

6.2 Future Work

The following topics emerging from this thesis are considered for future work:

- Study of microgrid system during unbalanced faults on the 600 V PCC,
- Design of a recloser technique for microgrid resynchronisation to the main grid
- Implement a detailed model of Li-ion Battery storage system,
- Include a CHP model in the microgrid system.
- Utilizing LoRa to establish a wireless communication network for various microgrid application

References

[1] M. H. Ahamed, U. D. S. Dissanayake, H. M. De Silva, H. R. C. G. Pradeep, and N. W. A. Lidula, "Modelling and simulation of a solar PV and battery based DC microgrid system," *2016 Int. Conf. Electr. Electron. Optim. Tech.*, no. 1, pp. 1706–1711, 2016.

[2] T. Thacker, "Phase-locked loops, islanding detection and microgrid operation of single-phase converter systems,", M.A.Sc. thesis, Virginia Polytechnic Institute and State University, 2009.

[3] S. Bush, "*Smart Grid: Communication-Enabled Intelligence for the Electric Power Grid", 1st ed,* John Wiley & Sons, 2013.

[4] F. Khan, M. Y. Ali, V. K. Sood, F. Bhuiyan, P. Insull and F. Ahmad, "Simulation of microgrid system with distributed generation," *2017 IEEE Electrical Power and Energy Conference (EPEC)*, Saskatoon, SK, 2017, pp. 1-6.

[5] Z. Cheng, J. Duan and M. Chow, "To Centralize or to Distribute: That Is the Question: A Comparison of Advanced Microgrid Management Systems," *IEEE Industrial Electronics Magazine*, vol. 12, no. 1, pp. 6-24, March 2018.

[6] A. S. N. Huda and R. Živanović, "Large-scale integration of distributed generation into distribution networks: Study objectives, review of models and computational tools," *Renew. Sustain. Energy Rev.*, vol. 76, no. February, pp. 974–988, 2017.

[7] H. Kanchev, D. Lu, F. Colas, V. Lazarov, and B. Francois, "Energy management and operational planning of a microgrid with a PV based active generator for smart grid applications," *IEEE Trans. Ind. Electron.*, vol. 58, no. 10, pp. 4583–4592, 2011.

[8] T. S. Ustun, C. Ozansoy, and A. Zayegh, "Fault current coefficient and time delay assignment for microgrid protection system with central protection unit," *IEEE Transactions on Power System*, vol. 28, no. 2, pp. 598–606, 2013.

[9] H. Abdi, S. D. Beigvand, and M. La Scala, "A review of optimal power flow studies applied to smart grids and microgrids," *Renew. Sustain. Energy Rev.*, vol. 71, December 2016, pp. 742–766, 2017.

[10] A. K. Basu, S. Chowdhury, and S. P. Chowdhury, "Role of switching devices on microgrid reliability," *Univ. Power Eng. Conf. (UPEC), 2010 45th Int.*, no. 1, pp. 1–6, 2010.

[11] M. Soshinskaya, W. H. J. Crijns-Graus, J. M. Guerrero, and J. C. Vasquez, "Microgrids: Experiences, barriers and success factors," *Renew. Sustain. Energy Rev.*, vol. 40, pp. 659–672, 2014.

[12] A A Salam, A Mohamed, and M. A. Hannan, "Technical Challenges on Microgrids," *Network*, vol. 3, no. 6, pp. 64–69, 2008.

[13] A. F. Sapar, C. K. Gan, A. N. Ramani, and M. Shamshiri, "Modelling and simulation of islanding detection in microgrid," *2014 IEEE Innov. Smart Grid Technol. - Asia, ISGT ASIA 2014*, pp. 641–646, 2014.

[14] M. Z. C. Wanik, A. Bousselham, and A. Elrayyah, "Real-Time simulation modeling for PV-battery based microgrid system," *2016 IEEE Int. Conf. Power Syst. Technol. POWERCON 2016*, 2016.

[15] E. K. B. Indu.V, "A Hybrid Photovoltaic and Battery Energy Storage system with P-Q and V-f control strategies in Microgrid," *2015 IEEE Int. Conf. Power, Instrumentation, Control Comput.*, pp. 4–9, 2015.

[16] W. Yue, C. Zhao, Y. Lu, and G. Li, "A scheme of connecting microgird to AC grid via flexible power electronics interface," *2010 Int. Conf. Power Syst. Technol. Technol. Innov. Mak. Power Grid Smarter, POWERCON2010*, pp. 1–6, 2010.

[17] J. Jo and H. Cha, "Analysis of two charging modes of battery energy storage system for a stand-alone microgrid," *Conf. Proc. - IEEE Appl. Power Electron. Conf. Expo. - APEC*, vol. 2016–May, pp. 1708–1712, 2016.

[18] E. B. Ssekulima and A. Al Hinai, "Coordinated voltage control of solar PV with MPPT and battery storage in grid-connected and microgrid modes," *Proc. 18th Mediterr. Electrotech. Conf. Intell. Effic. Technol. Serv. Citizen, MELECON 2016*, April, pp. 18–20, 2016.

[19] R. G. Wandhare, S. Thale, and V. Agarwal, "Design of a photovoltaic power conditioning system for hierarchical control of a microgrid," *2014 IEEE 40th Photovolt. Spec. Conf. PVSC 2014*, pp. 3144–3149, 2014.

[20] S. Khongkhachat and S. Khomfoi, "Droop control strategy of AC microgrid in islanding mode," *2015 18th Int. Conf. Electr. Mach. Syst. ICEMS 2015*, pp. 2093–2098, 2016.

[21] A. Rahmoun, A. Armstorfer, J. Helguero, H. Biechl, and A. Rosin, "Mathematical modeling and dynamic behavior of a Lithium-Ion battery system for microgrid application," *2016 IEEE Int. Energy Conf.*, pp. 1–6, 2016.

[22] C. Marinescu, L. Barote, and D. Munteanu, "PV-battery system with enhanced control for microgrid integration," *2016 Int. Conf. Appl. Theor. Electr. ICATE 2016 - Proc.*, 2016.

[23] J. He, Y. W. Li, D. Xu, X. Liang, B. Liang and C. Wang, "Deadbeat Weighted Average Current Control with Corrective Feed-Forward Compensation for Microgrid Converters with Nonstandard LCL Filter," *IEEE Transactions on Power Electronics*, vol. 32, no. 4, pp. 2661-2674, April 2017.

[24] D. Pullaguram, S. Mishra, N. Senroy and M. Mukherjee, "Design and Tuning of Robust Fractional Order Controller for Autonomous Microgrid VSC System," *IEEE Transactions on Industry Applications*, vol. 54, no. 1, pp. 91-101, Jan.-Feb. 2018.

[25] Z. Li, Z. Cheng, Y. Xu, Y. Wang, J. Liang and J. Gao, "Hierarchical control of parallel voltage source inverters in AC microgrids," *The Journal of Engineering*, vol. 2019, no. 16, pp. 1149-1152, 3 2019.

[26] H. Bevrani, M. R. Feizi and S. Ataee, "Robust Frequency Control in an Islanded Microgrid: H∞ and μ-synthesis Approaches," *IEEE Transactions on Smart Grid*, vol. 7, no. 2, pp. 706-717, March 2016.

[27] K. S. Rajesh, S. S. Dash, R. Rajagopal, and R. Sridhar, "A review on control of ac microgrid," *Renew. Sustain. Energy Rev.*, vol. 71, January, pp. 814–819, 2017.

[28] A. Mazloomzadeh, M. H. Cintuglu, and O. A. Mohammed, "Islanding detection using synchronized measurement in smart microgrids," *2013 IEEE PES Conf. Innov. Smart Grid Technol. ISGT LA 2013*, 2013.

[29] A. Khamis, H. Shareef, E. Bizkevelci, and T. Khatib, "A review of islanding detection techniques for renewable distributed generation systems," *Renew. Sustain. Energy Rev.*, vol. 28, pp. 483–493, 2013.

[30] C. Li, C. Cao, Y. Cao, Y. Kuang, L. Zeng, and B. Fang, "A review of islanding detection methods for microgrid," *Renew. Sustain. Energy Rev.*, vol. 35, pp. 211–220, 2014.

[31] A. A. Salam, A. Mohamed and M. A. Hannan, "Technical Challenges on Microgrids" *ARPN Journal of Engineering and Applied Sciences*, VOL. 3, NO. 6

[32] G. Antonova, M. Nardi, A. Scott and M. Pesin, "Distributed generation and its impact on power grids and microgrids protection," *2012 65th Annual Conference for Protective Relay Engineers*, College Station, TX, 2012, pp. 152-161.

[33] M. Y. Marwan Haitham Abouzeid, Vijay Sood, "Simulation of intelligent MPPT techniques for a grid integrated PV system using EMTP," University of Ontario Institute of Technology, 2014.

[34] F. F. Rakotomananandro, "Study of Photovoltaic System," Ohio State University, 2011.

[35] N. Langhammer and R. Kays, "Performance Evaluation of Wireless Home Automation Networks in Indoor Scenarios," *IEEE Transactions on Smart Grid*, vol. 3, no. 4, pp. 2252–2261, Dec. 2012.

[36] F. Gómez-cuba, R. Asorey-cacheda, and F. J. González-castaño, "Smart Grid Last-Mile Communications Model and Its Application to the Study of Leased Broadband," *IEEE Transactions on Smart Grid*, vol. 4, no. 1, pp. 5–12, 2013.

[37] Noam, Eli, 2002, "Interconnection Practices," in (eds) Martin Cave, Sumit Majumdar, Ingo Vogelsang, Handbook of Telecommunications Economics, Volume 1, NorthHolland, Amsterdam.

[38] S. Marzal, R. Salas, R. González-Medina, G. Garcerá, and E. Figueres, "Current challenges and future trends in the field of communication architectures for microgrids," *Renew. Sustain. Energy Rev.*, 2017.

[39] Rukun Mao, Huijuan Li, Yan Xu and Husheng Li, "Wireless communication for controlling microgrids: Co-simulation and performance evaluation," *2013 IEEE Power & Energy Society General Meeting*, Vancouver, BC, 2013, pp. 1-5.

[40] V. C. Gungor *et al*., "A Survey on Smart Grid Potential Applications and Communication Requirements," *IEEE Transactions on Industrial Informatics*, vol. 9, no. 1, pp. 28-42, Feb. 2013.

[41] T. Liu, Y. Liu, Y. Mao, Y. Sun, X. Guan, W. Gong, and S. Xiao, "A Dynamic Secret-Based Encryption Scheme for Smart Grid Wireless Communication," *IEEE Transactions on Smart Grid*, vol. 5, no. 3, pp. 1175–1182, May 2014.

[42] A. Usman and S. H. Shami, "Evolution of Communication Technologies for Smart Grid applications," *Renew. Sustain. Energy Rev.*, vol. 19, pp. 191–199, Mar. 2013.

[43] Saha, H., Mandal, S., Mitra, S., Banerjee, S., Saha, U, "Comparative performance analysis between nRF24L01+ and XBEE ZB module based wireless ad-hoc networks," *International Journal of Computer Network and Information Security* 9, 36–44, 2017.

[44] T. Sridhar and J. Anish, "Development of Solar MPPT System Using Boost Converter with Microcontroller," vol. 1, no. 4, pp. 334–340, 2012.

[46] T. Kalitjuka, "Control of Voltage Source Converters for Power System Applications," Norwegian University of Science and Technology, 2011.

[47] J. M. Lee, "Islanding Detection Methods for Microgrids," M.A.Sc. thesis, University of Wisconsin-Madison, 2011.

[48] S. Safdar, B. Hamdaoui, E. Cotilla-Sanchez and M. Guizani, "A survey on communication infrastructure for micro-grids," *2013 9th International Wireless Communications and Mobile Computing Conference (IWCMC)*, Sardinia, 2013, pp. 545-550

[49] X. Fang, S. Misra, G. Xue and D. Yang, "Smart Grid — The New and Improved Power Grid: A Survey," in *IEEE Communications Surveys & Tutorials*, vol. 14, no. 4, pp. 944-980, Fourth Quarter 2012

[50] O. Tremblay and L. A. Dessaint, "Experimental Validation of a Battery Dynamic Model for EV Applications," World Electric Vehicle Journal, vol. 3, 2009.

[51] X. Fang, D. Yang and G. Xue, "Wireless Communications and Networking Technologies for Smart Grid: Paradigms and Challenges," arXiv Prepr. arXiv1112.1158, pp. 1-7, 2011.

[52] V. C. Gungor *et al*., "A Survey on Smart Grid Potential Applications and Communication Requirements," in *IEEE Transactions on Industrial Informatics*, vol. 9, no. 1, pp. 28-42, Feb. 2013.

[53] Nordic, "The Wireless Quarter", Feb. 2007. Available: http://www.nordicsemi.com/eng/nordic/content_download/2135/27213/file/wireless_quarter_q207.pdf

[54] M. Y. Ali, F. Khan and V. K. Sood, "Energy Management System of a Microgrid using Particle Swarm Optimization and Wireless Communication System," *2018 IEEE Electrical Power and Energy Conference (EPEC)*, Toronto, ON, 2018, pp. 1-7.

[55] Sabih H. Gerez, "Implementation of Digital Signal Processing: Some background on GFSK Modulation", March 2016. Available: https://wwwhome.ewi.utwente.nl/~gerezsh/sendfile/sendfile.php/gfsk-intro.pdf?sendfile=gfsk-intro.pdf

[56] Kuo-Jung Sun, Zuo-Min Tsai, K. -. Lin and Huei Wang, "A noise optimization formulation for CMOS low-noise amplifiers with on-chip low-Q inductors," in *IEEE Transactions on Microwave Theory and Techniques*, vol. 54, no. 4, pp. 1554-1560, June 2006.

[57] D. Kalinksy & R. Kalinsky, "Introduction to Serial Peripheral Interface." Embedded system design. Available: http://embedded.com/columns/beginerscorner/9900483?_requestid=245610

[58] NRF24L01+ Single Chip 2.4G Hz Transceiver Product Specification v1.0 (September 2008). Available: http://www.nordicsemi.com/files/Product/data_sheet/nRF24L01P_Product_Specification10.pdf

[59] A. Iqbal and T. Iqbal, "Low-cost and Secure Communication System for Remote Micro-grids using AES Cryptography on ESP32 with LoRa Module," *2018 IEEE Electrical Power and Energy Conference (EPEC)*, Toronto, ON, 2018, pp. 1-5.

[60] The Vigenere Ciphere Encryption and Decryption, Available: https://pages.mtu.edu/~shene/NSF-4/Tutorial/VIG/Vig-Base.html

[61] F. A. Aoudia, M. Gautier, M. Magno, M. Le Gentil, O. Berder, and L. Benini, "Long-short range communication network leveraging LoRa and wake-up receiver," Microprocessors Microsyst., vol. 56, pp. 184–192, Feb. 2018.

[62] LoRa Alliance. (2015). A technical overview of LoRa and LoRaWAN. (November), 1-20. Available: https://www.lora-alliance.org/portals/0/documents/whitepapers/LoRaWAN101.pdf

[63] Semtech Corporation, "LoRa Modulation Basics," no. May, pp. 1–26, 2015.

APPENDIX

Publications

1. M. Y. Ali, F. Khan and V. K. Sood, "Energy Management System of a Microgrid using Particle Swarm Optimization and Wireless Communication System," *2018 IEEE Electrical Power and Energy Conference (EPEC)*, Toronto, ON, 2018, pp. 1-7.
2. F. Khan, A. Sunbul, M. Y. Ali, H. Abdel-Gawad, S. Rahnamayan and V. K. Sood, "Maximum Power Point Tracking in Photovoltaic Farms Using DE and PSO Algorithms: A Comparative Study," *2018 IEEE Congress on Evolutionary Computation (CEC)*, Rio de Janeiro, 2018, pp. 1-9.
3. F. Khan, M. Y. Ali, V. K. Sood, F. Bhuiyan, P. Insull and F. Ahmad, "Simulation of microgrid system with distributed generation," *2017 IEEE Electrical Power and Energy Conference (EPEC)*, Saskatoon, SK, 2017, pp. 1-6.

Book Chapter

1. Vijay K. Sood, Mohammad Y. Ali and Faizan Khan, "Energy Management System of a Microgrid using Particle Swarm Optimization (PSO) and communication system", Springer Books, 29 pages.